



저작자표시-비영리-변경금지 2.0 대한민국

이용자는 아래의 조건을 따르는 경우에 한하여 자유롭게

- 이 저작물을 복제, 배포, 전송, 전시, 공연 및 방송할 수 있습니다.

다음과 같은 조건을 따라야 합니다:



저작자표시. 귀하는 원저작자를 표시하여야 합니다.



비영리. 귀하는 이 저작물을 영리 목적으로 이용할 수 없습니다.



변경금지. 귀하는 이 저작물을 개작, 변형 또는 가공할 수 없습니다.

- 귀하는, 이 저작물의 재이용이나 배포의 경우, 이 저작물에 적용된 이용허락조건을 명확하게 나타내어야 합니다.
- 저작권자로부터 별도의 허가를 받으면 이러한 조건들은 적용되지 않습니다.

저작권법에 따른 이용자의 권리는 위의 내용에 의하여 영향을 받지 않습니다.

이것은 [이용허락규약\(Legal Code\)](#)을 이해하기 쉽게 요약한 것입니다.

[Disclaimer](#)

Ph.D. DISSERTATION

DESIGN OF MULTISTACKED
TRUE-TIME DELAY LINE AND
PHASE TUNABLE REFLECTOR FOR
LOW-PROFILE WIDEBAND CP ARRAY
ANTENNA SYSTEM

낮은 높이의 광대역 원형 편파 배열 안테나
시스템을 위한 다층 적재된 실시간 지연 회로와
위상 조절 반사판 설계

February 2020

GRADUATE SCHOOL OF ELECTRICAL
ENGINEERING AND COMPUTER SCIENCE
SEOUL NATIONAL UNIVERSITY

MINYOUNG YOON

공학박사 학위논문

DESIGN OF MULTISTACKED
TRUE-TIME DELAY LINE AND
PHASE TUNABLE REFLECTOR FOR
LOW-PROFILE WIDEBAND CP ARRAY
ANTENNA SYSTEM

낮은 높이의 광대역 원형 편파 배열 안테나
시스템을 위한 다층 적재된 실시간 지연 회로와
위상 조절 반사판 설계

2020 년 2 월

서울대학교 대학원
전기 · 컴퓨터공학부

윤 민 영

DESIGN OF MULTISTACKED
TRUE-TIME DELAY LINE AND
PHASE TUNABLE REFLECTOR FOR
LOW-PROFILE WIDEBAND CP ARRAY
ANTENNA SYSTEM

지도 교수 남 상 욱

이 논문을 공학박사 학위논문으로 제출함

2020 년 2 월

서울대학교 대학원

전기 · 컴퓨터공학부

윤 민 영

윤민영의 공학박사 학위논문을 인준함

2020 년 2 월

위 원 장 _____ 서 광 석 _____ (인)

부위원장 _____ 남 상 욱 _____ (인)

위 원 _____ 박 남 규 _____ (인)

위 원 _____ 오 정 석 _____ (인)

위 원 _____ 박 익 모 _____ (인)

Abstract

In this thesis, two essential technologies to realize a low profile wideband phased array antenna system are described. Phased array antennas, which have been actively used in military and civil applications such as radar, electronic warfare (EW), and wireless communications, are becoming more advanced as the system specification demanded by the industry. Especially, low-profile wideband phased array antennas are actively studied. It has been a challenge to design wideband and low-profile antennas, which can be surface-mounted on airborne applications such as missile, aircraft, and unmanned aerial vehicle (UAV) to reduce air resistance. Target application in this thesis is jammer in electronic warfare which is to search the enemy's position and shoot a signal of a large power of a certain frequency to the position by beamforming, so it is designed to selectively choose a frequency in a wide band. The low-profile wideband array antenna system for the application consists of a wideband beamforming network and a low-profile wideband array antenna. In this thesis, we analyzed the issues and problems in each part and overcame them to design and implement the low-profile wideband antenna system. The contents of the study carried out are as follows.

At first, design considerations and procedure of wideband beamforming network is presented. Three factors that can affect group delay variation are analyzed, which is the most important

performance indicator of the true-time delay line (TTD). First factor that affects group delay characteristic is off-state capacitor resonance. To minimize degradation of TTD performance due to the resonances, switches with an off-state isolation of more than 30 dB are required. Second factor is reflected wave due to discontinuity, so that matching must be accomplished in design of TTDs and all system. The last factor is the phase error caused by the reflection coefficient due to the antenna impedance. Monte Carlo simulations were performed to investigate the effect of phase delay error on the beam steering angle and side lobe level due to antenna impedance. And the actual antenna is designed to verify the effect of the phase delay error on the antenna impedance. Considering these factors 7-bit multistacked TTD was designed and fabricated for miniaturization which is an additional issue when designing a TTD. Fabrication and measurement were performed and our approach shows an improved performance regarding a figure of merit defined as the relative delay divided by the insertion loss at the longest delay state, a large number of bits of resolution, and low power consumption. Finally, a wideband antenna system was constructed to verify the fabricated TTD. Beam steering is performed without beam squint within the 3 : 1 bandwidth, which verify that the miniaturized TTD is capable of wideband beam steering.

Second, to solve performance degradation problems when forming a unidirectional beam by attaching a perfect electric conductor (PEC) reflector close to the wideband antenna is described for low-profile

wideband phased array antenna systems. . The most applicable type of antennas for low profile wideband antenna array is spiral antenna which has advantages of simple manufacture process and miniaturization for array. Spiral antenna has the disadvantage of requiring a reflector for unidirectional patterns due to its bi-directional circular polarized pattern. We analyzed the reason why the axial ratio (AR) could be deteriorated by the reflector first. Based on analysis, a polarization-dependent phase tunable reflector is proposed to implement the required $\angle\Gamma_{xx}^R$ and $\angle\Gamma_{yy}^R$ using varactors for improvement of AR. To verify that AR is effectively improved by the polarization-dependent phase tunable reflector, spiral array antenna backed by the polarization-dependent phase tunable reflector was designed and fabricated. Periodic boundary simulation for infinite array and simulation of 4×4 array with dummy were performed. A 4×4 array with dummy of the fabricated array with polarization-dependent phase tunable reflector for measurement. Fabricated array antenna has a reflection coefficient of less than -10 dB in the entire target band. All measurement results and simulation results have high consistent. AR improvement was achieved through the measurement results by changing bias voltage applied to varactors on polarization-dependent phase tunable reflector. According to this measurement process and results we implemented a spiral array antenna capable of beam steering from -30° to 30° with excellent circular polarization (CP) characteristics with an AR value of less than 1.5 dB within the 3 dB beamwidth without loss by

applying polarization–dependent phase tunable reflector.

In conclusion, we investigated and analyzed two issues to overcome for implementation of a low–profile wideband antenna system. Through accurate analysis, appropriate solution could be found and applied to design of wideband beamforming network and low–profile wideband array antenna. Fabrications and measurements were conducted to prove the validity of the entire process.

Keywords: Wideband beamforming network, multistacked true–time delay, low–profile wideband antenna, spiral array, phase tunable reflector, axial ratio improvement

Student Number: 2013–20833

Table of Contents

Abstract.....	i
Table of Contents.....	v
List of Figures	viii
List of Table	xvi
Chapter 1. Introduction.....	1
1.1. Motivation	1
1.2. Organization of the Dissertation	4
Chapter 2. Wideband Beamforming Network.....	5
2.1. Analysis of factors that affects group delay variation in TTD	6
2.1.1. Accurate group delay measurement technique in vector network analyzer.....	6
2.1.2. Off-switch capacitor resonance	10
2.1.3. Reflected wave due to discontinuity.....	13
2.1.4. Antenna impedance variation over frequency	16
2.2. Design of 7-bit multistacked true-time delay for	

miniaturization.....	26
2.2.1. Design considerations	27
2.2.2. TTD resolution and number of bits	30
2.2.3. Optimal design of signal vias.....	32
2.2.4. Fabrication and measurement results.....	36
2.2.5. Verification of TTD.....	40
2.3. Conclusion.....	53
Chapter 3. Low–profile Wideband Antenna.....	55
3.1. Analysis of AR deterioration backed by reflector ...	57
3.2. Improvement of AR with polarization–dependent phase tunable reflector	63
3.2.1. AR improvement through reflector with ideal reflection phase.....	63
3.2.2. Practical design issues of reflector with varactors	68
3.2.3. AR improvement through 1D phase tunable reflector	76
3.2.4. AR improvement through 2D phase tunable reflector	79

3.3. Design of spiral antenna array backed by polarization– dependent 1D phase tunable reflector	83
3.3.1. Periodic boundary simulation for infinite array	84
3.3.2. 4 × 4 array simulation with dummy	87
3.4. Fabrication and measurement results	90
3.5. Conclusion.....	107
 Bibliography	 110
Abstract in Korean	115

List of Figures

Fig. 2.1 Block diagram of wideband beamforming network.....	5
Fig. 2.2 Group delay measurement result (a) aperture : 4 MHz (b) aperture : 100 MHz.....	8
Fig. 2.3 (a) Conventional switched line (b) switched line using cascaded switches.....	11
Fig. 2.4 Group delay result of CST simulation and measurement with conventional switched line TTD (delay difference : 15 ps)..	12
Fig. 2.5 Group delay result of CST simulation and measurement with conventional switched line TTD (delay difference : 270 ps)	12
Fig. 2.6 Group delay result of CST simulation and measurement with TTD using cascaded switches (delay difference : 270 ps) .	12
Fig. 2.7 Transmission line model with discontinuity	14
Fig. 2.8 Transmission line model with delay time of T_0 for antenna load of Z_A	16
Fig. 2.9 First term and second term of equation (2.11)	17
Fig. 2.10 1D linear phased array antenna system	18
Fig. 2.11 Monte Carlo simulation 100 sampling result with beam steering angle of 30° at $RL_{\min} = 7$ dB, $\epsilon_{\max} = 26.5^\circ$ of 8 elements uniform array.....	19
Fig. 2.12 Linear array model with spiral antenna of 8 elements ..	22
Fig. 2.13 Linear array with N elements.....	27
Fig. 2.14 Block diagram of TTD line	28

Fig. 2.15 Cross-sectional view of multistacked PCB and layer characteristics	31
Fig. 2.16 Side-view of vias: (a) ViaA, (b) ViaB, and (c) ViaC	32
Fig. 2.17 Equivalent circuit of a via	33
Fig. 2.18 Capacitance of each via.....	33
Fig. 2.19 Measurements of signal vias according to radius of anti-pad: (a) ViaA, (b) ViaB, and (c) ViaC	35
Fig. 2.20 Fabricated TTD in PCB process	36
Fig. 2.21 Measured (a) input/output reflection coefficients and (b) insertion loss of the TTD for the main bits	37
Fig. 2.22 Measured phase delay with respect to the shortest delay state of the TTD	38
Fig. 2.23 Measured group delay of the TTD.....	38
Fig. 2.24 24-way wideband power divider (a) CST simulation model and (b) fabricated model (393 x 318 mm ²)	40
Fig. 2.25 Simulation and measurement results of input reflection coefficient of 24-way wideband power divider	41
Fig. 2.26 Simulation and measurement results of output reflection coefficient of 24-way wideband power divider	41
Fig. 2.27 Simulation and measurement results of isolation between adjacent output ports of 24-way wideband power divider	42
Fig. 2.28 Wideband beamforming network (a) CST simulation model and (b) fabricated model (425 x 359 x 110 mm ³).....	43
Fig. 2.29 Block diagram of digital circuit with flip-flop and information of 30 pins	44

Fig. 2.30 RF shielding case (a) 2D model and (b) fabricated model	45
Fig. 2.31 Radiation pattern measurement results without RF shielding case when terminated at 50 Ohm with 24-way power divider and 24 TTDs without antenna.....	46
Fig. 2.32 Radiation pattern measurement results with RF shielding case when terminated at 50 Ohm with 24-way power divider and 24 TTDs without antenna.....	46
Fig. 2.33 Radiation pattern measurement results without RF shielding case when total beamforming network is connected with antennas	47
Fig. 2.34 Radiation pattern measurement results with RF shielding case when total beamforming network is connected with antennas	48
Fig. 2.35 Wideband conformal phased array antenna system with wideband beamforming network.....	48
Fig. 2.36 $\phi = 0^\circ$ cut normalized results of beam steering from -30° to 40° in azimuth angle at 6 GHz	49
Fig. 2.37 $\phi = 90^\circ$ cut normalized results of beam steering from 10° to 30° in elevation angle at 6 GHz	50
Fig. 2.38 $\phi = 0^\circ$ cut normalized results of 0° beam steering in azimuth angle at 2, 3, 4, 5, 6 GHz	51
Fig. 2.39 $\phi = 0^\circ$ cut normalized results of 10° beam steering in azimuth angle at 2, 3, 4, 5, 6 GHz.	51

Fig. 2.40 $\phi=0^\circ$ cut normalized results of 20° beam steering in azimuth angle at 2, 3, 4, 5, 6 GHz	52
Fig. 2.41 $\phi=0^\circ$ cut normalized results of 30° beam steering in azimuth angle at 2, 3, 4, 5, 6 GHz	52
Fig. 3.1 Multiple reflection between antenna and reflector.....	57
Fig. 3.2 Designed 2–arm spiral antenna (a) top view, (b) side cut view.....	60
Fig. 3.3 Conductor pattern of 2–arm spiral antenna	60
Fig. 3.4 Comparison of the AR of designed spiral antenna backed by PEC plane at broadside	62
Fig. 3.5 Optimum AR results at broadside obtained by changing $\angle\Gamma_{xx}^R$ and $\angle\Gamma_{yy}^R$ individually (2D) compared to AR with PEC reflector	65
Fig. 3.6 Required $\angle\Gamma_{xx}^R$ and $\angle\Gamma_{yy}^R$ for optimum AR in Fig. 3.5 (2D).	65
Fig. 3.7 Optimum AR results at broadside obtained by changing $\angle\Gamma_{xx}^R$ of (1D) with $\angle\Gamma_{yy}^R$ fixed at -180° compared to AR with PEC reflector.....	66
Fig. 3.8 Required $\angle\Gamma_{xx}^R$ and $\angle\Gamma_{yy}^R$ for optimum AR in Fig. 3.7 (1D).	66

Fig. 3.9 Optimum AR results at broadside obtained by changing $\angle\Gamma_{yy}^R$ of (1D) with $\angle\Gamma_{xx}^R$ fixed at -180° compared to AR with PEC reflector.....	67
Fig. 3.10 Required $\angle\Gamma_{xx}^R$ and $\angle\Gamma_{yy}^R$ for optimum AR in Fig. 3.9 (1D).	67
Fig. 3.11 Equivalent circuit of varactor.	68
Fig. 3.12 Proposed design model of polarization–dependent 1D phase tunable reflector with varactors (a) top view, (b) side cut view.	69
Fig. 3.13 Reflection phase of Γ_{xx}^R and Γ_{yy}^R for an incident plane wave depending on the capacitance change of the varactors when R_S is 0 ohm	71
Fig. 3.14 Reflection phase of Γ_{xx}^R for an incident plane wave depending on the capacitance change of the varactors when R_S is 0.8 ohm	72
Fig. 3.15 Reflection phase of Γ_{xx}^R for an incident plane wave depending on the capacitance change of the varactors when R_S is 5 ohm.	72
Fig. 3.16 Real part of Z_S for an incident plane wave depending on the capacitance and R_S change of the varactors	74

Fig. 3.17 Imaginary part of Z_S for an incident plane wave depending on the capacitance and R_S change of the varactors75

Fig. 3.18 Optimum AR result calculated in Fig. 3.7 and AR results of spiral antenna array with 1D reflector at broadside depending on capacitance of ideal varactor by changing $\angle\Gamma_{xx}^R$ of (1D) with $\angle\Gamma_{yy}^R$ fixed at -180° 77

Fig. 3.19 Optimum AR result calculated in Fig. 3.7 and AR results of spiral antenna array with 1D reflector at broadside depending on capacitance of practical varactor by changing $\angle\Gamma_{xx}^R$ of (1D) with $\angle\Gamma_{yy}^R$ fixed at -180° 77

Fig. 3.20 Optimum AR result calculated in Fig. 3.7 and AR results of spiral antenna array with 1D reflector at broadside depending on capacitance of ideal varactor by changing $\angle\Gamma_{yy}^R$ of (1D) with $\angle\Gamma_{xx}^R$ fixed at -180° 78

Fig. 3.21 Optimum AR result calculated in Fig. 3.7 and AR results of spiral antenna array with 1D reflector at broadside depending on capacitance of practical varactor by changing $\angle\Gamma_{yy}^R$ of (1D) with $\angle\Gamma_{xx}^R$ fixed at -180° 78

Fig. 3.22 Proposed design model of polarization-dependent 2D phase tunable reflector with varactors79

Fig. 3.23 Optimum AR result calculated in Fig. 3.5 and AR results of spiral antenna array with 2D reflector at broadside depending on capacitance of ideal varactor	81
Fig. 3.24 Optimum AR result calculated in Fig. 3.5 and AR results of spiral antenna array with 2D reflector at broadside depending on capacitance of practical varactor.....	82
Fig. 3.25 Periodic boundary model of spiral antenna backed by polarization-dependent phase tunable reflector with varactors	84
Fig. 3.26 AR results and the radiation efficiency results of spiral antenna array of periodic structure at broadside depending on capacitance of varactor	85
Fig. 3.27 Input reflection coefficient of spiral antenna array of periodic structure depending on capacitance of varactor	86
Fig. 3.28 4×4 array with dummy simulation model backed polarization-dependent phase tunable reflector (a) top view (b) side view	88
Fig. 3.29 AR results and the radiation efficiency results of 4×4 array with dummy at broadside depending on capacitance of varactor.....	89
Fig. 3.30 The fabrication model of polarization-dependent phase tunable reflector	90
Fig. 3.31 4×4 array with dummy fabrication model backed polarization-dependent phase tunable reflector (a) top view (b) perspective view (c) back view	91

Fig. 3.32 Reflection coefficient simulation results of 4×4 array with dummy for all 16 ports at 1 GHz to 7 GHz	93
Fig. 3.33 Reflection coefficient measurement results of 4×4 array with dummy for all 16 ports at 1 GHz to 7 GHz	93
Fig. 3.34 Reflection coefficient simulation results of 4×4 array with dummy for all 16 ports at 2.4 GHz to 3.2 GHz	94
Fig. 3.35 Reflection coefficient measurement results of 4×4 array with dummy for all 16 ports at 2.4 GHz to 3.2 GHz	94
Fig. 3.36 The mounted model in chamber for the measurement ..	95
Fig. 3.37 4×4 array with dummy fabrication model with a circuit implemented using series batteries to adjust the voltage applied to the varactors of reflector	95
Fig. 3.38 AR simulation results of 4×4 array with dummy depending on bias voltage applied to varactors on reflector ..	96
Fig. 3.39 AR measurement results of 4×4 array with dummy depending on bias voltage applied to varactors on reflector ..	96
Fig. 3.40 Simulation and measurement results of RHCP gain at broadside in 2.4–3.2 GHz when bias voltage of 2.1 V is applied to varactors on reflector	99
Fig. 3.41 Simulation and measurement results of LHCP gain at broadside in 2.4–3.2 GHz when bias voltage of 2.1 V is applied to varactors on reflector	100
Fig. 3.42 Simulation and measurement results of RHCP gain pattern in $\phi = 0^\circ$ cut when bias voltage of 2.1 V is applied to varactors on reflector	100

Fig. 3.43 Simulation and measurement results of LHCP gain pattern in $\phi=0^\circ$ cut when bias voltage of 2.1 V is applied to varactors on reflector	101
Fig. 3.44 Simulation and measurement results of RHCP gain pattern in $\phi=90^\circ$ cut when bias voltage of 2.1 V is applied to varactors on reflector	101
Fig. 3.45 Simulation and measurement results of LHCP gain pattern in $\phi=90^\circ$ cut when bias voltage of 2.1 V is applied to varactors on reflector	102
Fig. 3.46 AR measurement results in $\phi=0^\circ$ cut and $\phi=90^\circ$ cut when bias voltage of 2.1 V is applied to varactors on reflector	102
Fig. 3.47 Simulation results of the RHCP pattern depending on beam steering angle from -30° to 30° in the $\phi=0^\circ$ cut when bias voltage of 2.1 V is applied to varactors on reflector	103
Fig. 3.48 Measurement results of the RHCP pattern depending on beam steering angle from -30° to 30° in the $\phi=0^\circ$ cut when bias voltage of 2.1 V is applied to varactors on reflector.....	104
Fig. 3.49 Simulation results of the RHCP pattern depending on beam steering angle from -30° to 30° in the $\phi=90^\circ$ cut when bias voltage of 2.1 V is applied to varactors on reflector	104
Fig. 3.50 Measurement results of the RHCP pattern depending on beam steering angle from -30° to 30° in the $\phi=90^\circ$ cut when bias voltage of 2.1 V is applied to varactors on reflector.....	105

Fig. 3.51 Measurement results of the AR within beamwidth depending on beam steering angle from -30° to 30° in the $\phi=0^\circ$ cut when bias voltage of 2.1 V is applied to varactors on reflector106

Fig. 3.52 Measurement results of the AR within beamwidth depending on beam steering angle from -30° to 30° in the $\phi=90^\circ$ cut when bias voltage of 2.1 V is applied to varactors on reflector106

List of Tables

Table 2.1 RMS error and standard deviation of beam steering angle according to RL_{\min} , ε_{\max} , θ	21
Table 2.2 Increase level and standard deviation of sidelobe level according to RL_{\min} , ε_{\max} , θ	21
Table 2.3 The magnitude and phase of active reflection coefficient and phase delay error according to each frequency	24
Table 2.4 Beam steering characteristics according to maximum value of active reflection coefficient when steering 30 degree beam	25
Table 2.5 Comparison with previously reported design.....	39
Table 3.1 Dimensions of the designed 2–arm spiral antenna.....	61
Table 3.2 Parameter values of varactor	68
Table 3.3 Dimensions of the proposed design of polarization–dependent phase tunable reflector.	75

Chapter 1. Introduction

1.1. Motivation

Phased array antennas have been used in many military and civil applications such as radar, electronic warfare (EW), and wireless communications [1]. Especially, low-profile wideband phased array antennas are actively studied [2], [3]. It has been a challenge to design wideband and low-profile antennas, which can be surface-mounted on airborne applications such as missile, aircraft, and unmanned aerial vehicle (UAV) to reduce air resistance.

Target application in this thesis is jammer in electronic warfare which is to search the enemy's position and shoot a signal of a large power of a certain frequency to the position by beamforming, so it is designed to selectively choose a frequency in a wide band. To implement a low profile wideband phased array antenna system for the application, two essential technologies are needed. First, wideband beamforming network is required to excite desired signals with multiple antennas in wideband. Phased array antenna with phase shifter can only operate in a narrow band, resulting in a beam squint phenomenon [4], [5]. Therefore, phased array antenna systems need true-time delay (TTD) lines. In order to design a TTD, it is necessary to accurately analyze the factors that may affect the group delay, which is the most important performance indicator of the TTD. An additional issue when designing a TTD considering these factors

is miniaturization. In beamforming systems with relatively low frequency band, such as the S- and C-bands, a long delay time allows beam steering, because the distance between antenna elements is long. In addition, as the number of antenna elements increases, the delay time should be longer, so that miniaturization of TTD is required. Still, designing a TTD with long delay using an IC results in a large insertion loss [6], and the IC process is expensive. Alternatively, a printed circuit board (PCB) process is less expensive, but the resulting TTD can be larger. Aiming to TTD miniaturization using a PCB process, in this paper we designed a multistacked TTD with long delay time by stacking advanced substrates with low dielectric loss [7]

In general, low-profile antennas are antennas with a ground plane in close proximity. Design of low-profile wideband antennas is challenging issue due to the ground plane in close proximity. Hence, second essential technology for low-profile wideband phased array antenna systems is to solve performance degradation problems when forming a unidirectional beam by attaching a PEC reflector close to the wideband antenna. Antennas with unidirectional pattern such as microstrip patch antennas can be operated in a wide band by applying various broadband techniques. However, the bandwidth is relatively smaller than that of other broadband antennas. Wideband antennas such as helical antenna and tapered slot antenna are difficult to be considered low-profile antennas due to their high height and large area. The most applicable type of antennas for low profile wideband

antenna array is spiral antenna which has advantages of simple manufacture process and miniaturization for array. Spiral antenna has the disadvantage of requiring a reflector for unidirectional patterns. Reflections by reflector can lead to performance degradation of matching and AR characteristics. Although several papers have been published, which solve the matching problem using artificial magnetic conductor (AMC) structures such as photonic bandgap (PBG) and electromagnetic bandgap (EBG) for the design of lower height spiral antenna, the papers do not provide AR results [8–11]. In other words, these papers succeeded in transmitting all power in one direction by improving matching, but have different polarization over frequency, which is not suitable for intentional utilization. Many papers have been published that use absorbers or resistors to solve both AR and matching problems [12], [13]. The simple principle is to convert the reflected wave by the reflector into a loss through the absorber or resistor so that it only has a pattern by the upwardly radiated wave. Both AR and matching have been improved but have a serious problem in efficiency. In this thesis, we analyzed the reason why the AR could be degraded by the reflector and based on this, we designed a spiral array antenna with excellent AR and matching characteristics without loss by applying polarization-dependent phase tunable reflector.

1.2. Organization of the Dissertation

The rest of the dissertation is organized as follows.

Chapter 2 presents a study on wideband beamforming network. We analyze three factors that can affect group delay variation. Considering these factors we proposed a TTD design technique for miniaturization.

In Chapter 3, we present the analysis of AR deterioration backed by reflector, and then, propose spiral array antenna backed by polarization-dependent phase tunable reflector to improve AR performance. Verification was accomplished through fabrication and measurement.

Finally, Chapter 4 concludes this dissertation with the summary and discussion on the future work.

Chapter 2. Wideband Beamforming Network

In this chapter, we describe wideband beamforming network, one of two essential technologies for low-profile wideband phased array antenna system. The block diagram of the wideband beamforming network is shown in Fig. 2.1. The most important element in broadband beamforming network is true-time delay (TTD). It is necessary to accurately analyze the factors that can affect the group delay, which is the most important performance indicator of the TTD. An additional issue when designing a TTD considering these factors is miniaturization. In chapter 2.1, we present accurate group delay measurement technique and analysis of factors that affects group delay variation. Chapter 2.2 shows design methodology of TTD for miniaturization. Finally, a summary will be covered in Chapter 2.3.

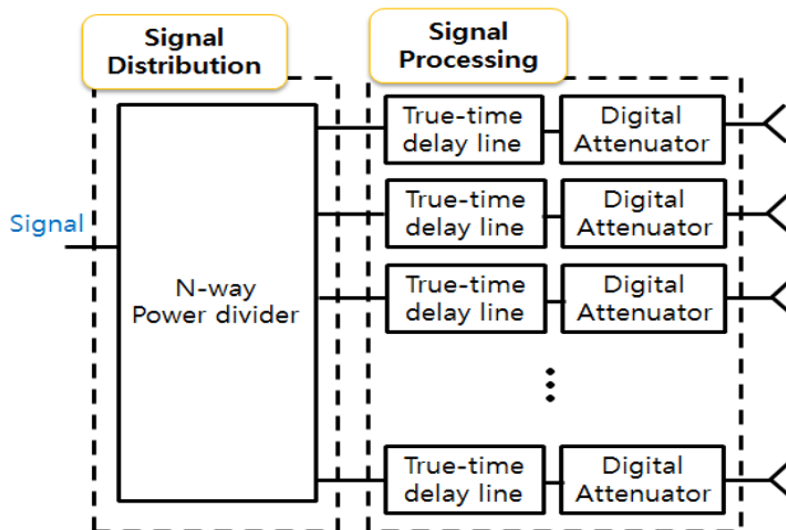


Fig. 2.1. Block diagram of wideband beamforming network.

2.1 Analysis of factors that affects group delay variation in TTD

2.1.1 Accurate group delay measurement technique in vector network analyzer

To determine the effect of phase distortion, a measurement of the group delay is required. Since group delay is defined as the derivative of the phase delay, it is sensitive to noise and requires an accurate measurement method.

The group delay, first introduced in 1930 and widely used in many books, is the negative derivative of phase with respect to angular frequency as follows [14].

$$\tau = -\frac{d\phi(\omega)}{d\omega} = -\frac{1}{2\pi} \frac{d\phi(f)}{df} . \quad (2.1)$$

Since most measurement equipment obtains discrete data over frequency, group delay can be described as follows [15].

$$\tau_{gr} = -\frac{1}{360^\circ} \frac{\Delta\phi}{\Delta f} . \quad (2.2)$$

With the above equation, the group delay measurement accuracy can be expressed by the phase accuracy and aperture as follows.

$$\delta\tau_{gr} = -\frac{1}{360^\circ} \frac{\delta\Delta\phi}{\Delta f} . \quad (2.3)$$

Since the phase accuracy has already been determined within the measurement instrument, the above equation shows that the aperture size determines the group delay measurement accuracy. The aperture size should be determined as follows.

- Desired measurement accuracy
- How rapidly the group delay characteristic of the DUT changes with frequency

Before performing vector network analyzer measurements, accurate calibration should be conducted to eliminate systematic error with time-invariance characteristics commonly known as 12 models [16]. Random errors can be reduced by using the average function. In addition, reducing the IF bandwidth has the disadvantage of longer sweep time, but can reduce measured random noise.

In order to perform wideband beamforming in phased array antenna through true-time delay circuits in S- and C-bands, accuracy of several ps is required [7]. The group delay of the RF switch with two ports was measured to have an accuracy within 10 ps. The device used for the measurement is NJG1802K51, a commercial switch from New Japan Radio. Calculated by Equation (2.3), the aperture size

required to have a group delay accuracy within 5 ps is over 100 MHz. The phase accuracy of the equipment used at this measurement is 0.2° [17]. The measured result were averaged 16 times and the IF bandwidth was set to 1 kHz.

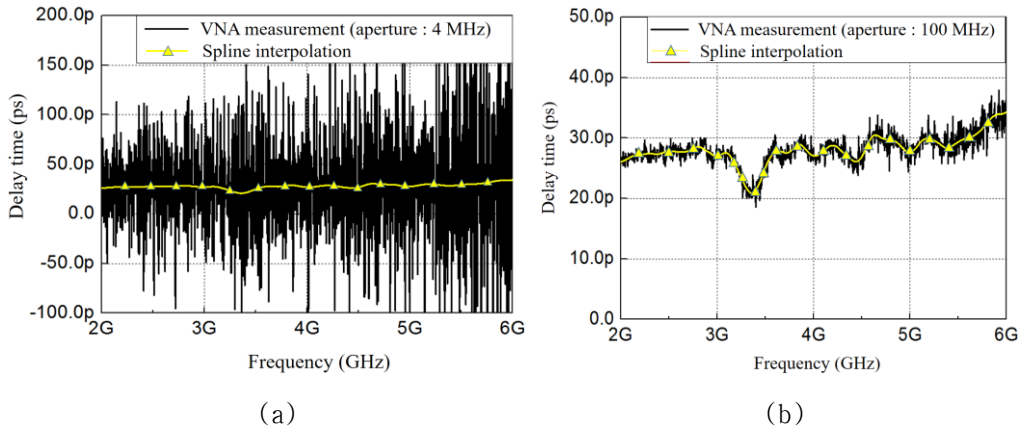


Fig. 2.2. Group delay measurement result (a) aperture: 4 MHz (b) aperture: 100 MHz.

Fig. 2.2(a) shows a group delay measurement with an accuracy of 140 ps when the aperture size is 4 MHz. Accurate result is hidden by noise in Fig. 2.1(a). Fig. 2.2(b) shows a group delay measurement with an accuracy of 5 ps when the aperture size is 100 MHz. The measurement result is compared with the spline interpolation result obtained by post processing to check the accuracy of the result. In Fig. 2.2(b), the measurement result closely matches the spline interpolation and the phase characteristic which was hidden by noise in Fig. 2.2(a) can be recognized.

For accurate group delay measurements, noise should be reduced through correct calibration, data averaging and IF bandwidth reduction. It is essential to determine the appropriate aperture value for the desired accuracy. Additionally, spline interpolation of post processing provides accurate group delay measurements.

2.1.2 Off-switch capacitor resonance

First factor that affects group delay characteristic is off-state capacitor resonance which must be avoided when designing a switched line TTD.

Conventional switched line with single pole double throw (SPDT) switches is shown in Fig. 2.3 (a), which can generate resonance if isolation of switches is around 15 dB which is fair value of isolation. Long line past the off-state capacitor can be seen as parallel resonator by capacitive coupling. The signals of very small magnitude pass through off-switch capacitor but it becomes the reason of resonance and influences phase characteristic between input and output, so that group delay can be distorted. The resonance occurs when the electrical length of transmission line is an integral multiple of half wave length as

$$L_{resonance} = \frac{N\lambda}{2} \quad (2.4)$$

where N is a positive integer.

Conventional switched lines are designed and fabricated with two different delay time difference, 15 ps and 270 ps in Fig. 2.4 and Fig. 2.5 respectively to look into the off-switch capacitor resonance. Simulation has been done in CST Design Studio (DS) which is EM circuit co-simulation tool. After EM simulation, total circuit

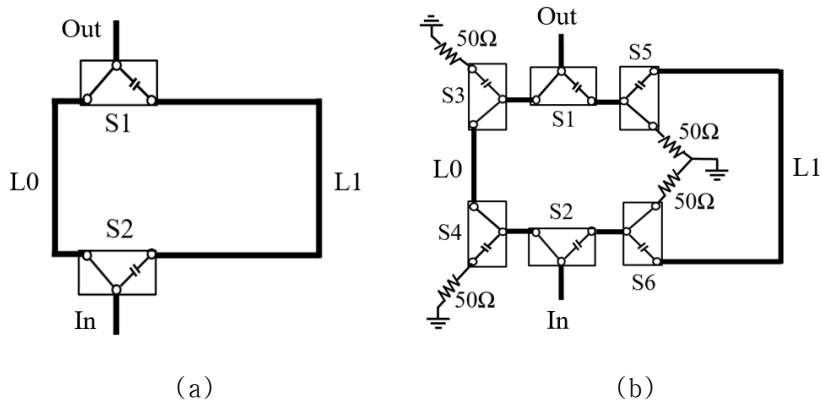


Fig. 2.3. (a) Conventional switched line (b) switched line using cascaded switches.

simulation with S parameter measurement data of SPDT switches (S3P) is performed with fast time for precise results. SPDT switches, NJG1802K51 of New Japan Radio Company are used for design and measurement. This switches have fare isolation of 16 dB at 6 GHz. Long line which has group delay difference of 15 ps in Fig. 2.4 is shorter than half wave length at 6 GHz. Because the range of the S parameter measurement (S3P) of SPDT switches is up to 6 GHz, resonance is not observed in Fig. 2.4. On the other hand, resonance can be observed at around 5 GHz in case of a model with group delay difference of 270 ps in Fig. 2.5.

Avoidance of off-switch resonance is key point of design of TTD lines. To solve this problem TTD using cascaded switches in Fig. 2.3(b) is proposed in [18]. Fig 2.6 shows resonance is effectively removed at around 5 GHz in TTD with cascaded switches. To minimize degradation of TTD performance due to the resonances, switches with an off-state isolation of more than 30 dB are required.

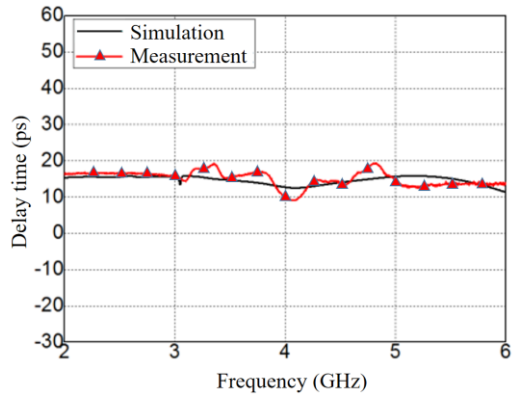


Fig. 2.4. Group delay result of CST simulation and measurement with conventional switched line TTD (delay difference: 15 ps).

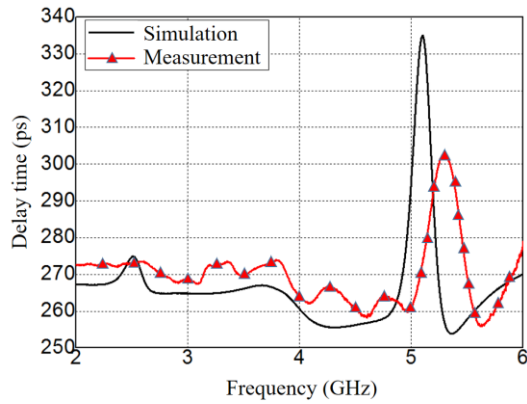


Fig. 2.5. Group delay result of CST simulation and measurement with conventional switched line TTD (delay difference: 270 ps).

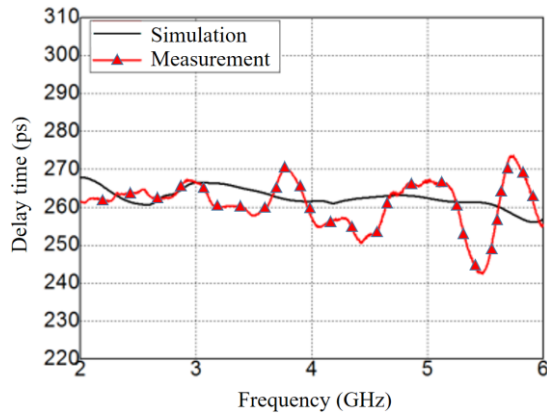


Fig. 2.6. Group delay result of CST simulation and measurement with TTD using cascaded switches (delay difference: 270 ps).

2.1.3 Reflected wave due to discontinuity

Second factor that affects group delay characteristic is reflected wave due to discontinuity, so that matching must be accomplished in all system.

The phase characteristics must have a linear slope in distortionless systems so that group delay is constant for all frequencies. However, any nonlinear phase characteristic over the frequency range will result in group delay variations. For analysis the effects on the group delay caused by reflected waves due to discontinuity and impedance mismatch, transmission line model with discontinuity is proposed as in Fig. 2.7. For simple analysis source impedance and load impedance are matched to Z_0 , which means that $\Gamma_s = \Gamma_L = 0$. All of the reflected waves with different phases caused by discontinuity can be added or subtracted to affect phase of frequency response at port 2, resulting in group delay variation. Summation of all forward waves at the load, can be expressed as

$$V_2^- = (V_1^+ e^{-\gamma_0 l_1} e^{-\gamma_1 l_1} e^{-\gamma_0 l_2} T_1 T_2) + (V_1^+ e^{-\gamma_0 l_1} e^{-\gamma_1 l_1} e^{-\gamma_0 l_2} T_1 T_2)(\Gamma_1 \Gamma_2 e^{-2\gamma_1 l_1}) + (V_1^+ e^{-\gamma_0 l_1} e^{-\gamma_1 l_1} e^{-\gamma_0 l_2} T_1 T_2)(\Gamma_1 \Gamma_2 e^{-2\gamma_1 l_1})^2 + \dots \quad (2.5)$$

where V_1^+ is incident wave generated from a source, Γ_1 and Γ_2 are reflection coefficients at each ends of discontinuity and T_1 and T_2 are transmission coefficients at each ends of discontinuity.

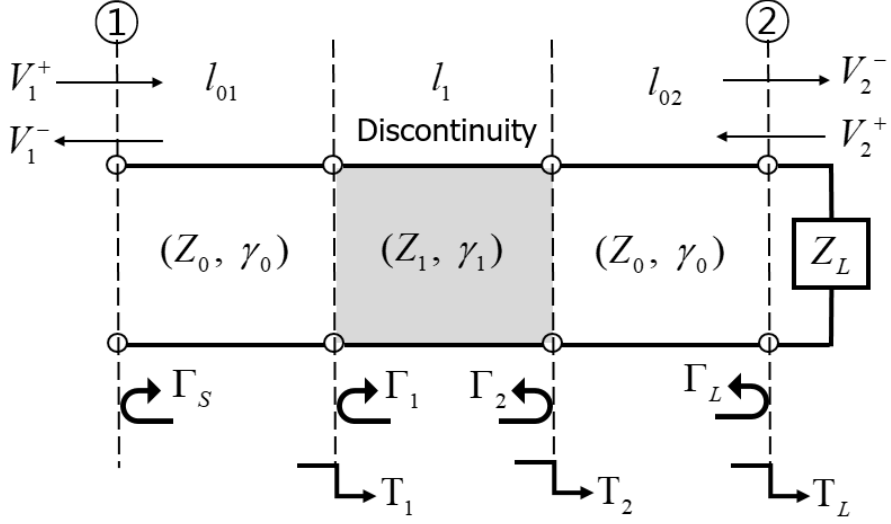


Fig. 2.7. Transmission line model with discontinuity.

To obtain $\angle S_{21}$, S_{21} is calculated as

$$\begin{aligned}
 S_{21} &= \frac{V_2^-}{V_1^+} = (e^{-\gamma_0 l_{01}} e^{-\gamma_1 l_1} e^{-\gamma_0 l_{02}} T_1 T_2) \{1 + (\Gamma_1 \Gamma_2 e^{-2\gamma_1 l_1}) + (\Gamma_1 \Gamma_2 e^{-2\gamma_1 l_1})^2 + \dots\} \\
 &= \frac{T_1 T_2 e^{-\gamma_0 l_{01}} e^{-\gamma_1 l_1} e^{-\gamma_0 l_{02}}}{1 - \Gamma_1 \Gamma_2 e^{-2\gamma_1 l_1}} = \frac{X}{1 - Y}
 \end{aligned} \quad (2.6)$$

The group delay can be expressed by obtaining negative derivative of $\angle S_{21}$ for angular frequency (ω) as

$$T_{GD} = -\frac{\partial \angle S_{21}}{\partial \omega} = -\frac{\partial \phi_x}{\partial \omega} - \frac{\partial \left(\tan^{-1} \left(\frac{|Y| \sin(\phi_Y)}{1 - |Y| \cos(\phi_Y)} \right) \right)}{\partial \omega} \quad (2.7)$$

where ϕ_X and ϕ_Y are phase of X and Y respectively. $|Y|$ variation and phase variations of Γ_1 , Γ_2 , T_1 and T_2 with frequency can be neglected in practical cases and low-loss transmission lines and assuming that β_0 , β_1 change linearly with frequency, we can obtain approximation equation of group delay as

$$T_{GD} = T_0 + T_1 + T_1 \frac{2|Y|\cos\phi_Y}{1-2|Y|\cos\phi_Y} \quad (2.8)$$

where $T_0 = \frac{d\beta_0}{d\omega}l_{01} + \frac{d\beta_0}{d\omega}l_{02}$ and $T_1 = \frac{d\beta_1}{d\omega}l_1$. Third term of (2.8) is group delay variation of reflected wave due to discontinuity in Fig. 2.7 as follows.

$$T_{GDV} = T_1 \frac{2|Y|\cos\phi_Y}{1-2|Y|\cos\phi_Y}. \quad (2.9)$$

In design of TTDs, group delay variation can be caused by reflected waves due to discontinuity, so matching of network is important in TTD design.

2.1.4 Antenna impedance variation over frequency

Jammers in electronic warfare are designed to enable wideband beamforming. It is necessary to search the enemy's position and shoot a signal of a large power of a certain frequency to the position in jammer, which is designed to selectively choose a frequency in a wide band. When designing a TTD to enable beam steering in a wide band, it is designed to avoid the influence and resonance caused by multiple reflected waves. However, even when designing a TTD with no phase distortion, the phase delay characteristics may be affected by the antenna impedance. In the case of narrow-band antennas, the magnitude of S_{11} can be reduced to more than -20 dB, but when designing a wide-band antenna, matching at wide bands inevitably increases the maximum antenna reflection coefficient.

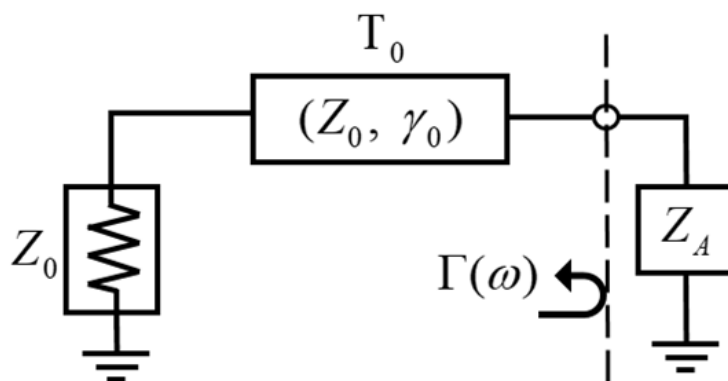


Fig. 2.8. Transmission line model with delay time of T_0 for antenna load of Z_A .

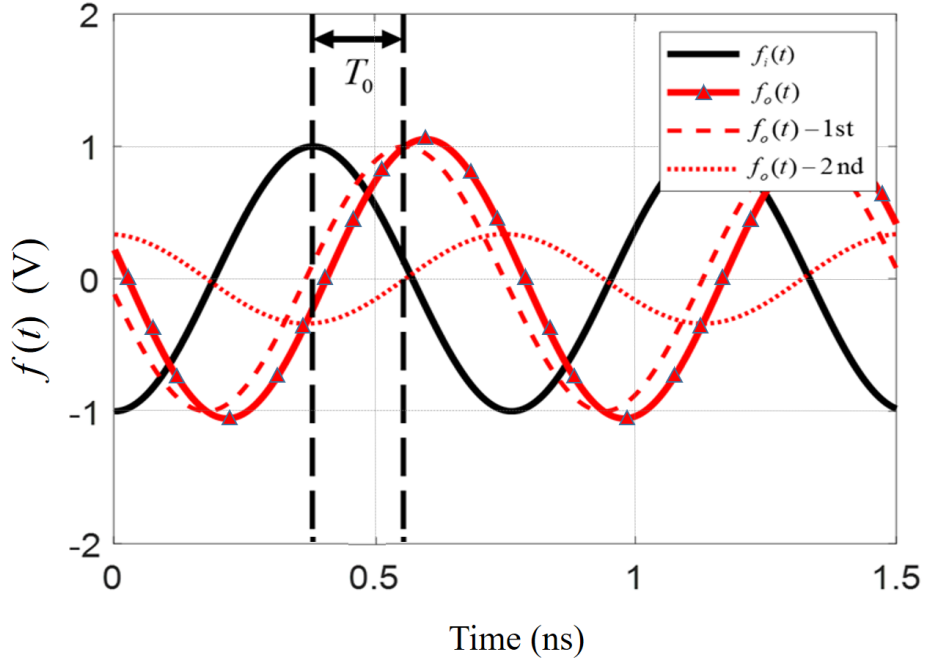


Fig. 2.9. First term and second term of equation (2.11).

In the phased array antenna, the active reflection coefficient reflecting all characteristics due to mutual coupling must be considered. Impedance including all these effects was modeled as Z_A shown in Fig. 2.8.

As shown in Fig. 2.9, when the reflection coefficient is $\Gamma(\omega)$ and the input voltage signal of $f_i(t)$ is transmitted to the transmission line with the delay time of T_0 , the output voltage signal of the $f_o(t)$ is affected by the magnitude and phase of the $\Gamma(\omega)$ as follows.

$$F_o(\omega) = F_i(\omega)e^{-j\omega T_0}[1 + \Gamma(\omega)], \quad (2.10)$$

$$f_o(t) = f_i(t - T_0) + f_i(t - T_0) * F^{-1}[\Gamma(\omega)]. \quad (2.11)$$

Equation (2.10) shows that reflection itself can affect the phase of the output signal. This can be overlooked when the input and output are terminated with Z_0 when designing and measuring the TTD. In the case of generating a CW signal in a broadband antenna system, the output voltage is described as follows.

$$f_o(t) = \sin[\omega(t - T_0)] + |\Gamma| \sin[\omega(t - T_0) + \angle\Gamma], \quad (2.12)$$

$$f_o(t) = \sqrt{1 + |\Gamma|^2 + 2|\Gamma| \cos \angle\Gamma} \sin[\omega(t - T_0) + \varepsilon], \quad (2.13)$$

$$\varepsilon = \tan^{-1} \left(\frac{|\Gamma| \sin \angle\Gamma}{1 + |\Gamma| \cos \angle\Gamma} \right), \quad (2.14)$$

$$RL = -20 \log |\Gamma| \quad (\text{dB}). \quad (2.15)$$

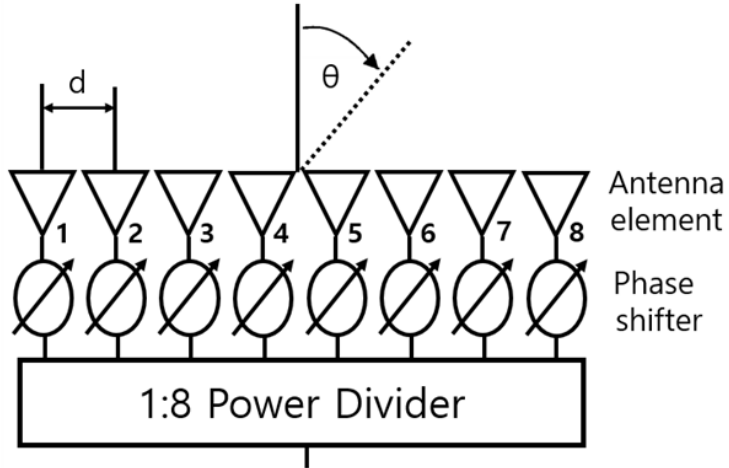


Fig. 2.10. 1D linear phased array antenna system.

Depending on the magnitude and phase of the reflection coefficient, phase delay error occurs. Reflection coefficient can be expressed as a reflection coefficient as shown in (2.15). The maximum reflection coefficient is determined by the antenna impedance. It was confirmed that the maximum phase delay error of 18.5° corresponding to 0.051λ occurs when RL_{\min} is 10 dB and the maximum phase delay error of 26.5° corresponding to 0.074λ when RL_{\min} is 7 dB.

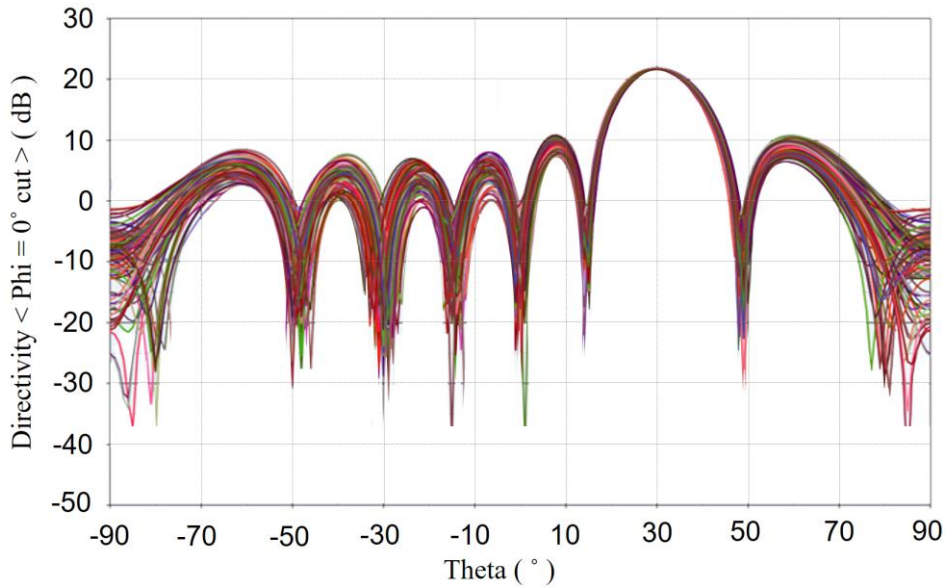


Fig. 2.11. Monte Carlo simulation 100 sampling result with beam steering angle of 30° at $RL_{\min} = 7$ dB, $\epsilon_{\max} = 26.5^\circ$ of 8 elements uniform array.

Monte Carlo simulations were performed to investigate the effect of phase delay error on the beam steering angle and side lobe level

due to antenna impedance. As shown in Fig. 2.10, eight antennas are assumed to be spaced at half wavelength intervals. The phase values required for beam steering angle are added with the maximum phase delay error with uniform distribution in Monte Carlo simulation. The theoretical value of the side lobe level for an eight-element uniform array is -12.8 dB. Fig. 2.11 shows the result of 30° beam steering through Monte Carlo simulation when RL_{\min} is 7 dB and ϵ_{\max} is 26.5° . Due to the phase error caused by Z_A , the beam steering angle is not stable and the side lobe level rises as shown in Fig. 2.11. The RMS error of the beam steering angle and the increase of the side lobe level according to the respective RL_{\min} , ϵ_{\max} , and θ are summarized in Table 2.1 and Table 2.2. In the case of Taylor taper, which lowers the side lobe level by -20 dB, the side lobe increase is 4.32 dB and the standard deviation is 0.85 dB when beam steering to 30° with ϵ_{\max} of 26.5° . Since beam steering can be affected by the reflection coefficient by Z_A , it is important to ensure that the maximum value of the active reflection coefficient value is not too large when designing the antenna with broadband.

Table 2.1. RMS error and standard deviation of beam steering angle according to RL_{\min} , ϵ_{\max} , θ .

	Steering angle	Steering angle	
		RMS error	Standard deviation
$RL_{\min} = 10$ dB, $\epsilon_{\max} = 18.5^\circ$	$\theta = 0^\circ$	0.28°	0.14°
	$\theta = 10^\circ$	0.19°	0.19°
	$\theta = 20^\circ$	0.20°	0.20°
	$\theta = 30^\circ$	0.22°	0.22°
$RL_{\min} = 7$ dB, $\epsilon_{\max} = 26.5^\circ$	$\theta = 0^\circ$	0.41°	0.21°
	$\theta = 10^\circ$	0.28°	0.28°
	$\theta = 20^\circ$	0.34°	0.33°
	$\theta = 30^\circ$	0.3°	0.3°

Table 2.2. Increase level and standard deviation of sidelobe level according to RL_{\min} , ϵ_{\max} , θ .

	Steering angle	Sidelobe level	
		Increase level	Standard deviation
$RL_{\min} = 10$ dB, $\epsilon_{\max} = 18.5^\circ$	$\theta = 0^\circ$	0.74 dB	0.34 dB
	$\theta = 10^\circ$	0.74 dB	0.31 dB
	$\theta = 20^\circ$	0.80 dB	0.35 dB
	$\theta = 30^\circ$	0.82 dB	0.32 dB
$RL_{\min} = 7$ dB, $\epsilon_{\max} = 26.5^\circ$	$\theta = 0^\circ$	1.08 dB	0.42 dB
	$\theta = 10^\circ$	1.12 dB	0.51 dB
	$\theta = 20^\circ$	1.21 dB	0.50 dB
	$\theta = 30^\circ$	1.18 dB	0.50 dB

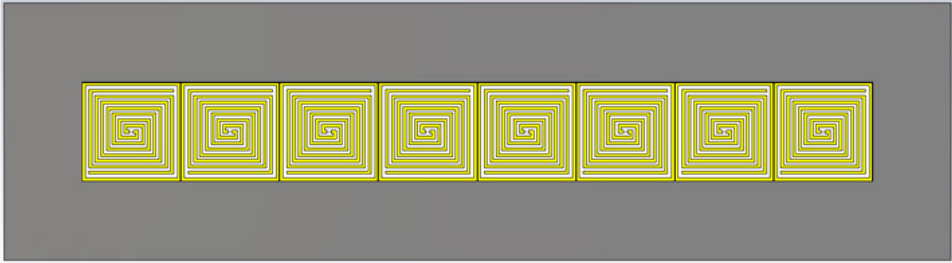


Fig. 2.12. Linear array model with spiral antenna of 8 elements.

The actual antenna is designed to verify the effect of the phase delay error on the antenna impedance, which was examined through Monte Carlo simulation. The reason for selecting the spiral antenna is that the active reflection coefficient may be partially enlarged in order to make the overall matching within a wide band. As shown in Fig. 2.12, the designed antenna is a rectangular two-arm spiral antenna, and the gap loading is added to the outside for miniaturization [19]. The spacing of antenna elements is 37.5 mm, half wavelength at 4 GHz, and it is designed to radiate to one side with a reflector.

Without mutual coupling between the antennas, the phase error resulting from the antenna impedances of all antennas is equally applied and does not affect beam steering. However, with mutual coupling between the antennas, even if the same antennas are arranged, the active reflection coefficients at the same frequency may be different in magnitude and phase, and thus may be distorted

at the desired beam steering angle, and the side lobe level may be increased. After excitation of signal required for 30° beam steering for each antenna, the active reflection coefficient magnitude and phase of each antenna element were extracted. As expected, it was confirmed that the magnitude and phase of each antenna element are different and the phase error occurs due to mutual coupling between antennas. The phase error is summarized in Table 2.3. Table 2.4 shows the characteristics of the beam steering with the phase error in Table 2.3. At 3 GHz and 4 GHz, the maximum values of the active reflection coefficients are -8.8 dB and -13.4 dB, respectively, and the maximum phase delay errors are 13.9° and 7.2° , respectively. The beam steering angle errors are 1° and 0° , respectively, and the side lobe level increases are 1.6 dB and 0.67 dB, respectively. Since this result is within the range expected by Monte Carlo simulation, the expectation of the phase delay error due to the antenna impedance was accurate. In addition, in the case of 2 GHz signal with maximum active reflection coefficient of -4.3 dB, the maximum phase delay error is -60.4° , the beam steering angle error is -2° , and the sidelobe level increase is 5.03 dB. If the active reflection coefficient is higher than -7 dB, the sidelobe level is greatly increased and the beam steering angle can deviate from the expected angle. Through the simulation results, it was confirmed that the phase error caused by the reflection coefficient due to the antenna impedance affects the beam steering angle and the side lobe level of the beam pattern in the actual antenna model.

Table 2.3. The magnitude and phase of active reflection coefficient and phase delay error according to each frequency.

		Number of Element	Active reflection coefficient		phase delay error
			magnitude	phase	
Beam steering angle : 30 °	2 GHz	1	-5.9 dB	-31.8 °	26.5 °
		2	-4.3 dB	-32.7 °	4.9 °
		3	-5.8 dB	-47.2 °	-60.4 °
		4	-10.5 dB	-38.2 °	34.8 °
		5	-6.9 dB	-37.9 °	-51.0 °
		6	-6.4 dB	-63.0 °	-24.4 °
		7	-8.5 dB	-43.7 °	-13.9 °
		8	-9.9 dB	-37.4 °	9.1 °
	3 GHz	1	-14.5 dB	-94.5 °	-7.0 °
		2	-11.5 dB	-85.4 °	-12.7 °
		3	-12.6 dB	-80.6 °	8.1 °
		4	-12.5 dB	-101.0 °	13.9 °
		5	-8.8 dB	-91.3 °	11.6 °
		6	-9.7 dB	-65.8 °	10.4 °
		7	-14.9 dB	-66.8 °	-13.9 °
		8	-12.6 dB	-98.4 °	13.9 °
	4 GHz	1	-15.6 dB	114.5 °	5.8 °
		2	-16.9 dB	81.0 °	4.7 °
		3	-14.6 dB	76.8 °	-5.8 °
		4	-14.4 dB	80.8 °	7.0 °
		5	-13.9 dB	80.2 °	7.2 °
		6	-13.4 dB	90.4 °	-7.0 °
		7	-16.7 dB	99.1 °	5.8 °
		8	-15.4 dB	55.4 °	-5.8 °

Table 2.4. Beam steering characteristics according to maximum value of active reflection coefficient when steering 30 degree beam.

	Beam steering angle : 30 °		
	2 GHz	3 GHz	4 GHz
maximum of ARC magnitude value	-4.3 dB	-8.8 dB	-13.4 dB
maximum phase delay error	-60.4 °	13.9 °	7.2 °
Beam steering angle error	-2 °	1 °	0 °
Sidelobe level increase	5.03 dB	1.6 dB	0.67 dB

2.2 Design of 7-bit multistacked true-time delay for miniaturization

TTDs must present several features such as low insertion loss, long total delay, low phase distortion, and compact size. In beamforming systems with relatively low frequency band, such as the S- and C-bands, a long delay time allows beam steering, because the distance between antenna elements is long. In addition, as the number of antenna elements increases, the delay time should be longer. Still, designing a TTD with long delay using an IC results in a large insertion loss, and the IC process is expensive. Alternatively, a PCB process is less expensive, but the resulting TTD can be larger.

Aiming to TTD miniaturization using a PCB process, in this study we designed a multistacked TTD with long delay time by stacking advanced substrates with low dielectric loss.

2.2.1 Design considerations

Generally, phase shifters are used for narrowband operation of phased array antennas, as using them for wideband distorts the beam steering angle by a phase depending on frequency, conforming the beam squint phenomenon. TTD lines are used to prevent this phenomenon. Fig. 2.13 shows a linear array antenna with distance d between antennas. The time delay between each antenna in free space can be expressed as

$$\Delta t = \frac{d \sin \theta}{c} \quad (2.16)$$

where c is the speed of light and θ is the scanning angle.

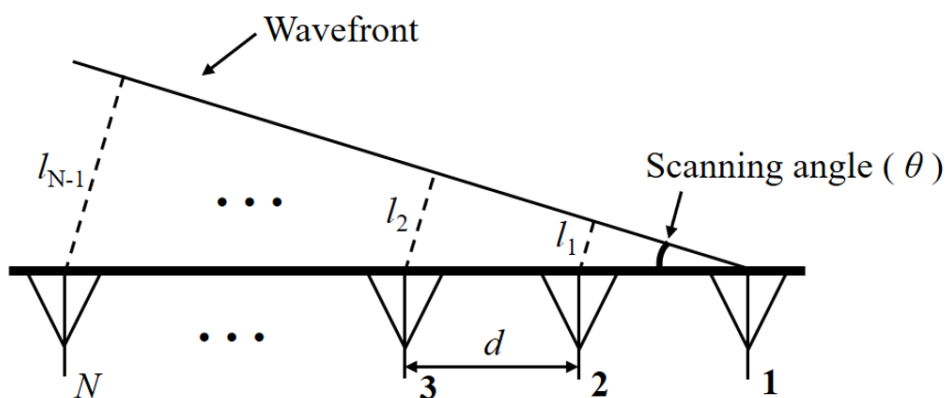


Fig. 2.13. Linear array with N elements.

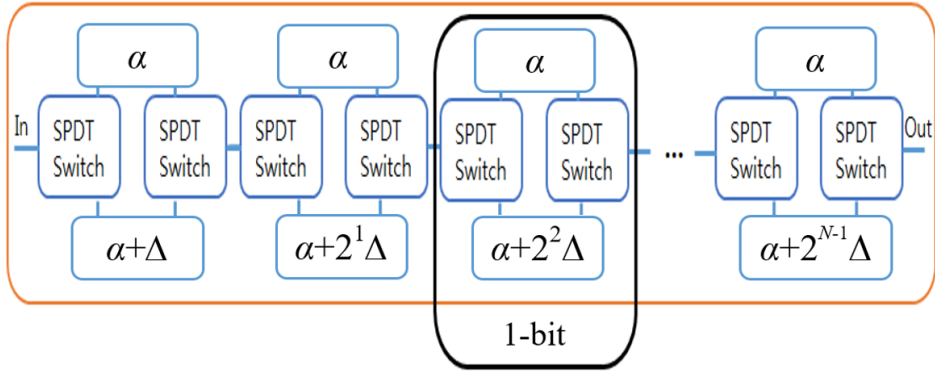


Fig. 2.14. Block diagram of TTD line.

Fig. 2.14 illustrates a switched line structure typically used in TTD lines. Two single pole double throw (SPDT) switches are needed for a one-bit line. In Fig. 2.14, α is a reference line and Δ is a line with a delay time longer than the reference line by a minimum amount (i.e., resolution time). By arranging doubling Δ in series, it is possible to efficiently construct a TTD line with minimum delay time resolution.

Several considerations are necessary in the design of a switched line TTD as mentioned in the previous chapter. First, resonance of line coupled by the off-state capacitor of the SPDT should be avoided [18]. Resonance can cause delay distortion when the electrical length of a line connected through this capacitor is an integer multiple of a half wavelength. To prevent this distortion, a switch with an off-state isolation of at least 30 dB should be used. We prevented resonance by using the HMC1118 switch (Analog Devices, Inc., Norwood, MA, USA) that provides excellent isolation in the desired frequency band

[20]. In addition, the reflected wave generated by discontinuity and impedance mismatch can affect the phase between input and output, which can in turn deteriorate the TTD performance [21]. Hence, multistacked fabrication should consider the signal passing through vias and matching should be carefully performed.

2.2.2 TTD resolution and number of bits

Generally, phase shifters are used for narrowband operation of phased array antennas, as using them for

When designing a TTD line for wideband beam steering of an N -element array antenna, the required maximum delay and number of bits are determined by the desired beam steering angle and resolution [22]. We designed a TTD for an eight-element linear array operating at maximal beam steering angle of 60° and resolution of 5° . The frequency band was set to 1–7 GHz according to the operating band of the switches. As shown in Fig. 2.13, the minimum value of the electrical length in air is $l_1 = d \times \sin(5^\circ)$ and the maximum value is $l_7 = 7d \times \sin(60^\circ)$. Generally, when designing a broadband antenna, the distance between antennas at the lowest frequency should have a relatively small wavelength to avoid the generation of a grating lobe at the highest frequency [23]. Therefore, we set the distance between antennas to 37.5 mm, which is 0.125 of the wavelength of 1 GHz. In this case, the delay time has a minimum of 10.9 ps and a maximum of 757.8 ps. The number of bits of the TTD is at least seven, as determined by $l_7 \leq l_1 \times 2^n$. Hence, we designed a seven-bit TTD with minimum and maximum delay time of 8 and 1016 ps, respectively. We performed electromagnetic simulation, including measurement results of the switch, using CST Design Studio (Computer Simulation Technology GmbH, Darmstadt, Germany).

For miniaturization, we implemented a multistacked structure. In

the first layer, the switch was placed on the substrate by soldering, and microstrip lines were arranged to form short lines. The two longest lines, corresponding to the two most significant bits, were implemented using stripline in the second and third layers to reduce the total form factor of the TTD. The cross-section of the fabricated TTD layers is shown in Fig. 2.15, detailing the layer characteristics.

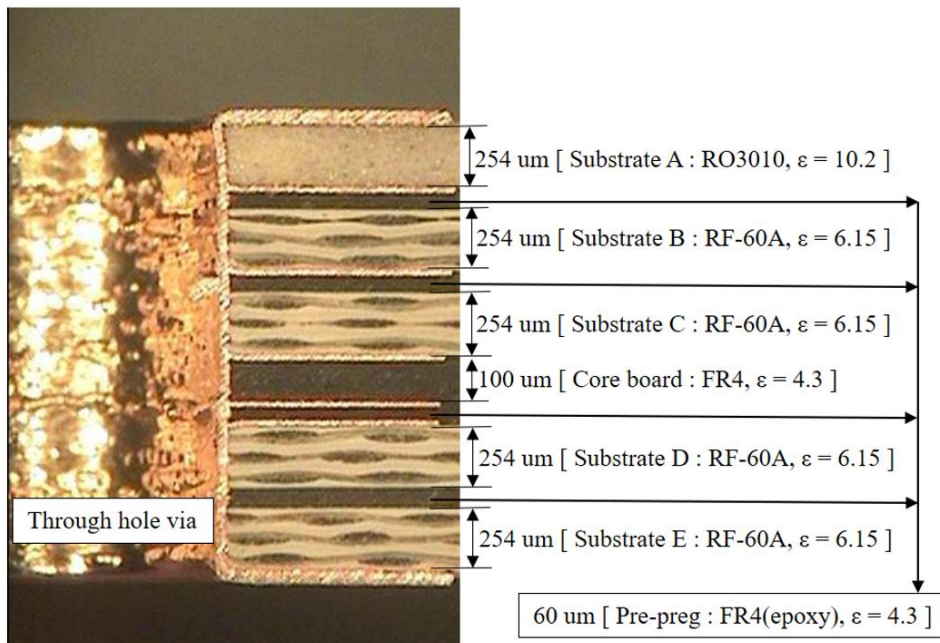


Fig. 2.15. Cross-sectional view of multistacked PCB and layer characteristics.

2.2.3 Optimal design of signal vias

The most important part of stacking advanced substrates is the design of signal via. As vias introduce discontinuity in the transmission line, a matching structure is required to mitigate the reflected wave. In fact, multiple reflected waves can be added at the output, resulting in phase distortion of TTD. As shown in Fig. 2.16, we designed three types of signal vias. Specifically, ViaA is intended for transition from the top microstrip line to the microstrip line of the motherboard. ViaB is intended for transition from the top microstrip line to the stripline of the second layer, and ViaC for transition from the top microstrip line to the stripline of the third layer.

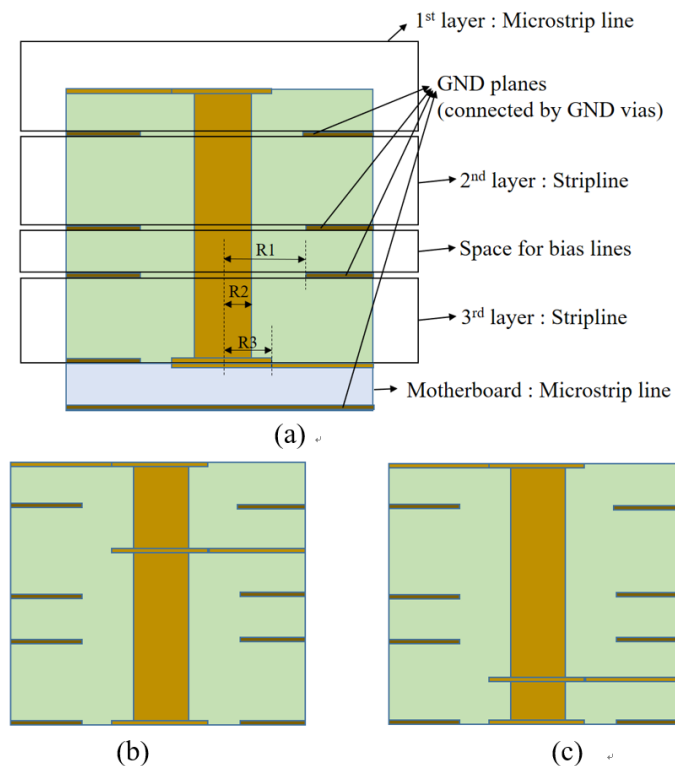


Fig. 2.16. Side-view of vias: (a) ViaA, (b) ViaB, and (c) ViaC.

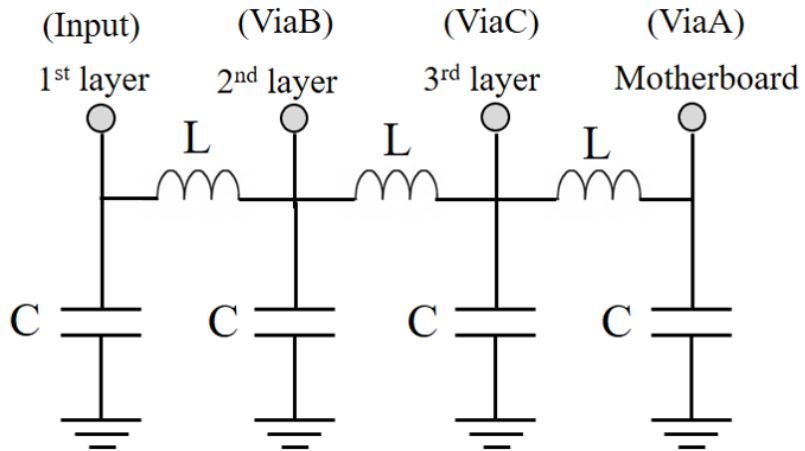


Fig. 2.17. Equivalent circuit of a via.

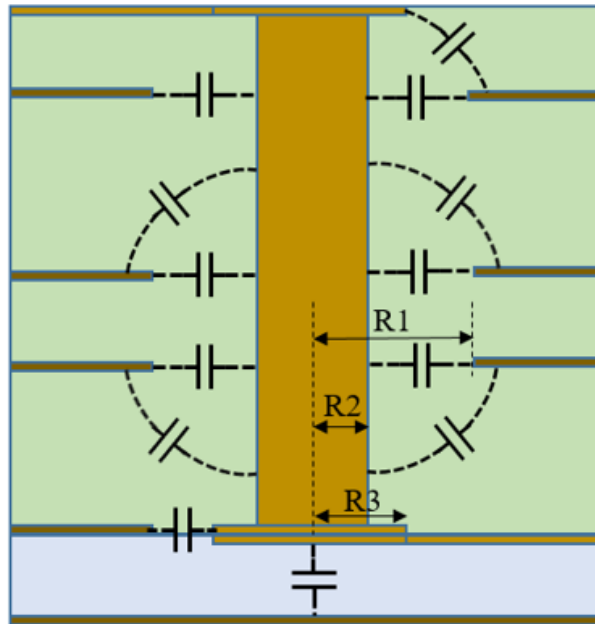


Fig. 2.18. Capacitance of each via.

The signal via circuit model is shown in Fig. 2.17 [24]. Series L is the inductance of the via body and shunt C is added to the various capacitance values, as shown in Fig. 2.18. The impedance of the signal vias should match the wideband load impedance to ensure good

signal transition. The two most significant bits were composed of striplines in the second and third layers to reduce the total area using ViaB and ViaC, respectively. By adjusting the inductance and capacitor values by changing the radii of anti-pad ($R1$), via ($R2$), pad ($R3$), and distance between vias enables impedance matching. The most dominant factor is the radius of anti-pad ($R1$), which is the distance between the ground plane and the signal via, i.e., the diameter of the hole in the ground conductor plate to allow the via to pass through ground.

Fig. 2.19 shows the measured matching characteristics of signal vias while changing the radius of the anti-pad. The optimal result can be obtained by adjusting this radius, as confirmed from the measurements. The black solid line in Fig. 2.19 shows the radii of anti-pad with the best matching conditions in the bandwidth of 1–7 GHz, being 0.85 mm for ViaA, 1.2 mm for ViaB, and 1 mm for ViaC. Notice that the optimal radii of anti-pad depends on the type of via.

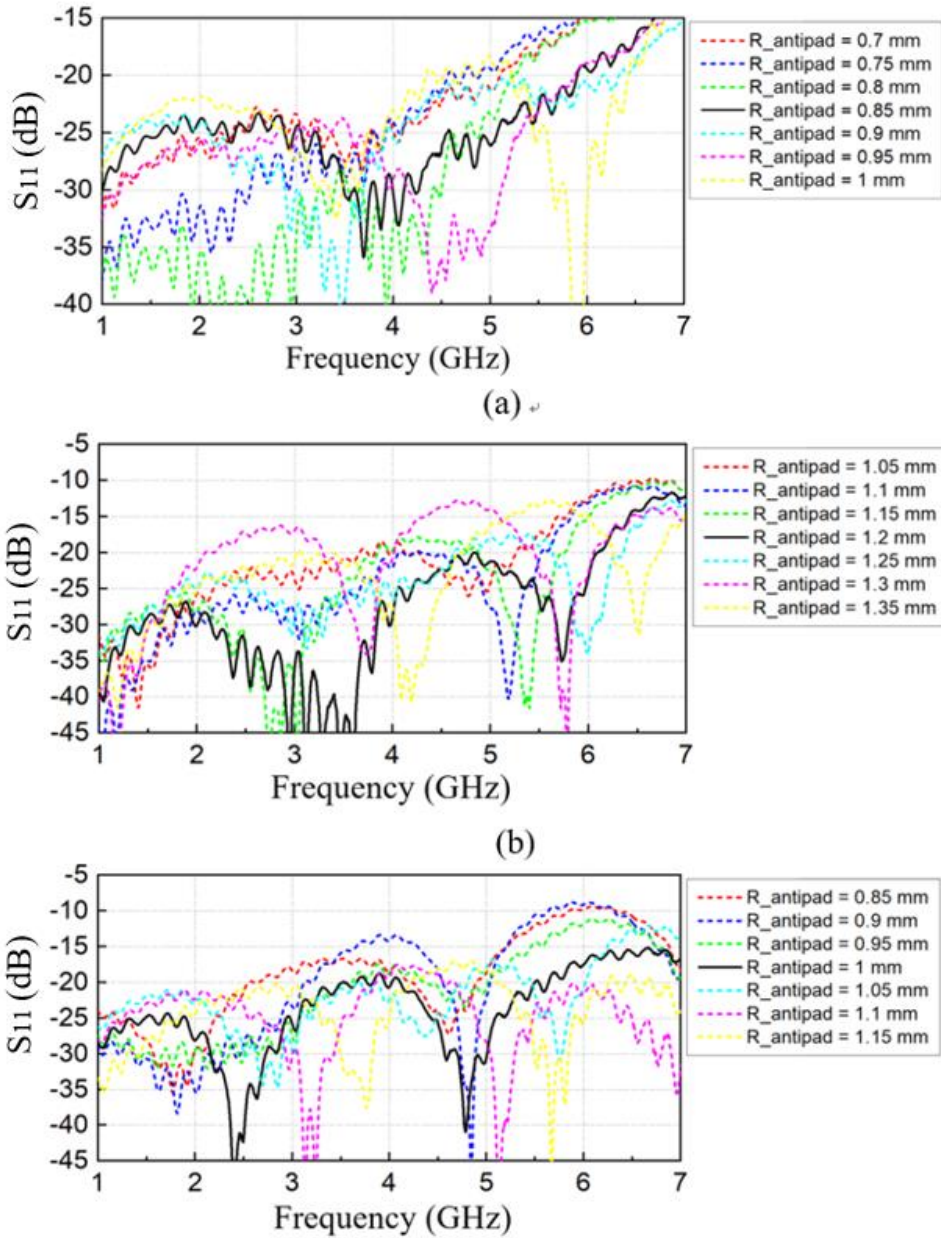


Fig. 2.19. Measurements of signal vias according to radius of anti-pad: (a) ViaA, (b) ViaB, and (c) ViaC.

2.2.4 Fabrication and measurement results

We fabricated the proposed seven-bit multistacked TTD in a PCB process, and its photo is shown in Fig. 2.20. The resulting TTD has an area of $36.6 \times 19.4 \text{ mm}^2$. The power consumption of the SPDT switches for all delay states is 0.65 mW at 3.3 V supply.

The measured input and output reflection coefficients of the major delay states are shown in Fig. 2.21(a). The measured input/output reflection coefficient is better than -12.1 dB across the bandwidth of 1–7 GHz. The insertion losses of the TTD are shown in Fig. 2.21(b). The losses of the 14 switches used in the TTD are 7 dB at 1 GHz and 9 dB at 7 GHz, and additional loss occurs over the lines and vias.

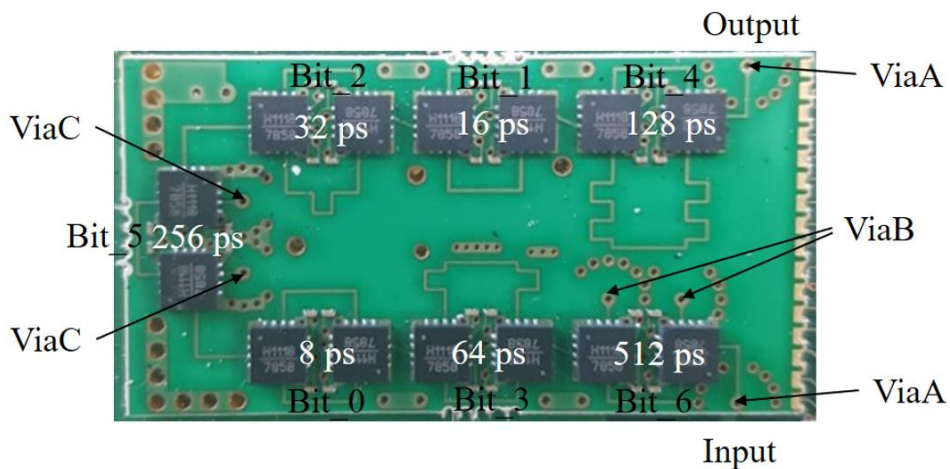


Fig. 2.20. Fabricated TTD in PCB process.

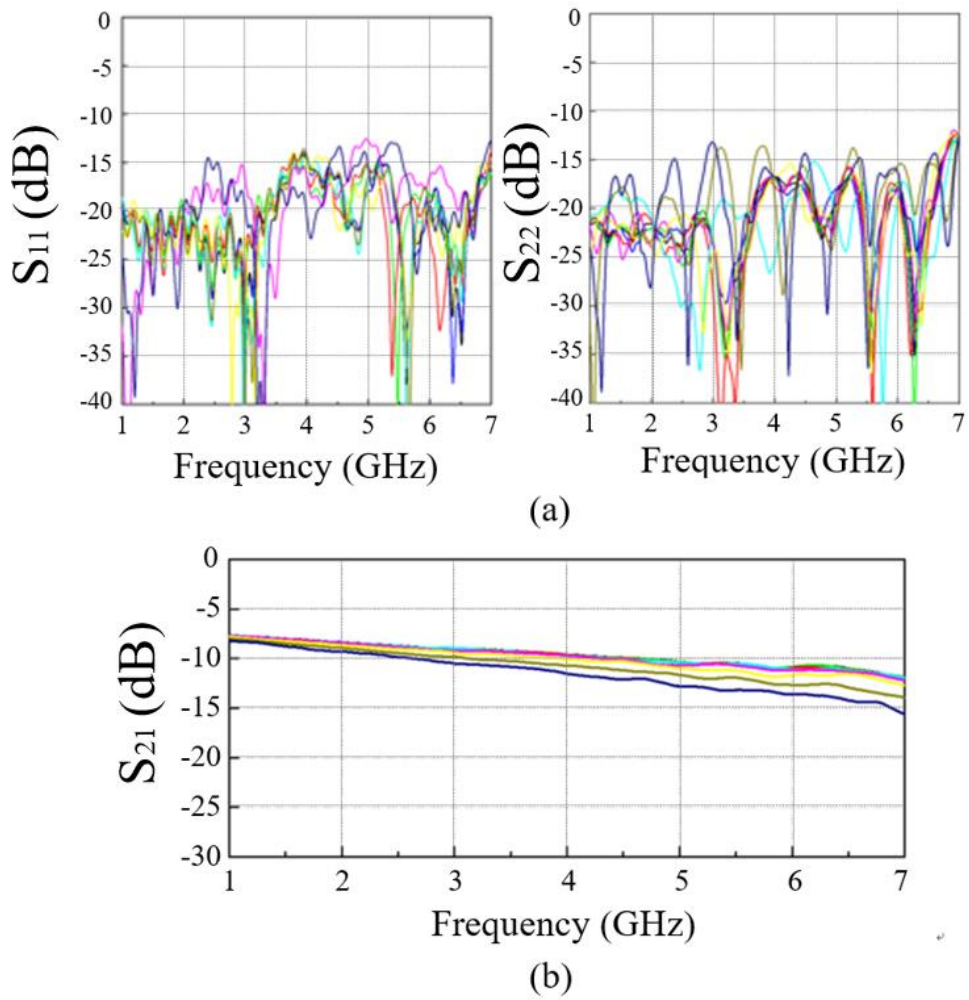


Fig. 2.21. Measured (a) input/output reflection coefficients and (b) insertion loss of the TTD for the main bits.

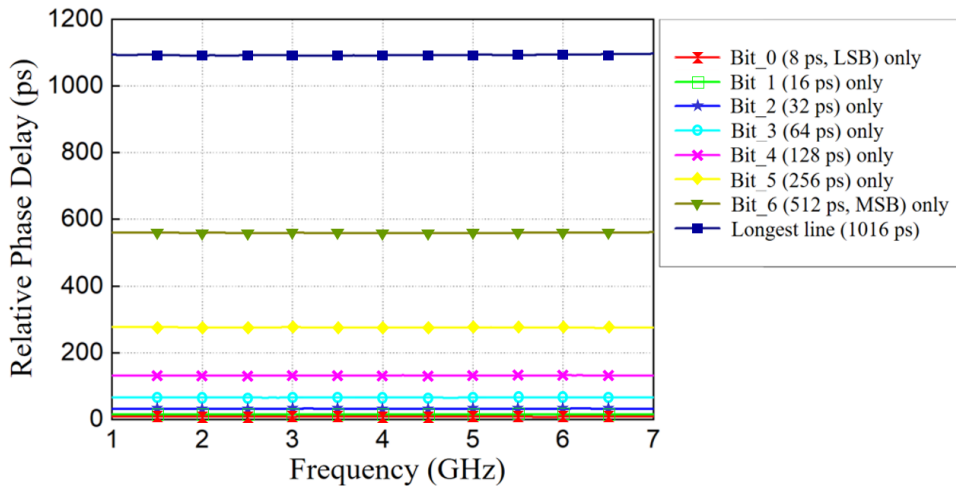


Fig. 2.22. Measured phase delay with respect to the shortest delay state of the TTD.

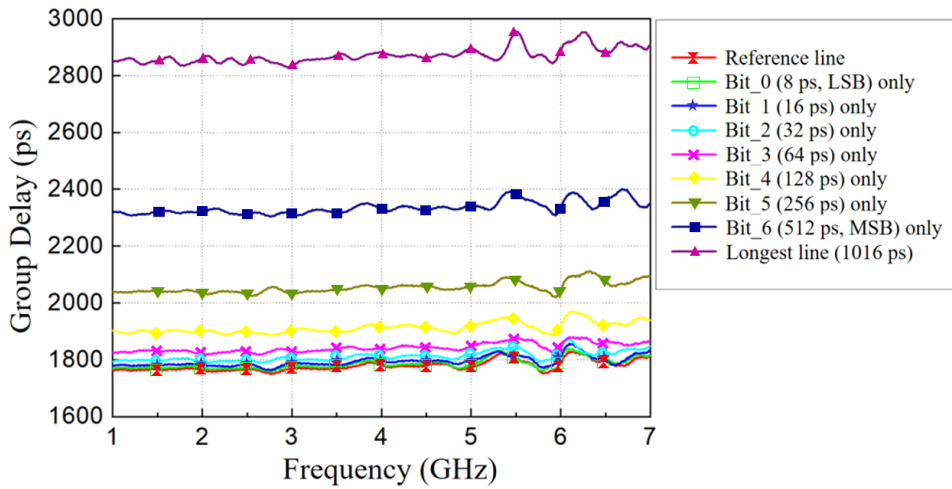


Fig. 2.23. Measured group delay of the TTD.

The measured phase delay with reference to the shortest delay of the TTD is shown in Fig. 2.22, with standard deviation of the TTD for all the states below 1.4 ps. The measured group delay of the TTD is shown in Fig. 2.23, with standard deviation of the TTD for all the states below 19 ps, which is 1.87 % of the maximum group delay.

The measured performance is summarized and compared with that of other TTD circuits in Table 2.5. Our approach shows an improved performance regarding a figure of merit defined as the relative delay divided by the insertion loss at the longest delay state, a large number of bits of resolution, and low power consumption.

Table 2.5. Comparison with previously reported design.

	[6]	[25]	[22]	[26]	[27]	This work
Substrate	CMOS	CMOS	PHEMT	GaAs	PCB	PCB
Frequency (GHz)	1-20	1-21	2-20	0-40	8-12	1-7
Maximum delay (ps)	400	274	145	87	97.3	1016
Insertion loss @ 7 GHz (dB)	24.5	11.2	11	2.5	3.7	15.6
FoM @ 7 GHz (ps / dB)	16.3	24.5	13.2	34.8	26.3	65.1
Number of bits	6	3	6	4	5	7
Size (mm ²)	4	1.1	5.6	30	4225	710
DC power (mW)	2.6-6	2-6.2	30	n/a	n/a	0.65

FoM, figure of merit

2.2.5 Verification of TTD

To verify the fabricated TTD, a wideband antenna system was constructed. The implemented antenna system consists of 24 antennas, 24-way broadband power divider, 24 TTDs and 24 digital attenuators. The 24-way antenna is designed by combining one 3-way power divider and three 8-way power dividers. The substrate was Duroid 5880 and 31 mil (0.787 mm) thick. The CST model and fabricated model of the power divider are shown in Fig. 2.24.

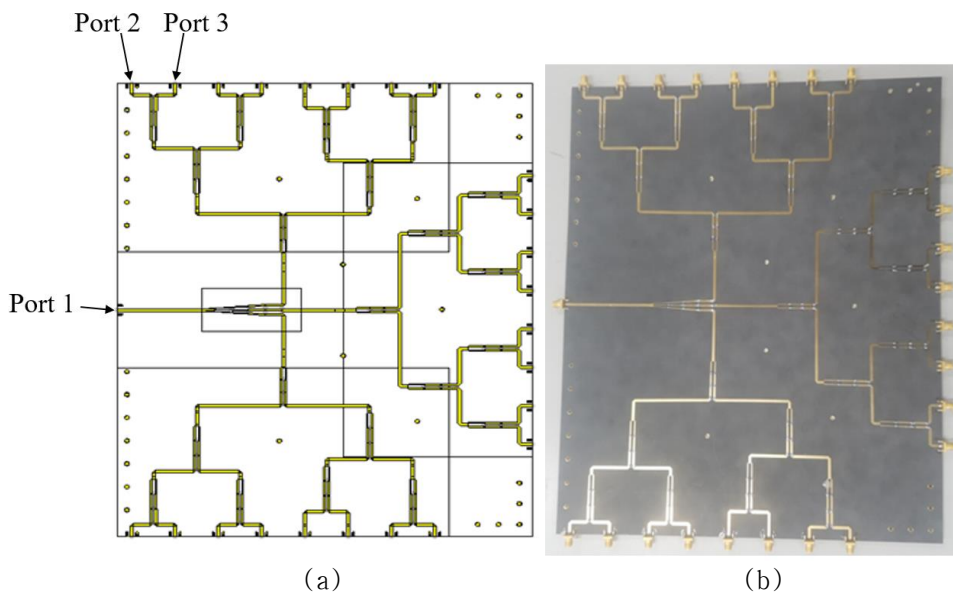


Fig. 2.24. 24-way wideband power divider (a) CST simulation model and (b) fabricated model (393 x 318 mm²).

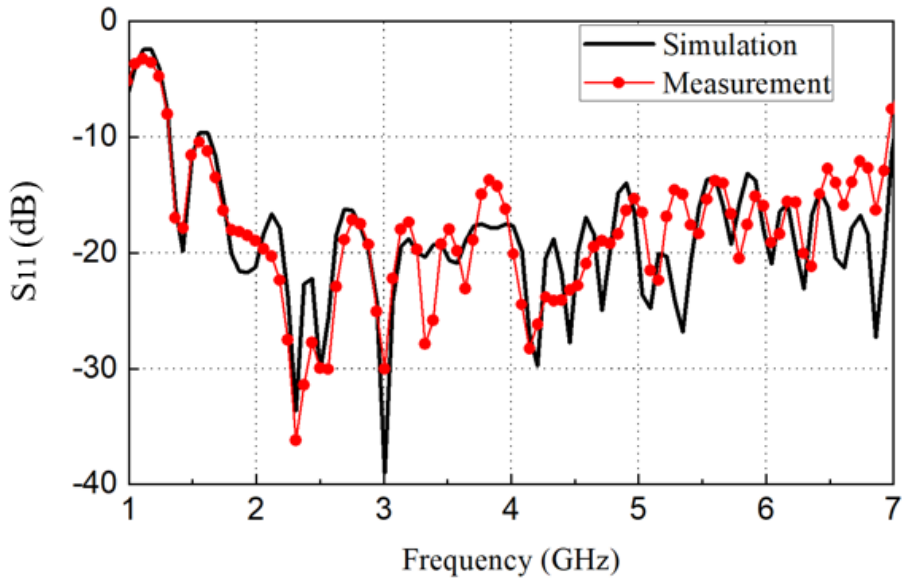


Fig. 2.25. Simulation and measurement results of input reflection coefficient of 24-way wideband power divider.

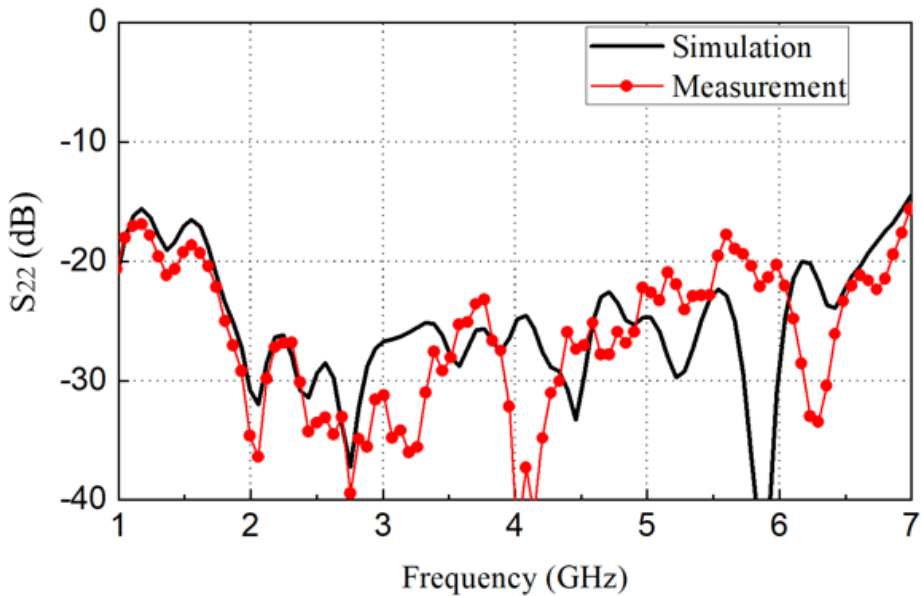


Fig. 2.26. Simulation and measurement results of output reflection coefficient of 24-way wideband power divider.

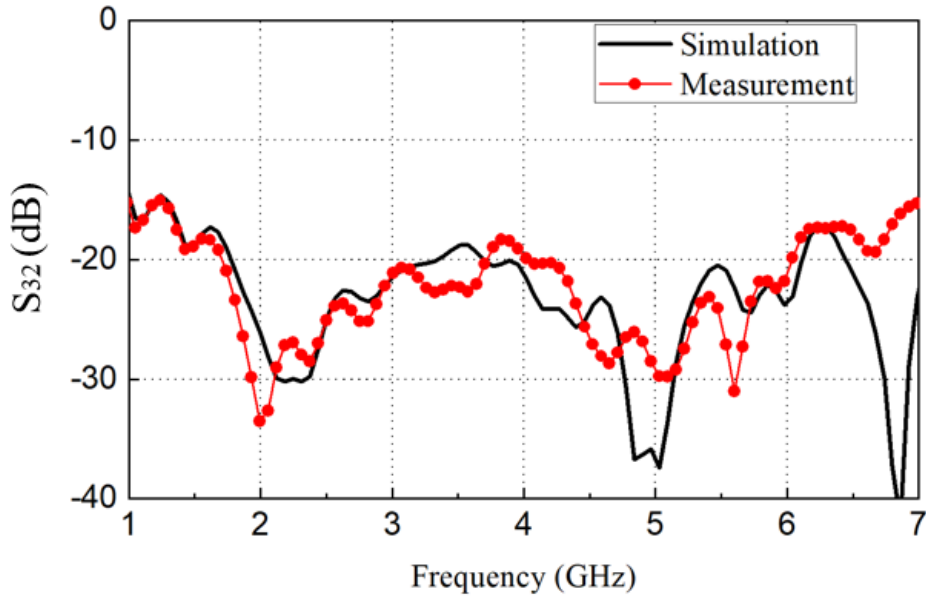


Fig. 2.27. Simulation and measurement results of isolation between adjacent output ports of 24-way wideband power divider.

It can be seen that the measurement results are consistent with the simulation results. Fig. 2.25 and Fig.2.26 show that the input and output reflection coefficient results have values lower than -14 dB within the entire frequency band. The isolation is kept below -20 dB within the entire frequency band in Fig. 2.27. The insertion loss at 2 GHz was 0.4 dB and 0.7 dB in simulation and measurement, respectively, which is consistent with connector loss values not included in the simulation model. The insertion loss at 6 GHz is 1.4 dB and 2.1 dB in simulation and measurement, respectively. Available bandwidth below -12.5 dB is from 1.66 GHz to 6.7 GHz.

Wideband beamforming network is implemented in a 3D structure as shown in Fig. 2.28. The reason is that longer length of total structure make it too heavy to support in chamber for measurement.

The beamforming network is fixed through a metal jig and the signal lines between the power divider and the TTD are connected through 90 degree SMA adapters.

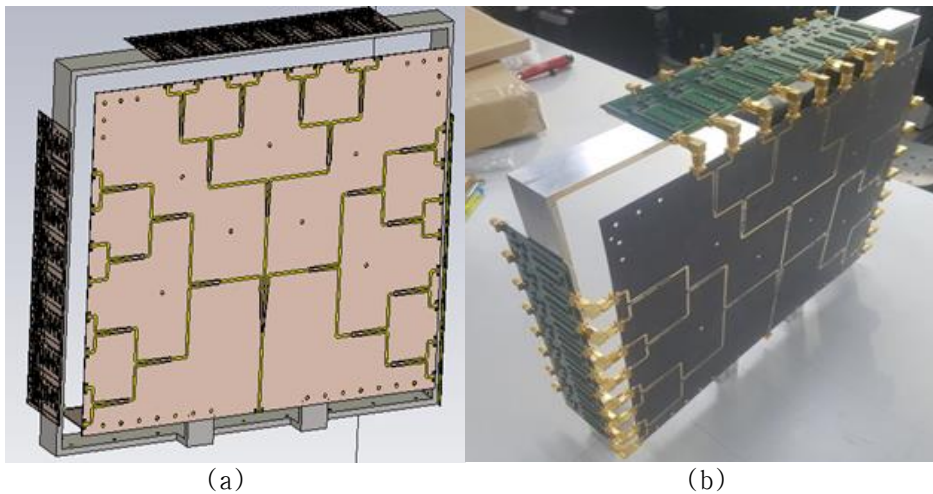


Fig. 2.28. Wideband beamforming network (a) CST simulation model and (b) fabricated model (425 x 359 x 110 mm³).

To store the DC bias voltage from the digital control circuit, a flip-flop chip was added to construct the network as shown in the Fig. 2.29. 30 pins are implemented to control: eight selection bits for clocking and 19 control bits (14 : TTD, 5 : digital attenuator), 1 VDD, 1 VSS, and 1 GND.

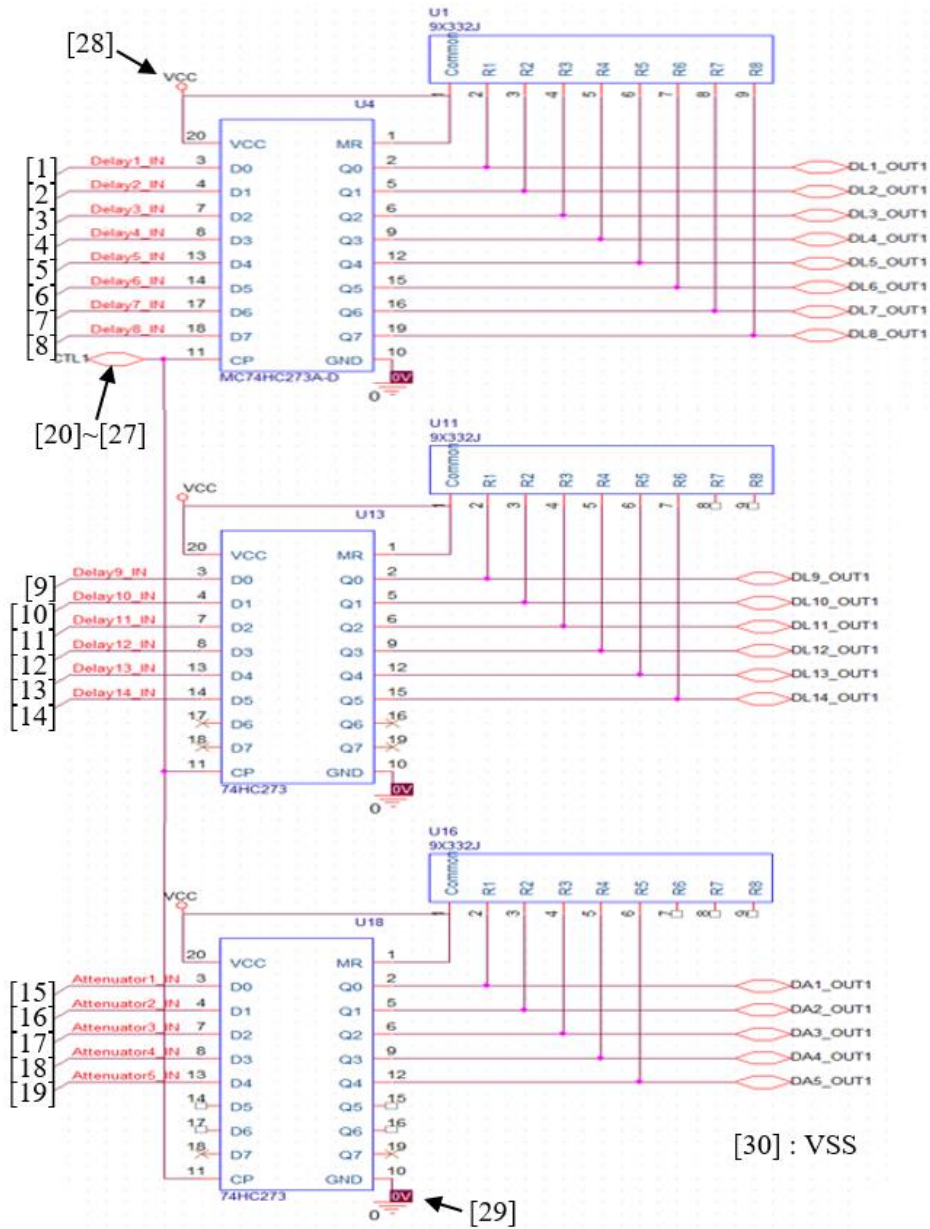


Fig. 2.29. Block diagram of digital circuit with flip-flop and information of 30 pins.

RF shielding does not need to be considered when measuring the S parameter of the beamforming network using the vector network analyzer, but RF shielding is essential when measuring the pattern

using the entire network in a chamber. This is because accurate pattern measurement results without RF shielding are difficult to obtain due to diffraction at the edges and scattering of elements such as GND substrates, TTD, and power divider. In this measurement, the entire network structure is covered with an RF shielding case to ensure accurate measurements. Except for one input port, 24 output ports, and RF penetration pipe for power supply and communication port, all of them were blocked with conductors to prevent leakage or inflow of signals as shown in Fig 2.30. The inner surface of the absorber contains 0.5T thick magnetic material powder to remove the influence of internal radiation, and the outer surface is blocked with a few cm absorber to reduce the measurement error due to scattering, enabling accurate measurement.

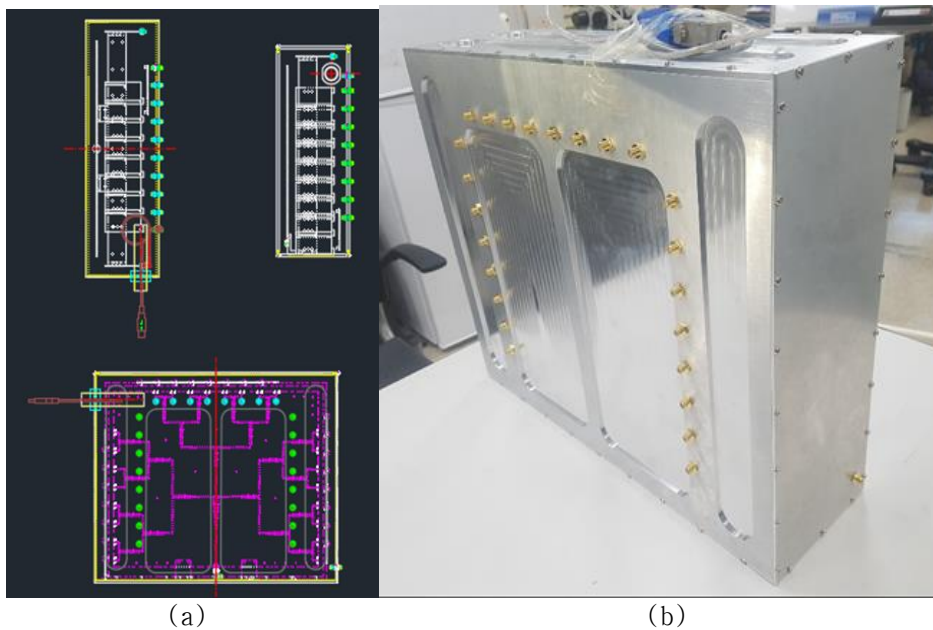


Fig. 2.30. RF shielding case (a) 2D model and (b) fabricated model.

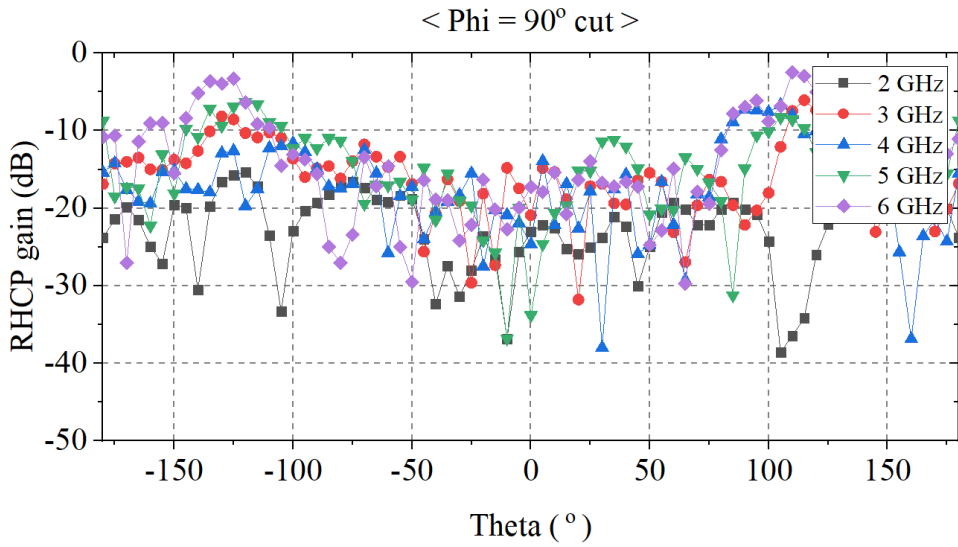


Fig. 2.31. Radiation pattern measurement results without RF shielding case when terminated at 50 Ohm with 24-way power divider and 24 TTDs without antenna.

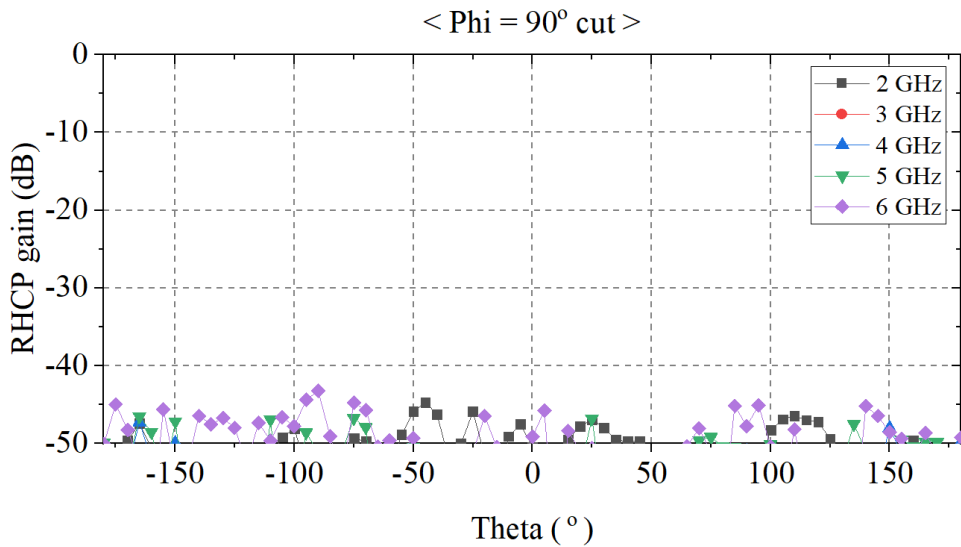


Fig. 2.32. Radiation pattern measurement results with RF shielding case when terminated at 50 Ohm with 24-way power divider and 24 TTDs without antenna.

Fig. 2.31 and Fig. 2.32 show the results of radiation pattern measurement results with or without RF shielding case when terminated at 50 Ohm with 24-way power divider and 24 TTDs without antenna. Fig. 2.32 shows that the RF shielding case works effectively.

Fig. 2.33 and Fig. 2.34 show radiation pattern measurements with and without RF shielding case, including 24 antennas. Fig. 2.33 shows that the beam synthesis does not work properly without the RF shielding case, and Fig. 2.34 shows that the beam is properly synthesized at 10° which is reference broadside angle of array over the entire band with the RF shielding case.

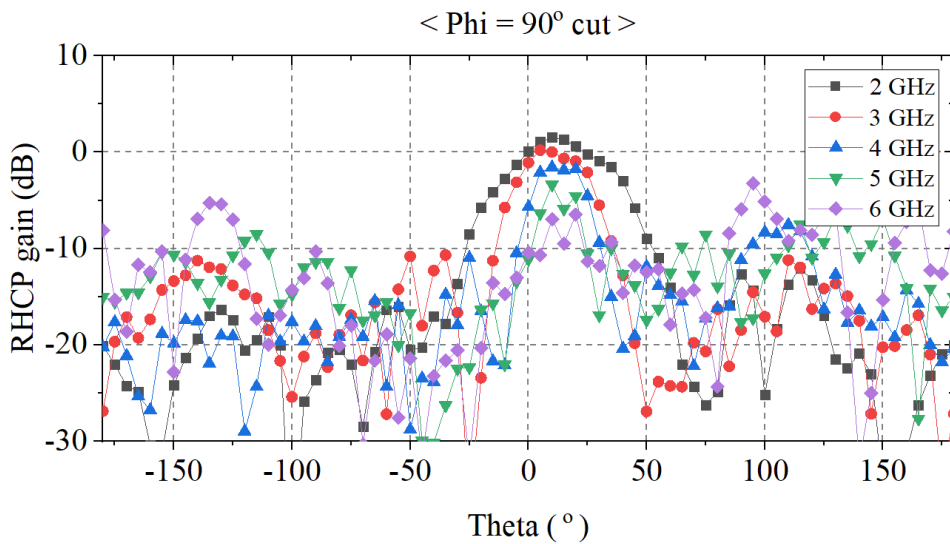


Fig. 2.33. Radiation pattern measurement results without RF shielding case when total beamforming network is connected with antennas.

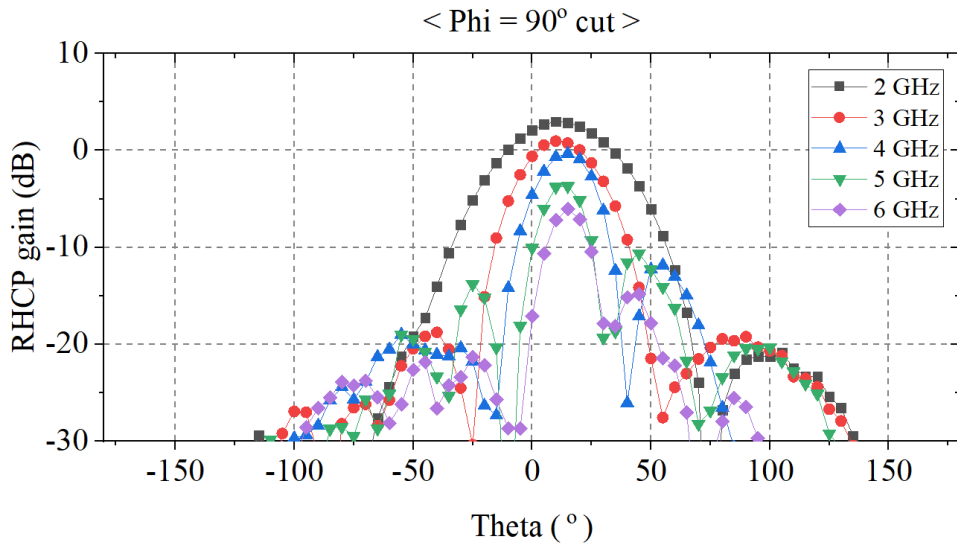


Fig. 2.34. Radiation pattern measurement results with RF shielding

24 elements of spiral antenna are arranged in a 2D conformal shape. The conformal shape was used as a reflector. The array antenna have good matching characteristics but poor AR characteristics. The solution to this problem was addressed in Chapter 3. Fig. 2.35 shows the beamforming network combined with the spiral array antenna.

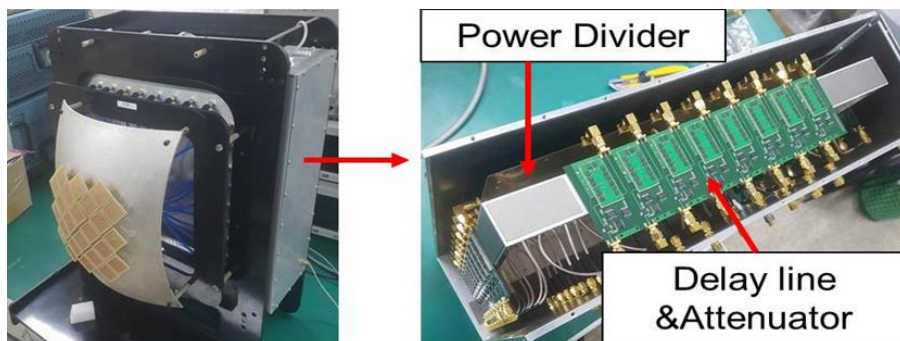


Fig. 2.35. Wideband conformal phased array antenna system with wideband beamforming network.

Beam steering was performed to verify that the whole system operates properly. Fig. 2.36 shows the $\phi=0^\circ$ cut results of beam steering from -30° to 40° in azimuth angle at 6 GHz, the worst case of side lobe level. Fig. 2.37 shows the $\phi=90^\circ$ cut results of beam steering from 10° to 30° in elevation angle at 6 GHz. As shown in Fig. 2.36 and Fig. 2.37, the beam steering is performed properly, with the side lobe level below -10 dB in both 2D directions.

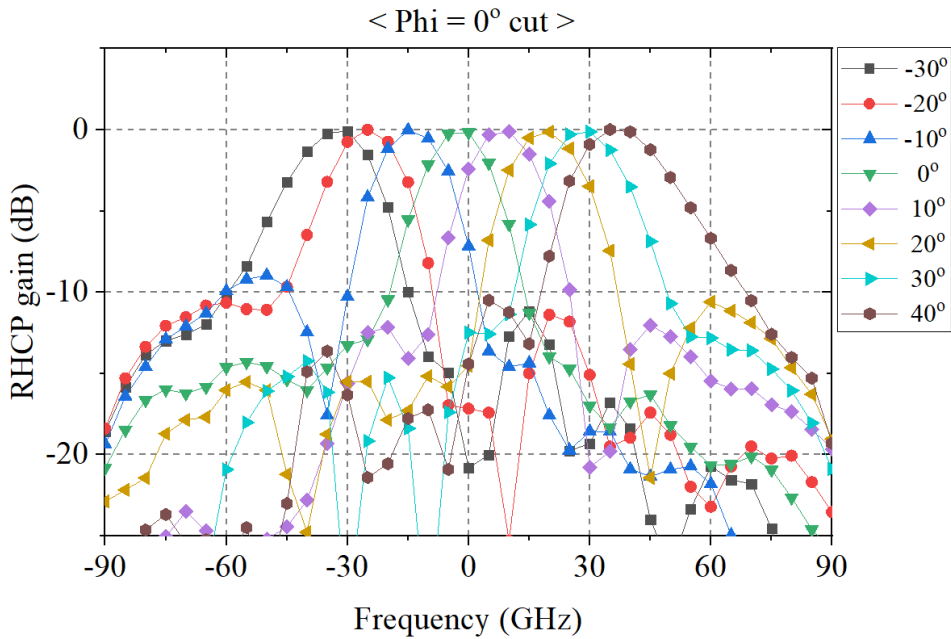


Fig. 2.36. $\phi=0^\circ$ cut normalized results of beam steering from -30° to 40° in azimuth angle at 6 GHz.

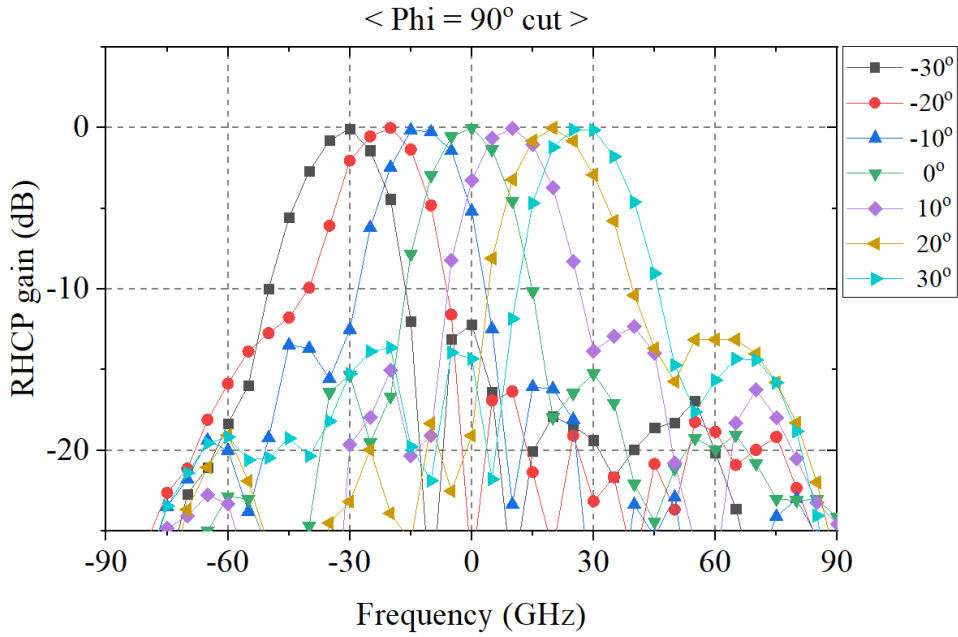


Fig. 2.37. $\phi = 90^\circ$ cut normalized results of beam steering from -30° to 30° in elevation angle at 6 GHz.

Beam steering was performed in the whole band to verify the TTD. Fig. 2.38, Fig. 2.39, Fig. 2.40, and Fig. 2.41 show $\phi = 0^\circ$ cut results of beam steering from 0° to 30° in azimuth angle at 2, 3, 4, 5, 6 GHz. As expected, as the frequency increased, the beam width decreased and beam steering was achieved with exactly the desired beam steering angle, which means beam steering is performed without beam squint within the 3 : 1 bandwidth. Based on the above results, it was verified that the miniaturized TTD is capable of wideband beam steering.

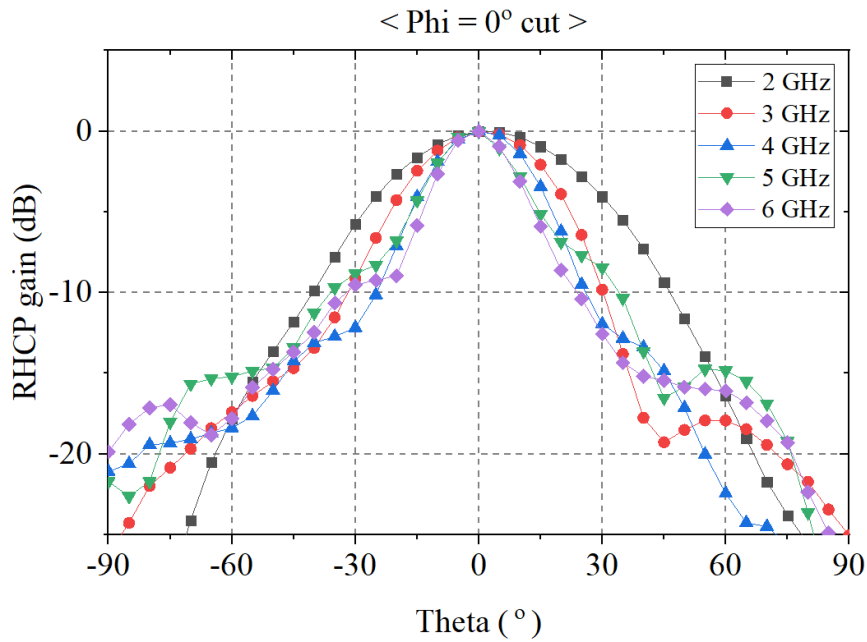


Fig. 2.38. $\phi = 0^\circ$ cut normalized results of 0° beam steering in azimuth angle at 2, 3, 4, 5, 6 GHz.

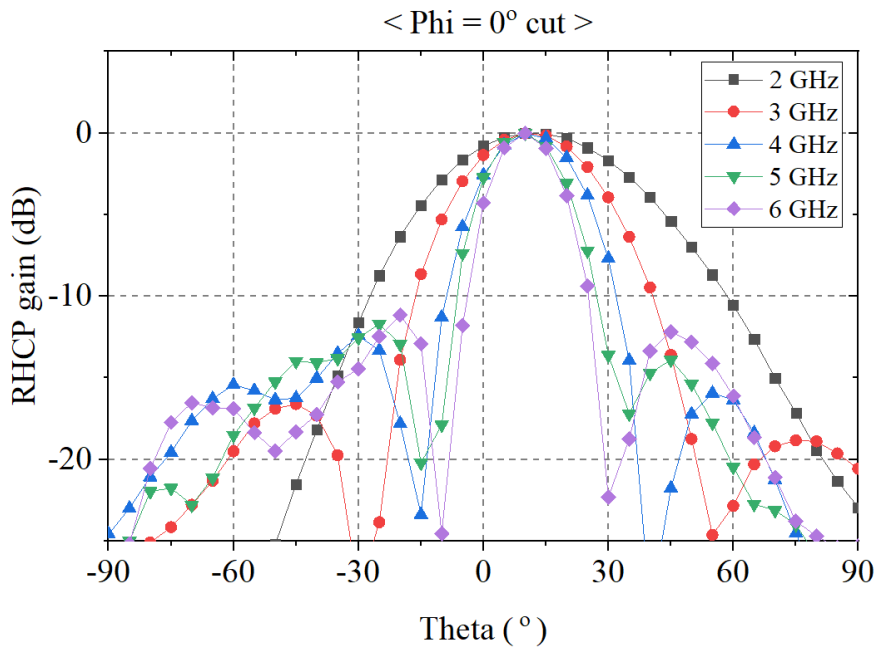


Fig. 2.39. $\phi = 0^\circ$ cut normalized results of 10° beam steering in azimuth angle at 2, 3, 4, 5, 6 GHz.

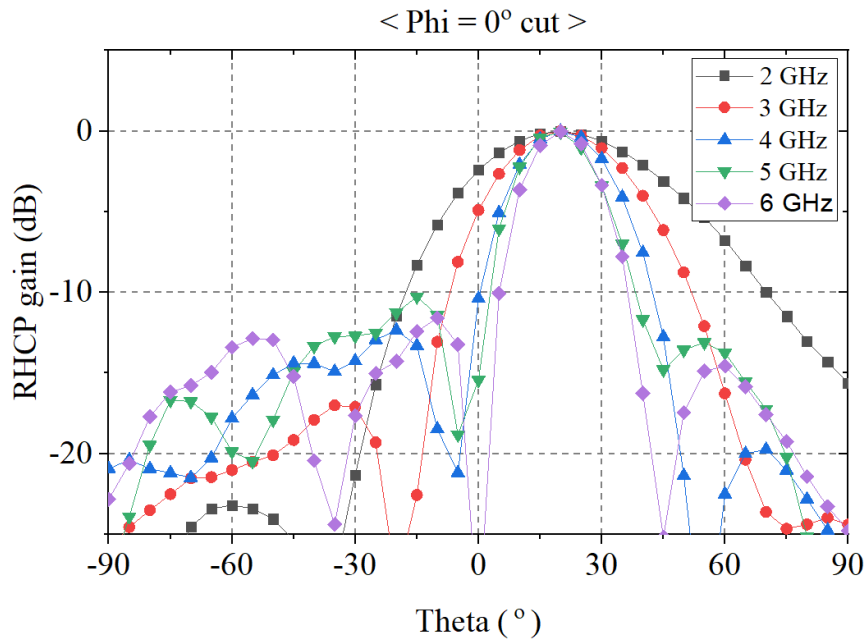


Fig. 2.40. $\phi = 0^\circ$ cut normalized results of 20° beam steering in azimuth angle at 2, 3, 4, 5, 6 GHz..

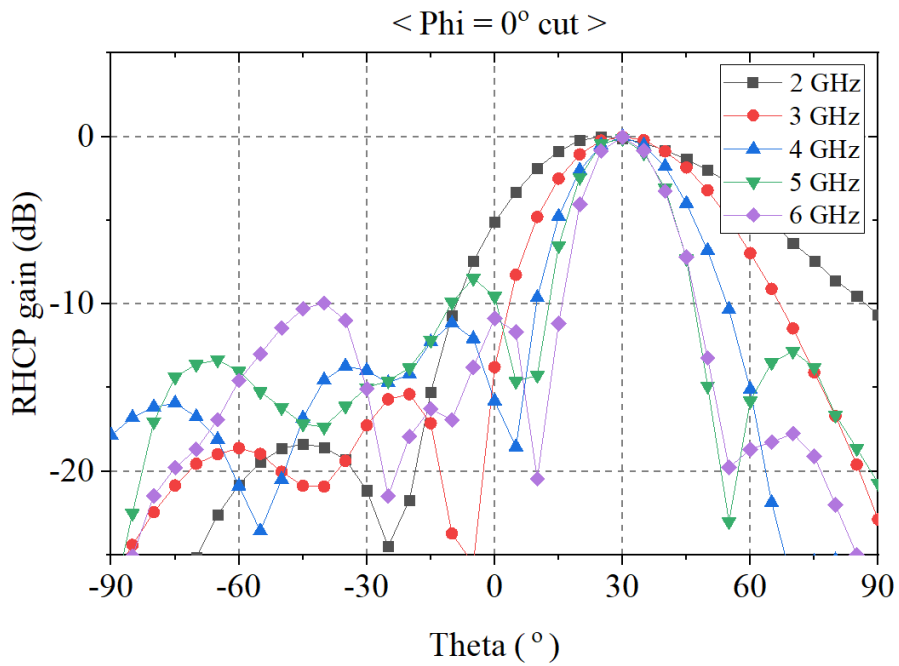


Fig. 2.41. $\phi = 0^\circ$ cut normalized results of 30° beam steering in azimuth angle at 2, 3, 4, 5, 6 GHz..

2.3 Conclusion

In this chapter, design considerations and procedure of wideband beamforming network is presented. Three factors that can affect group delay variation are analyzed, which is the most important performance indicator of the TTD. First factor that affects group delay characteristic is off-state capacitor resonance. To minimize degradation of TTD performance due to the resonances, switches with an off-state isolation of more than 30 dB are required. Second factor is reflected wave due to discontinuity, so that matching must be accomplished in design of TTDs and all system. The last factor is the phase error caused by the reflection coefficient due to the antenna impedance. Monte Carlo simulations were performed to investigate the effect of phase delay error on the beam steering angle and side lobe level due to antenna impedance. And the actual antenna is designed to verify the effect of the phase delay error on the antenna impedance. Considering these factors we designed 7-bit multistacked TTD for miniaturization which is an additional issue when designing a TTD. Fabrication and measurement were performed and our approach shows an improved performance regarding a figure of merit defined as the relative delay divided by the insertion loss at the longest delay state, a large number of bits of resolution, and low power consumption. Finally, a wideband antenna system was constructed to verify the fabricated TTD. Beam steering is performed without beam squint within the 3 : 1 bandwidth, which

verify that the miniaturized TTD is capable of wideband beam steering.

Chapter 3. Low-profile wideband antenna

In general, low-profile antennas are antennas with a ground plane in close proximity. Design of low-profile wideband antennas is a challenging issue due to the ground plane in close proximity. Hence, an essential technology for low-profile wideband phased array antenna systems is to solve performance degradation problems when forming a unidirectional beam by attaching a PEC reflector close to the wideband antenna. Antennas with unidirectional pattern such as microstrip patch antennas can be operated in a wide band by applying various broadband techniques. However, the bandwidth is relatively smaller than that of other broadband antennas. Wideband antennas such as helical antenna and tapered slot antenna are difficult to be considered low-profile antennas due to their high height and large area. The most applicable type of antennas for low profile wideband antenna array is spiral antenna which has advantages of simple manufacture process and miniaturization for array. Spiral antenna has the disadvantage of requiring a reflector for unidirectional patterns due to its bi-directional circular polarized pattern. Reflections by reflector can lead to performance degradation of matching and AR characteristics. Although several papers have been published, which solve the matching problem using AMC structures such as PBG and EBG for the design of lower height spiral antenna, the papers do not provide AR results [8–11]. In other words, these papers succeeded in transmitting all power in one direction by improving matching, but

have different polarization over frequency, which is not suitable for intentional utilization. Many papers have been proposed the insertion of absorbers or resistors to mitigate AR deterioration [12], [13]. The simple principle is to convert the reflected wave by the reflector into a loss through the absorber or resistor so that it only has a pattern by the upwardly radiated wave. Improvement of AR is achieved at the cost of radiation efficiency. [28] has presented improvement of AR through EBG plane without absorbers, but it was a single spiral antenna which is a very large antenna compared to the wavelength, so it is not suitable for array antennas. The AR deterioration was not analyzed and the empirical simulation was only performed by gradually removing the patch elements of the EBG structure in [28]. In this paper, we analyzed the reason why the AR could be deteriorated by the reflector. Based on this, we designed a spiral array antenna with excellent AR and matching characteristics without loss by applying polarization-dependent phase tunable reflector.

3.1. Analysis of AR deterioration with reflector

A reflector is used to convert the bidirectional pattern of antenna into the unidirectional pattern. The equations in [29] are described assuming that scattering does not occur at the plane of antennas in Fig. 3.1, which means that $T^A=1$ and $\Gamma^A=0$.

$$\vec{E}_{total} = \vec{E}_1 + \vec{E}_2 = \vec{E}_1 + \phi \Gamma^R \vec{E}_1 \quad (3.1)$$

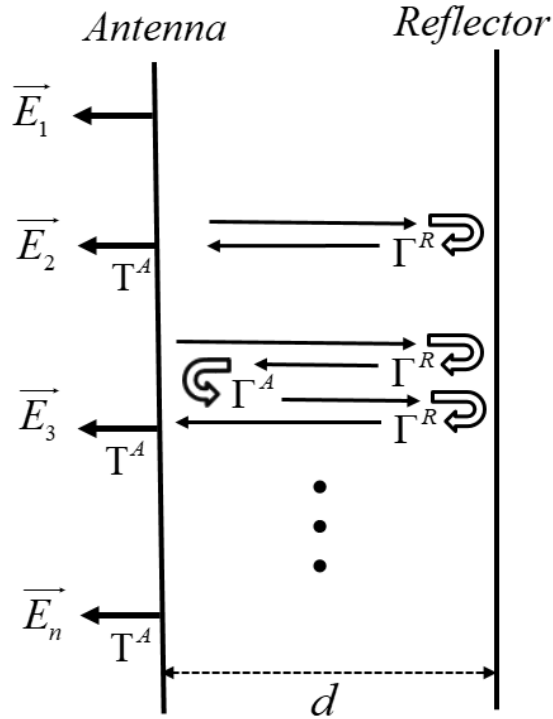


Fig. 3.1. Multiple reflection between antenna and reflector.

The total E-field in this case is obtained as shown in (3.1). AR deterioration is not appeared with this equation because there is no polarization-dependent change. However, as shown in Fig. 3.1, the

reflected wave generated by the reflector is reflected back from the antenna with transmitted wave, causing multiple reflections, which causes AR deterioration. When passing through the conductors of antennas, the transmitted wave and the reflected wave are generated unconditionally because it cannot be transmitted without reflection. The AR deteriorates because the reflected reflection coefficient and the transmission coefficient are not symmetric about polarization.

For the reason of AR deterioration, it can be inferred that structurally the 4–arm spiral antenna has no deterioration of the AR due to the reflector because the reflection coefficient and the transmission coefficient are symmetric about polarization unlike the 2–arm spiral antenna. However, the 4–arm spiral antenna is not considered in this paper because it has the disadvantage of requiring additional bulky network to apply the phase difference of 90 degrees. In addition, the 4–arm spiral antenna is disadvantageous compared to 2–arm in terms of bandwidth because the cycle of conductors that can be wound in the same area is less than that of 2–arm.

Considering all the reflections and transmissions shown in Fig. 3.1, the equation is arranged as follows.

$$\begin{aligned}\overrightarrow{E}_{total} &= \overrightarrow{E}_1 + \overrightarrow{E}_2 + \overrightarrow{E}_3 + \dots + \overrightarrow{E}_\infty \\ &= \overrightarrow{E}_1 + \phi\Gamma^A\Gamma^R\overrightarrow{E}_1 + \phi\Gamma^A(\phi\Gamma^R\Gamma^A)\Gamma^R\overrightarrow{E}_1 + \phi\Gamma^A(\phi\Gamma^R\Gamma^A)^2\Gamma^R\overrightarrow{E}_1 + \dots\end{aligned}\quad (3.2)$$

The terms in (3.2) can be described to a matrix and (3.2) is summarized as follows.

$$\vec{E}_{total} = \left[\mathbf{I} + e^{-j\frac{4\pi d}{\lambda}} \begin{pmatrix} \mathbf{T}_{xx}^A & \mathbf{T}_{xy}^A \\ \mathbf{T}_{yx}^A & \mathbf{T}_{yy}^A \end{pmatrix} \right] \left\{ \mathbf{I} - e^{-j\frac{4\pi d}{\lambda}} \begin{pmatrix} \mathbf{\Gamma}_{xx}^R & \mathbf{\Gamma}_{xy}^R \\ \mathbf{\Gamma}_{yx}^R & \mathbf{\Gamma}_{yy}^R \end{pmatrix} \begin{pmatrix} \mathbf{\Gamma}_{xx}^A & \mathbf{\Gamma}_{xy}^A \\ \mathbf{\Gamma}_{yx}^A & \mathbf{\Gamma}_{yy}^A \end{pmatrix} \right\}^{-1} \begin{pmatrix} \mathbf{\Gamma}_{xx}^R & \mathbf{\Gamma}_{xy}^R \\ \mathbf{\Gamma}_{yx}^R & \mathbf{\Gamma}_{yy}^R \end{pmatrix} \begin{pmatrix} E_x \\ E_y \end{pmatrix} e^{-jk_0 z} \quad (3.3)$$

The AR can be obtained as shown in (3.4) by the magnitude and phase of the total E–field for each polarization in (3.3).

$$AR = \frac{\sqrt{\frac{1}{2} \left(|E_{x,total}|^2 + |E_{y,total}|^2 + \sqrt{|E_{x,total}|^4 + |E_{y,total}|^4 + 2|E_{x,total}|^2 |E_{y,total}|^2 \cos(2(\angle E_{y,total} - \angle E_{x,total}))} \right)}}{\sqrt{\frac{1}{2} \left(|E_{x,total}|^2 + |E_{y,total}|^2 - \sqrt{|E_{x,total}|^4 + |E_{y,total}|^4 + 2|E_{x,total}|^2 |E_{y,total}|^2 \cos(2(\angle E_{y,total} - \angle E_{x,total}))} \right)}} \quad (3.4)$$

Equation (3.3) and (3.4) shows the factors influencing the AR are the magnitude and phase of the e–field for each polarization, the reflection and transmission coefficients of the antenna conductor according to each polarization, the distance between the antenna and the reflector, and the reflection coefficient at the reflector.

To verify that equation (3.3) and (3.4) are valid, spiral antennas are designed as shown in Fig. 3.2 and Fig. 3.3. A 2–arm equiangular spiral antenna with rectangular ring was designed using a 32 mil (0.8128 mm) thick RF–45 substrate and a FR4 substrate dielectric loading [30]. Design parameters are shown in Table 3.1. A tapered arm structure is used to miniaturize antenna size [31]. The mutual coupling between the outer rectangular ring and the antenna reduces

the reflection and improves the matching characteristics at low frequencies [32].

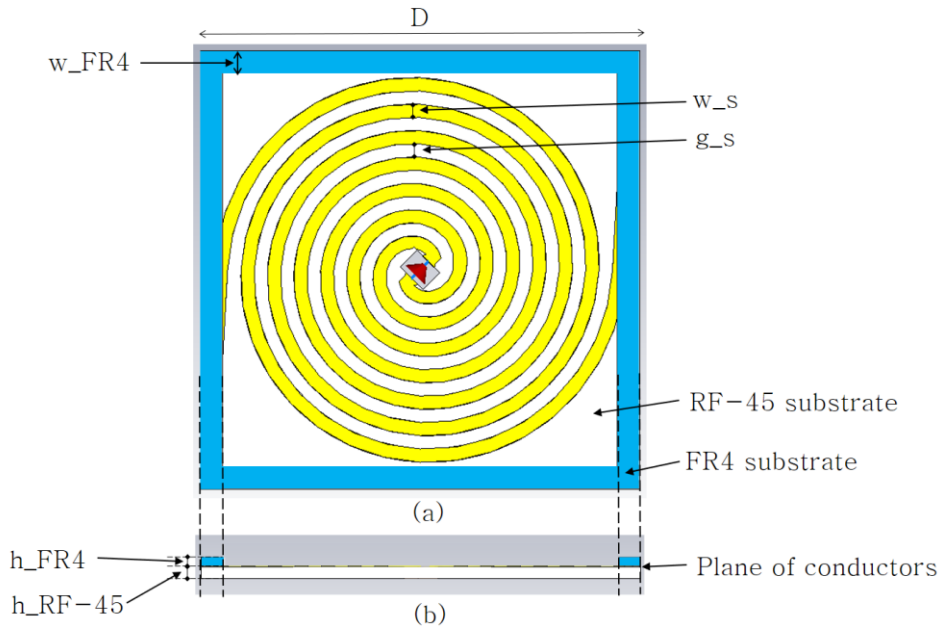


Fig. 3.2. Designed 2-arm spiral antenna (a) top view, (b) side cut view.

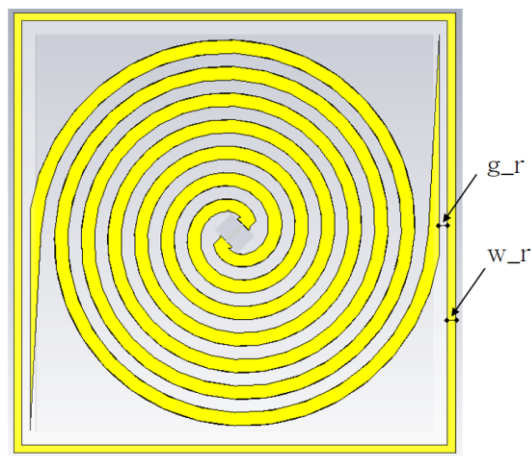


Fig. 3.3. Conductor pattern of 2-arm spiral antenna.

Table 3.1. Dimensions of the designed 2–arm spiral antenna.

Parameter	Value	Parameter	Value
D	30 mm	w_s	0.9 mm
w_FR4	1.5 mm	g_s	0.9 mm
h_FR4	0.6 mm	w_r	0.55 mm
h_RF-45	0.8128 mm	g_r	0.55 mm

When the plane wave is incident from the $-z$ axis to the designed antenna, the reflection and transmission coefficients for each polarization are extracted for calculation of AR with equation (3.3) and (3.4). In addition, the magnitude and phase of E–field of spiral antenna without reflector for each polarization at broadside are extracted for calculation. Fig. 3.4 shows AR comparison the calculation with the simulation results of designed spiral antenna with PEC plane at broadside. Distance between antenna and PEC plane (d) is 23 mm in simulation model. Periodic boundary simulation for infinite array was performed through CST time domain solver. The reflection coefficients for each polarization are -1 in calculation process. Fig. 3.4 shows that AR of antenna with PEC at broadside is worse than AR of antenna without PEC. The simulation results and the calculated values of the AR of antenna with PEC are almost identical, which means that above equations are valid and AR deterioration is analyzed.

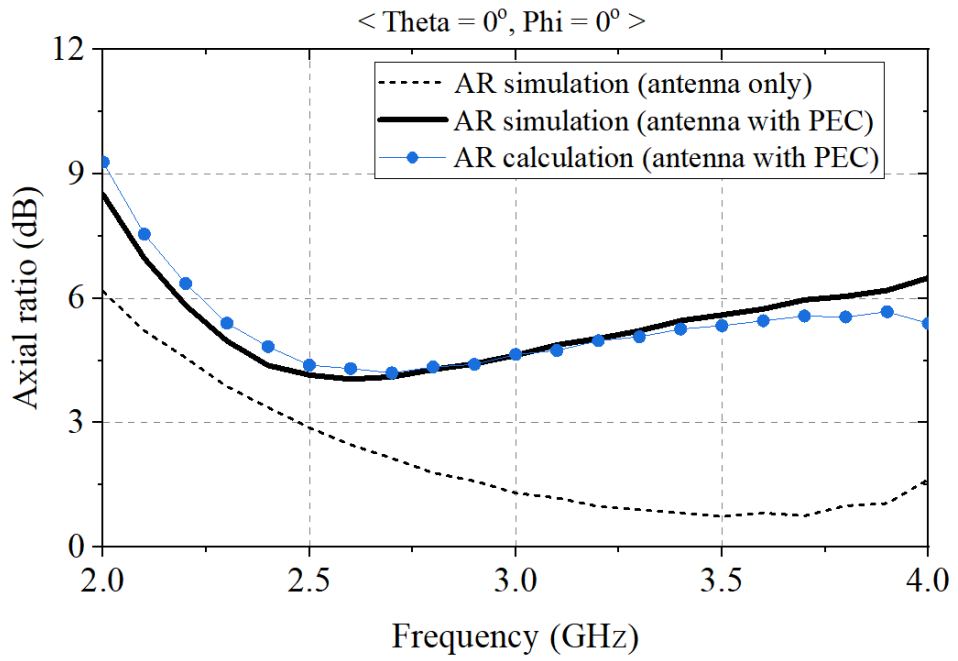


Fig. 3.4. Comparison of the AR of designed spiral antenna backed by PEC plane at broadside.

3.2. Improvement of AR with polarization-dependent phase tunable reflector

3.2.1 AR improvement through reflector with ideal reflection phase

Once the antenna is set and the distance between antenna and the reflector is determined, the factor that can change for improvement of the AR is the reflection phase of reflector. If the reflection phase for each polarization of the reflector changes simultaneously, the AR values are not changed significantly.

We observed how the AR was improved by changing the reflection phase of each polarization ($\angle\Gamma_{xx}^R$ and $\angle\Gamma_{yy}^R$) individually. Fig. 3.5 shows the optimum AR results at broadside obtained by changing $\angle\Gamma_{xx}^R$ and $\angle\Gamma_{yy}^R$ individually with 2D phase tunable reflector. The optimum AR is improved significantly compared to AR of antenna with PEC reflector. Through the above equation and calculation results, ideal circular polarization characteristics near 0 dB in entire band theoretically can be achieved by changing the reflection phase of each polarization separately. Fig. 3.6 shows $\angle\Gamma_{xx}^R$ and $\angle\Gamma_{yy}^R$ required for optimum AR in Fig. 3.5.

Next, we observed how the AR was improved by changing the reflection phase of one polarization ($\angle\Gamma_{xx}^R$) while fixing the reflection phase of the other polarization ($\angle\Gamma_{yy}^R$). In the process, it is assumed that $\angle\Gamma_{xy}^R$ and $\angle\Gamma_{yx}^R$ have very small values ($\angle\Gamma_{xy}^R = \angle\Gamma_{yx}^R = 0$). Fig.

3.7 shows the optimum AR results 1D phase tunable reflector at broadside obtained by changing $\angle\Gamma_{xx}^R$ with $\angle\Gamma_{yy}^R$ fixed at -180° . The optimum AR is improved compared to AR of antenna with PEC reflector. Fig. 3.8 shows $\angle\Gamma_{xx}^R$ and $\angle\Gamma_{yy}^R$ required for optimum AR in Fig. 3.7. Similarly, the optimum AR at broadside can be obtained with the $\angle\Gamma_{xx}^R$ fixed at -180° , as shown in Fig. 3.9. Fig. 3.10 shows $\angle\Gamma_{xx}^R$ and $\angle\Gamma_{yy}^R$ required for optimum AR at broadside. The optimum AR by changing $\angle\Gamma_{xx}^R$ is also improved compared to axial ratio of antenna with PEC reflector.

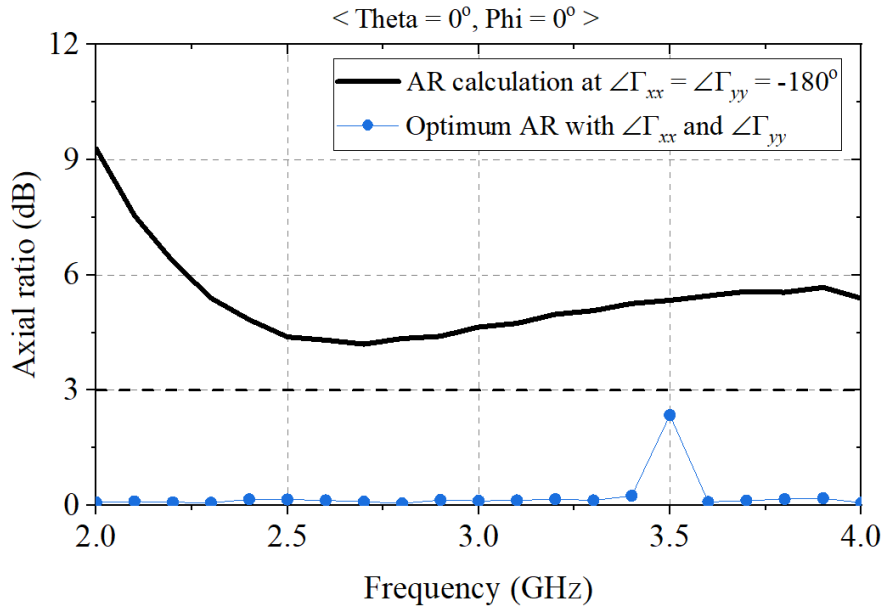


Fig. 3.5. Optimum AR results at broadside obtained by changing $\angle \Gamma_{xx}^R$ and $\angle \Gamma_{yy}^R$ individually (2D) compared to AR with PEC reflector.

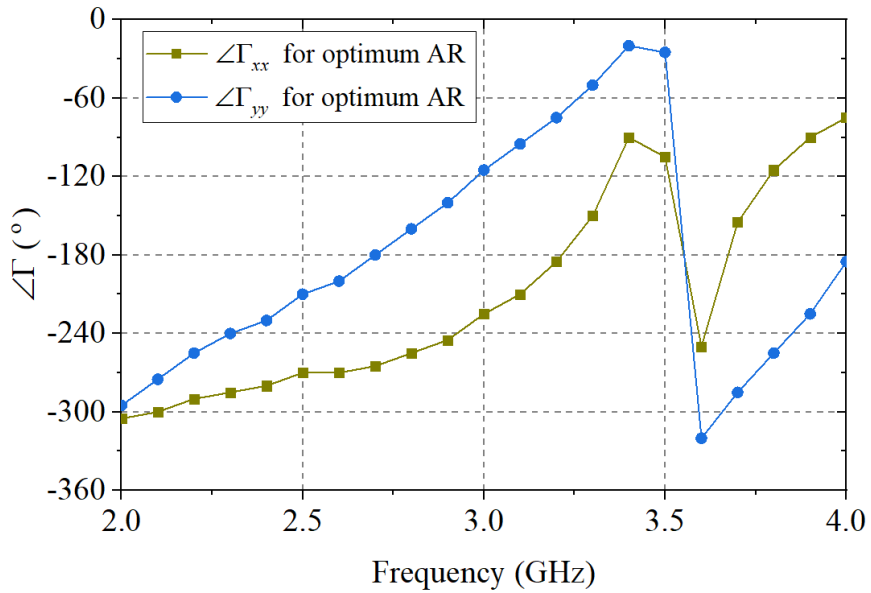


Fig. 3.6. Required $\angle \Gamma_{xx}^R$ and $\angle \Gamma_{yy}^R$ for optimum AR in Fig. 3.5 (2D).

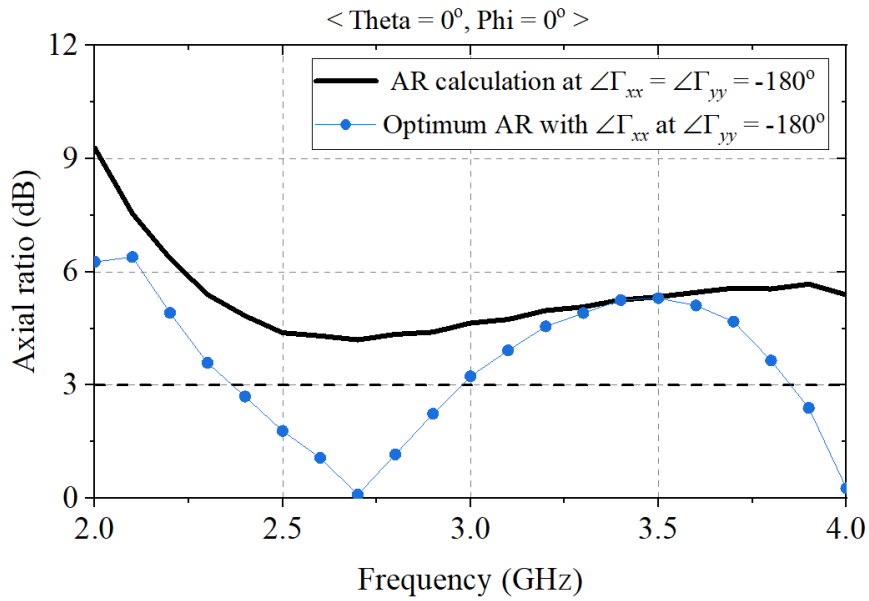


Fig. 3.7. Optimum AR results at broadside obtained by changing $\angle \Gamma_{xx}^R$ of (1D) with $\angle \Gamma_{yy}^R$ fixed at -180° compared to AR with PEC reflector.

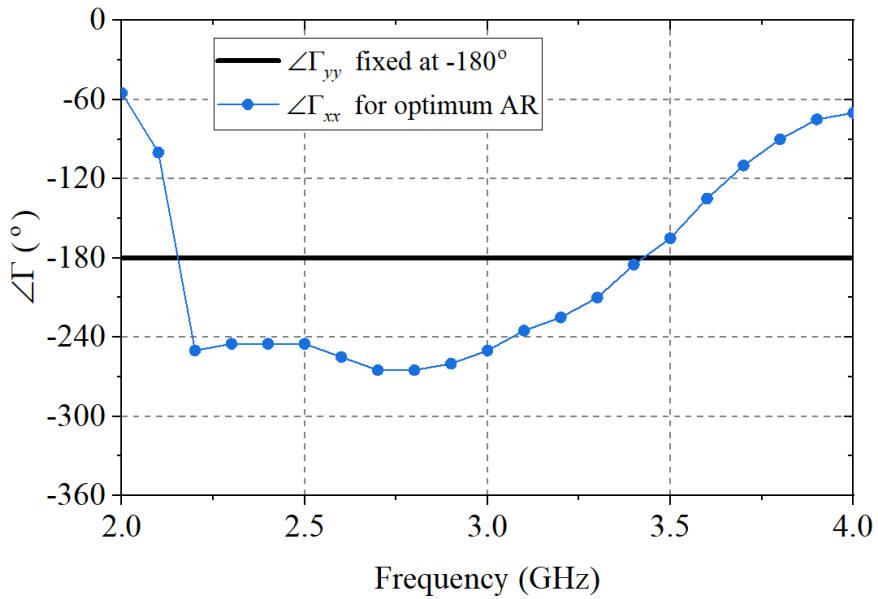


Fig. 3.8. Required $\angle \Gamma_{xx}^R$ and $\angle \Gamma_{yy}^R$ for optimum AR in Fig. 3.7 (1D).

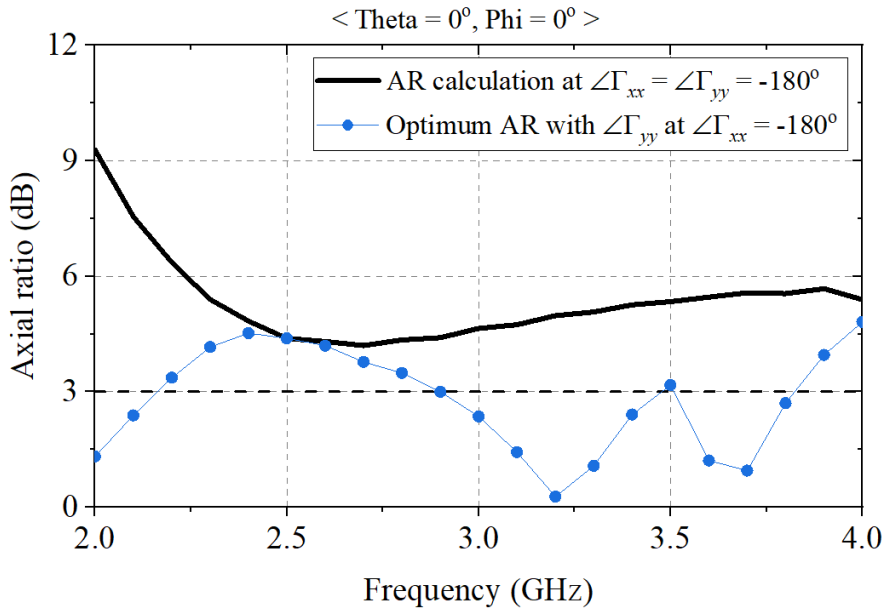


Fig. 3.9. Optimum AR results at broadside obtained by changing $\angle\Gamma_{yy}^R$ of (1D) with $\angle\Gamma_{xx}^R$ fixed at -180° compared to AR with PEC reflector.

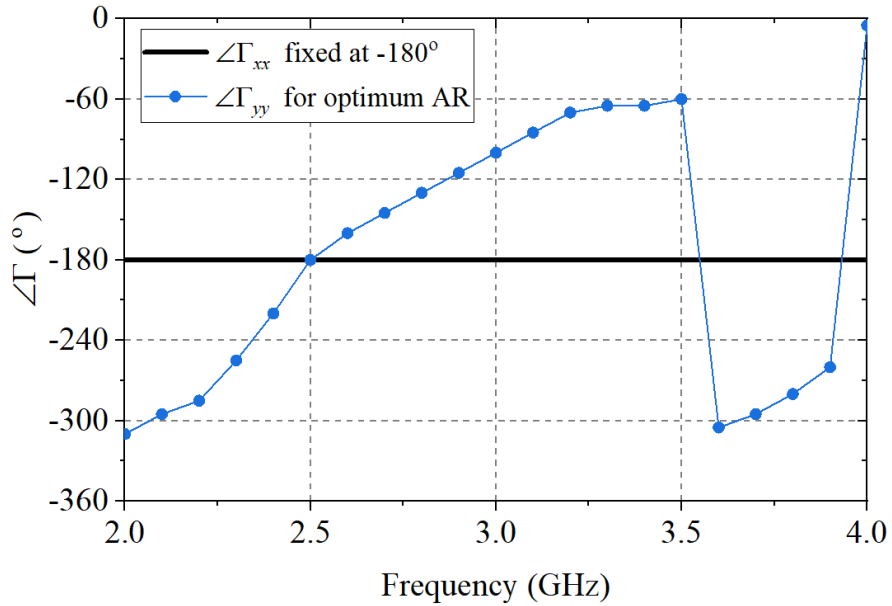


Fig. 3.10. Required $\angle\Gamma_{xx}^R$ and $\angle\Gamma_{yy}^R$ for optimum AR in Fig. 3.9 (1D).

3.2.2 Practical design issues of reflector with varactor

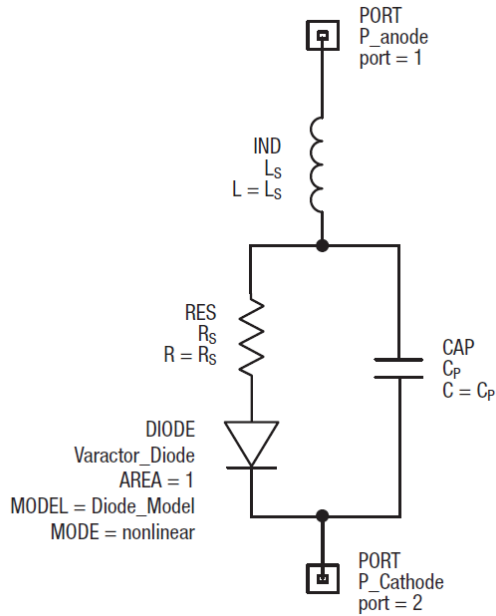


Fig. 3.11. Equivalent circuit of varactor.

Table 3.2. Parameter values of varactor.

Parameter	Value	Parameter	Value
L_S	0.45 nH	$R_S @ 4V,$ 50MHz	0.8 Ohm
C_P	0.29 pF	Q @ 4V, 50MHz	3200

A polarization-dependent phase tunable reflector is proposed to implement the required $\angle\Gamma_{xx}^R$ and $\angle\Gamma_{yy}^R$. It can be implemented using varactors. The commercial varactor used in the overall simulation is SMV1405 (Skyworks Solutions, Inc., Woburn, Massachusetts, USA) and the equivalent circuit is shown in Fig. 3.11. Parameter values of

varactor are shown in Table 3.2.

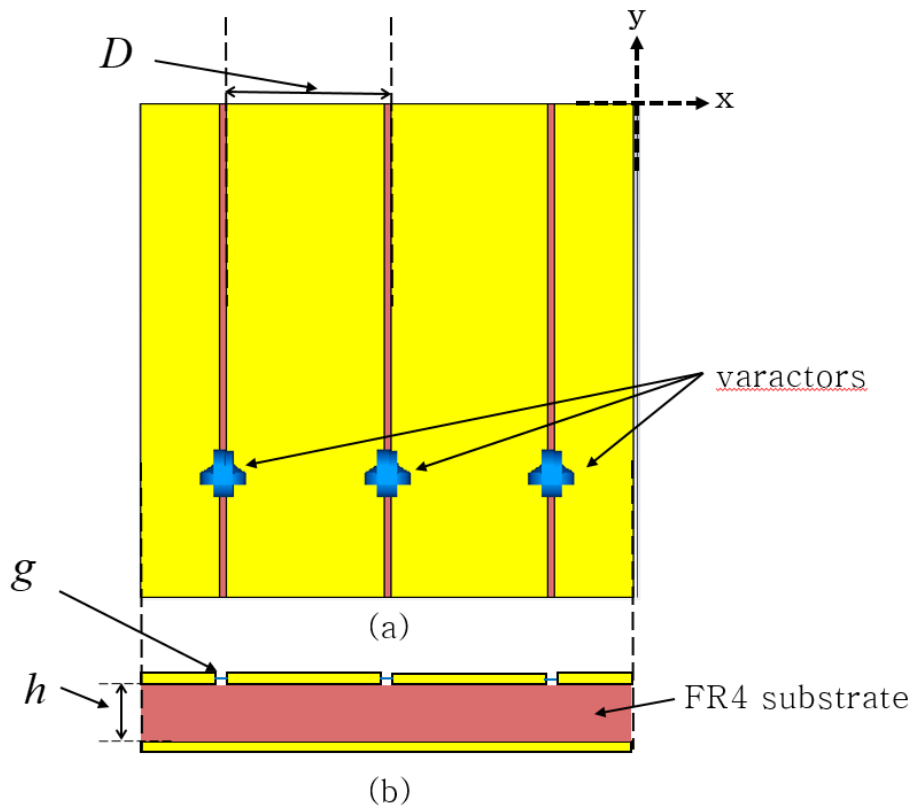


Fig. 3.12. Proposed design model of polarization-dependent 1D phase tunable reflector with varactors (a) top view, (b) side cut view.

A varactor with a high Q value was chosen to reduce the loss near the resonance point. As shown in Fig. 3.12, parallel resonance occurs when the conductors are arranged periodically with a gap and supported by a low height GND plane. The GND plane close to the plane of incidence can be equivalent to inductor and the gap between conductors can be equivalent to capacitor. Design of polarization-dependent phase tunable reflector with varactors in Fig. 3.12 can

make parallel resonance, which means the desired reflection phase can be adjusted by changing reverse bias voltage of varactors. The resonance frequency occurred by the parallel resonance is as follows [33].

$$f_0 = \frac{1}{2\pi\sqrt{L(C_g + C_{\text{var}})}} \quad (3.5)$$

where

$$L = \mu_0 h, \quad C_g = \frac{D\epsilon_0(\epsilon_r + 1)}{\pi} \log\left(\frac{4D}{g}\right) \quad (3.6)$$

C_g is the capacitance value represented by the gap in the periodic structure, and C_{var} is the capacitance value of the varactor that can be adjusted by bias voltage. The reflection phase changes from 180° to -180° for an incident plane wave having polarization in the direction orthogonal to the gap and a reflection phase of 180° maintains for an incident wave having polarization in the direction parallel to the gap, which is polarization-dependent phase tunable characteristic. Depending on the capacitance change of the varactors (C_{var}), the frequency at which the parallel resonance occurs can be changed as shown in Fig. 3.13, which is assuming that R_S is 0 ohm

in Fig. 3.11. The reflection phase for x polarization varies from 2 GHz to 4 GHz while the reflection phase for y polarization is maintained at 180 degrees.

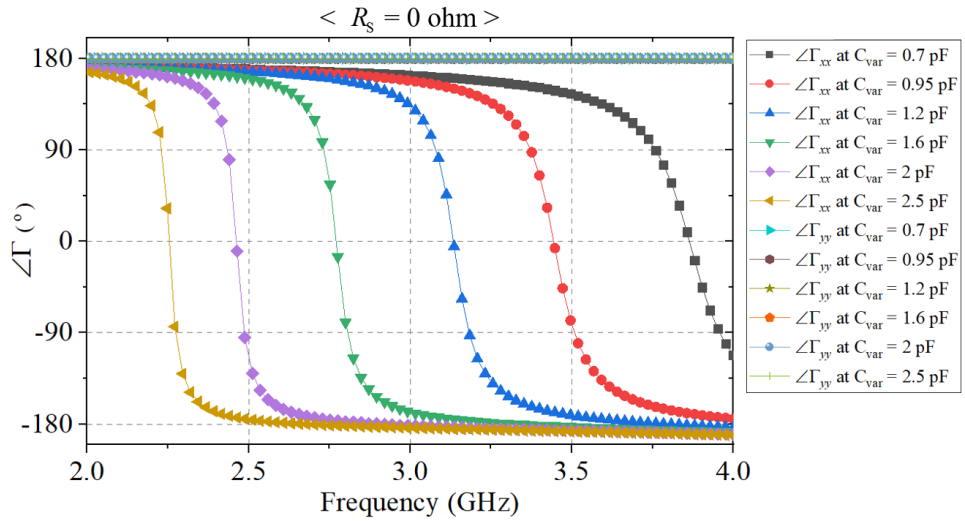


Fig. 3.13. Reflection phase of Γ_{xx}^R and Γ_{yy}^R for an incident plane wave depending on the capacitance change of the varactors when R_S is 0 ohm.

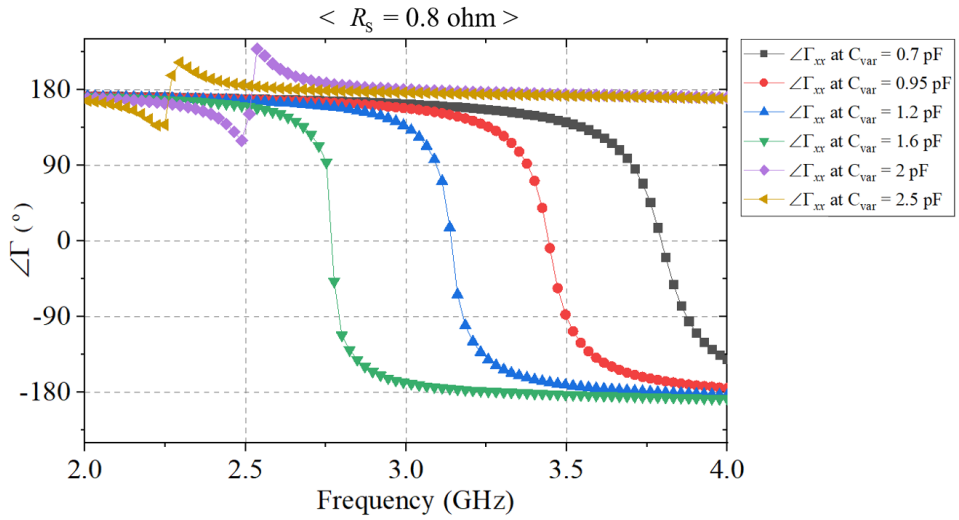


Fig. 3.14. Reflection phase of Γ_{xx}^R for an incident plane wave depending on the capacitance change of the varactors when R_S is 0.8 ohm.

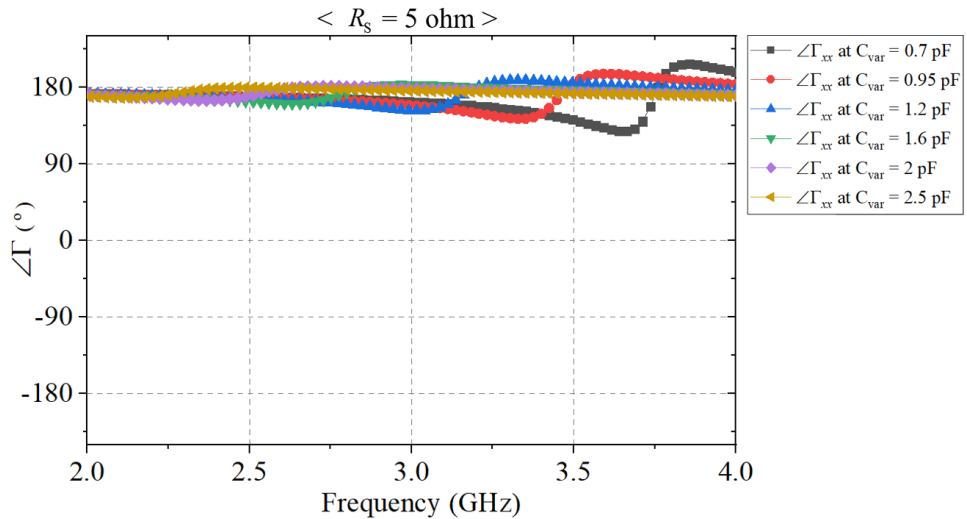


Fig. 3.15. Reflection phase of Γ_{xx}^R for an incident plane wave depending on the capacitance change of the varactors when R_S is 5 ohm.

In practice, the larger the R_s value of the varactor, the more limited the control of reflection phase as shown in Fig. 3.14 and Fig. 3.15. This limitation can be illustrated in Fig. 3.16 and Fig. 3.17. The impedance of surface (Z_s) at low frequencies drops when varactors with a low Q (large R_s) is used. As shown in (3.7), the imaginary part of Z_s affects reflection phase. The phase change due to the resonance is reduced where the absolute value of imaginary part of Z_s is small in Fig. 3.17.

$$\Gamma = \frac{\text{Re}[Z_s] - Z_0 + j \text{Im}[Z_s]}{\text{Re}[Z_s] + Z_0 + j \text{Im}[Z_s]} \quad (3.7)$$

In an ideal case ($R_s = 0$), the phase is adjusted according to the capacitance value without problems, whereas when R_s is 5 ohm, no phase change is seen in all cases. The R_s of a varactor with excellent Q is 0.8 ohm. From Fig. 3.16 and Fig. 3.17, the real and imaginary part of Z_s value according to the capacitance value at 0.8 ohm shows that operation band is over 2.55GHz. This practical issue limits the operating range of the reflector. An additional consideration is the method of extending the high frequency operating range by lowering the minimum value of C_{var} , which is also limited by the

trade-off between Q and the doping concentration of the varactor. In order to lower the minimum value of C_{var} or to increase the capacitance ratio, the doping concentration of varactor should be increased, which increases the loss, and consequently the Q of the varactor is lowered. This means that the range of the low frequency operating band is reduced, which limits the wider operating band. Finally, it is necessary to select the appropriate design parameters and the proper varactor according to equation (3.5) and (3.6) to design the reflector for the desired frequency band. Considering all the practical issues above, we designed a reflector that operates from 2.55GHz to 3.8GHz as shown in Fig. 3.12. Design parameters of proposed design of polarization-dependent phase tunable reflector of are shown in Table 3.3.

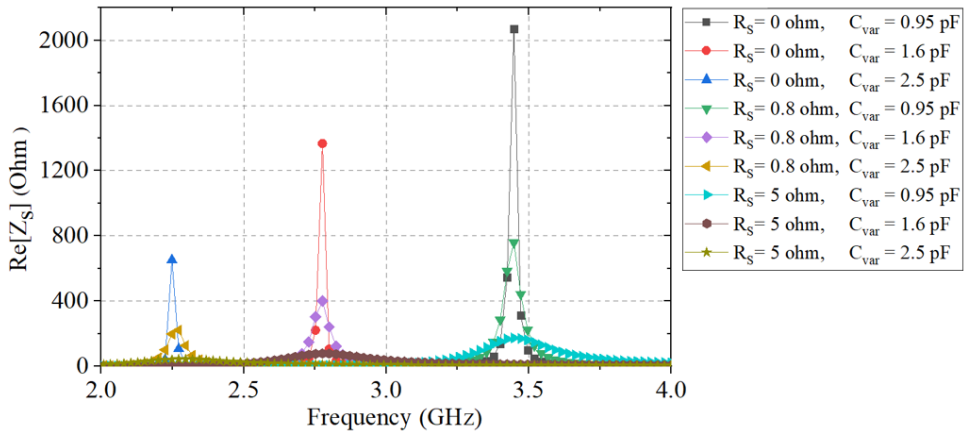


Fig. 3.16. Real part of Z_S for an incident plane wave depending on the capacitance and R_S change of the varactors.

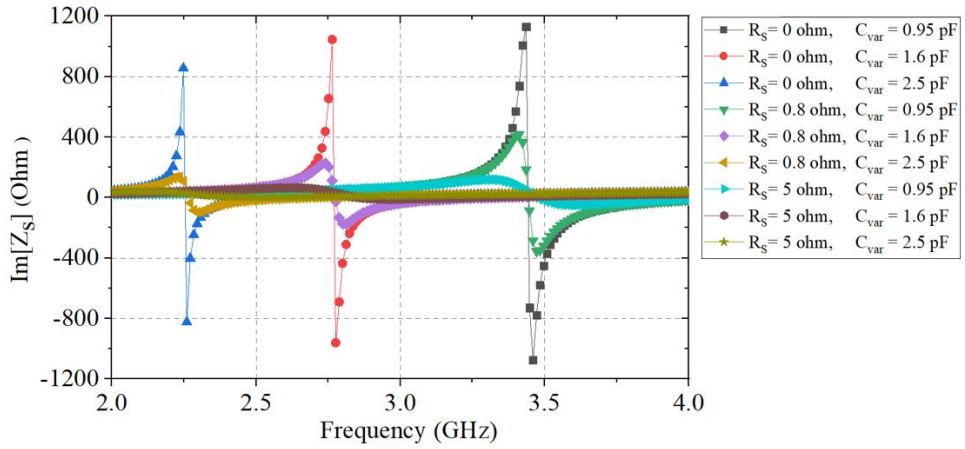


Fig. 3.17. Imaginary part of Z_S for an incident plane wave depending on the capacitance and R_S change of the varactors.

Table 3.3. Dimensions of the proposed design of polarization-dependent phase tunable reflector.

Parameter	Value	Parameter	Value
D	10 mm	g	0.4 mm
h	1.2 mm	ϵ_r	4.3

3.2.3 AR improvement through 1D phase tunable reflector

To verify that AR is effectively improved as expected in Fig. 3.7 by 1D phase tunable reflector designed in previous chapter, the simulation of designed spiral array antenna backed by 1D phase tunable reflector is performed. The AR simulation results by changing $\angle\Gamma_{xx}^R$ with $\angle\Gamma_{yy}^R$ fixed at -180° using the ideal varactors are shown in Fig. 3.18. AR is improved along the envelope of the optimum AR result calculated in Fig. 3.7. This is evidence of the accuracy of the analysis and developed equation in the previous chapter. The simulation results with a reflector using the practical varactors are shown in Fig. 3.19. Similar to the results of Fig. 3.18, but C_{var} initial value of practical varactor is 0.65pF, AR improvement is not seen above 3.4 GHz in Fig 3.19. Similarly, The AR simulation results by changing $\angle\Gamma_{yy}^R$ with $\angle\Gamma_{xx}^R$ fixed at -180° using the ideal varactors are shown in Fig. 3.20. AR is improved along the envelope of the optimum AR result calculated in Fig. 3.9. The simulation results with a reflector using the practical varactors are shown in Fig. 3.21. Similar to the results of Fig. 3.20, but C_{var} initial value of practical varactor is 0.65pF, AR improvement is not seen above 3.4 GHz in Fig 3.21.

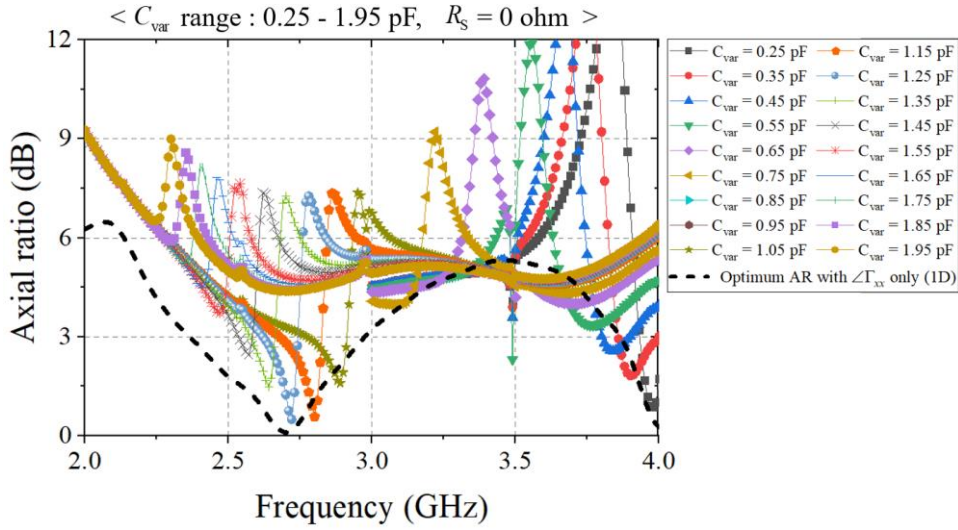


Fig. 3.18. Optimum AR result calculated in Fig. 3.7 and AR results of spiral antenna array with 1D reflector at broadside depending on capacitance of ideal varactor by changing $\angle\Gamma_{xx}^R$ of (1D) with $\angle\Gamma_{yy}^R$ fixed at -180° .

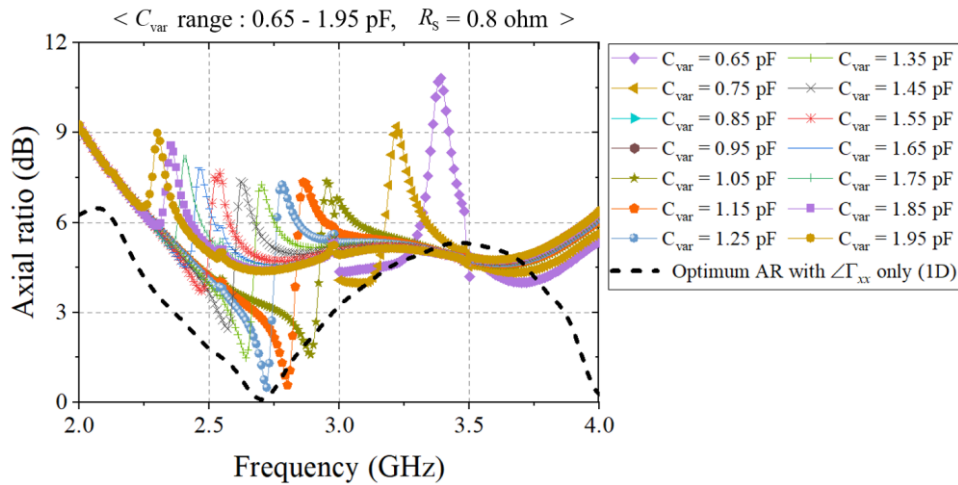


Fig. 3.19. Optimum AR result calculated in Fig. 3.7 and AR results of spiral antenna array with 1D reflector at broadside depending on capacitance of practical varactor by changing $\angle\Gamma_{xx}^R$ of (1D) with $\angle\Gamma_{yy}^R$ fixed at -180° .

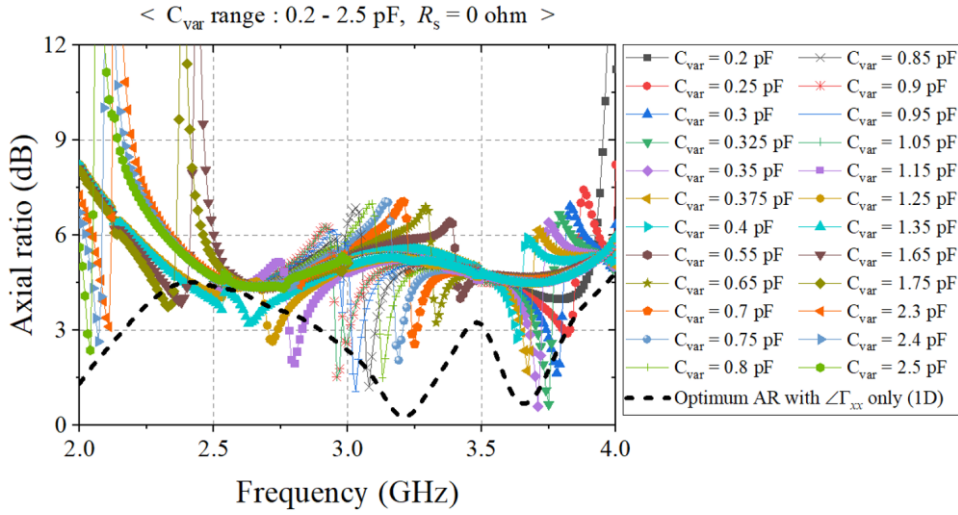


Fig. 3.20. Optimum AR result calculated in Fig. 3.7 and AR results of spiral antenna array with 1D reflector at broadside depending on capacitance of ideal varactor by changing $\angle\Gamma_{yy}^R$ of (1D) with $\angle\Gamma_{xx}^R$ fixed at -180° .

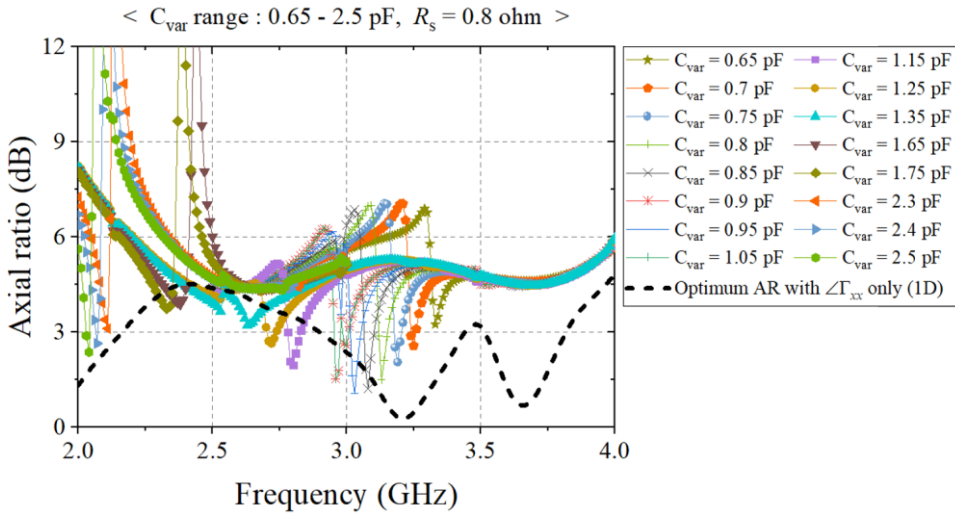


Fig. 3.21. Optimum AR result calculated in Fig. 3.7 and AR results of spiral antenna array with 1D reflector at broadside depending on capacitance of practical varactor by changing $\angle\Gamma_{yy}^R$ of (1D) with $\angle\Gamma_{xx}^R$ fixed at -180° .

3.2.4 AR improvement through 2D phase tunable reflector

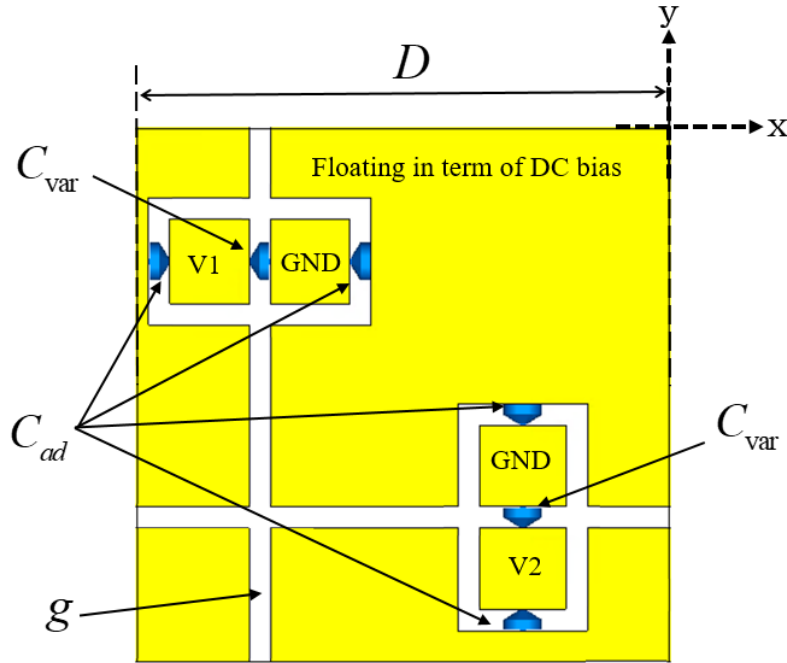


Fig. 3.22. Proposed design model of polarization-dependent 2D phase tunable reflector with varactors.

As Fig. 3.5 shows, designing a reflector that can $\angle\Gamma_{xx}^R$ and $\angle\Gamma_{yy}^R$ individually increases the degree of freedom of AR improvement. Designing a 2D phase tunable reflector using a varactors requires additional pads for bias, as shown in Fig. 3.22. An appropriate capacitance value of C_{ad} should be chosen to operate short in the entire RF band to be used. Since the actual device has self resonance frequency (SRF), it is not possible to use a capacitor having a large value unconditionally, so capacitance value of 10 pF is used in this paper. Through this structure, two voltages, V1 and V2, enable phase

adjustment according to each polarization. However, this structure has a disadvantage in that the number of varactors is required more than the 1D strip structure because all pads are separated. Accordingly, the number of C_{var} connected in parallel in (3.5) increases, which makes it difficult to select a desired frequency band. Even if the length of period D is reduced to reduce the value of C, the number of varactors that must be connected in parallel increases, so reducing the value of total capacitance has limitation. The space required for manufacturing is also limited compared to 1D structure. The length of the period D is limited because a hole for the connector is required.

Fig. 3.23 shows the simulation results of designing a reflector that can simultaneously adjust $\angle\Gamma_{xx}^R$ and $\angle\Gamma_{yy}^R$ separately in 2–4 GHz using an ideal varactors. Period D was chosen, ignoring the issues to be considered for fabrication. As predicted in Fig. 3.5, AR improves over the entire band compared to the case where only one of $\angle\Gamma_{xx}^R$ or $\angle\Gamma_{yy}^R$ can be adjusted, which means that improvements can be made to an uncoverable range if only one of $\angle\Gamma_{xx}^R$ or $\angle\Gamma_{yy}^R$ can be adjusted. The simulation results with a reflector using the practical varactors are shown in Fig. 3.24. Although the result of the practical 2D reflector is reduced in bandwidth compared to the practical 1D reflector, 2D reflector enable to improve AR within the operation band. In this paper, 1D reflector with array antenna was fabricated and measured because of the problem of the large number of

varactors required and limitation of bandwidth due to spatial limitation. 1D reflector has structural simplicity and advantage in bandwidth compared to 2D reflector.

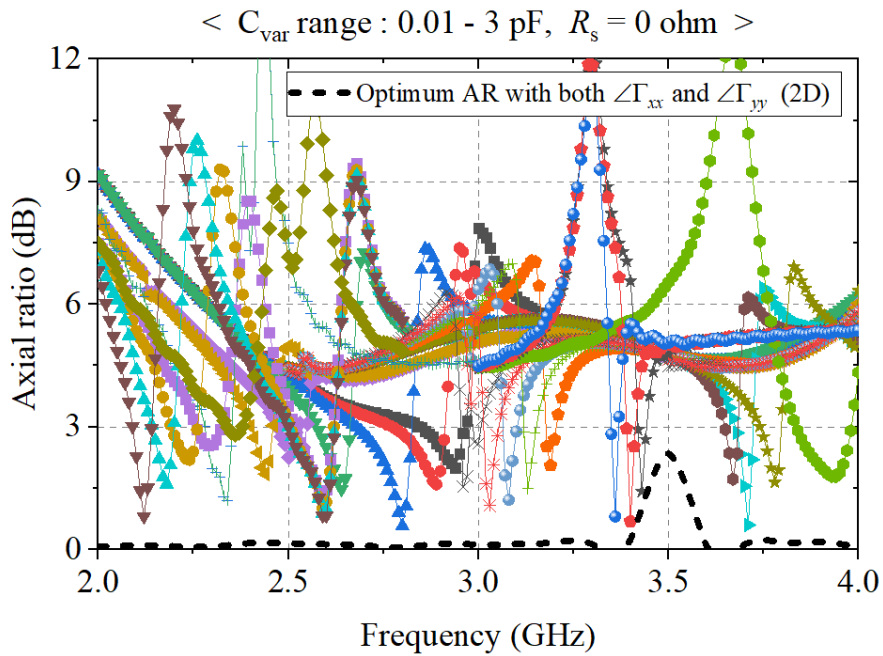


Fig. 3.23. Optimum AR result calculated in Fig. 3.5 and AR results of spiral antenna array with 2D reflector at broadside depending on capacitance of ideal varactor.

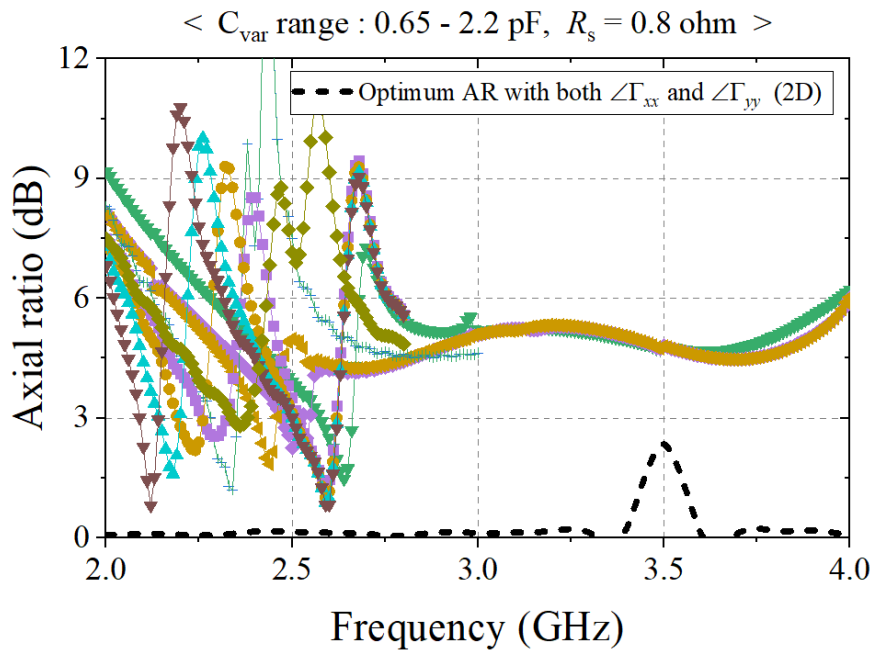


Fig. 3.24. Optimum AR result calculated in Fig. 3.5 and AR results of spiral antenna array with 2D reflector at broadside depending on capacitance of practical varactor.

3.3. Design of spiral antenna array backed by polarization-dependent 1D phase tunable reflector

It is difficult to realize a reflector that individually adjusts the phase of each polarization. Therefore, we investigated how much the ratio is improved by changing the reflection phase of only one polarization while fixing the reflection phase of one polarization.

To confirm whether the AR improved as desired when the reflector was manufactured and placed backed by the antenna, detailed design for fabrication was conducted. The required $\angle\Gamma_{yy}^R$ is -180° , and the required $\angle\Gamma_{xx}^R$ is approximately from -250° to -270° . This can be achieved by adjusting the bias voltage applied to the varactors as shown in the previous chapter. At first, periodic boundary simulation included varactor modeling, balun design, and connectors for RF signal input for infinite array was performed through CST time domain solver and then simulation of 4×4 array with dummy was performed for actual implementation, which included a circuit for bias voltage and a hole for antenna support.

3.3.1 Periodic boundary simulation for infinite array

The periodic boundary simulation model is shown in Fig. 3.25. The spacing between the antenna and reflector is 23 mm, 0.21 wavelength at 2.8 GHz.

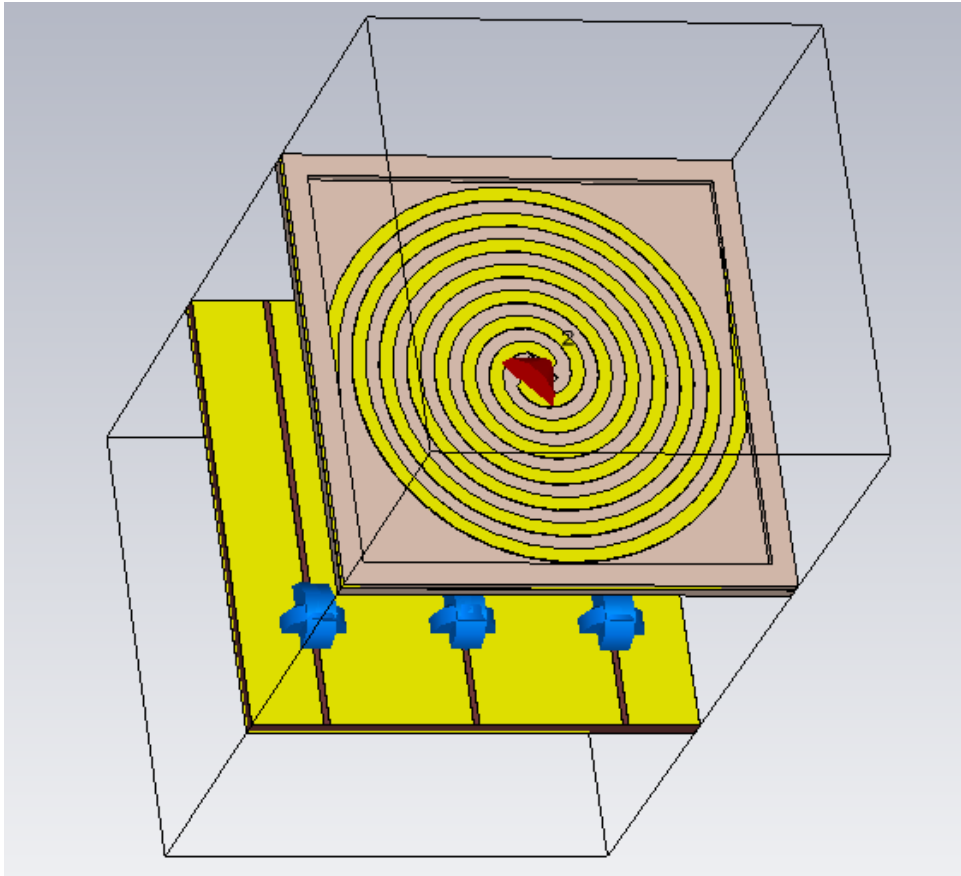


Fig. 3.25. Periodic boundary model of spiral antenna backed by polarization-dependent phase tunable reflector with varactors.

Fig. 3.26 shows the AR results and the radiation efficiency results of spiral antenna array of periodic structure at broadside. As expected, the AR improves below 3 dB as the varactor capacitance

changes. Unlike the array antenna structure using absorbers or resistors which can lose 30–50% of power loss, the proposed array antenna structure has more than 80% efficiency in the target frequency band of improving AR, which can be sweep by changing bias voltage applied to varactors. The AR was improved while maintaining the radiation efficiency more than 80% compared to case of antenna simply backed by PEC plane. Frequency band with an efficiency above 80% and an AR below 3 dB range from 2.58 GHz to 2.92 GHz. Fig. 3.27 shows the input reflection coefficient for periodic boundary simulation of a spiral antenna array. Designed array antenna has a reflection coefficient of less than -10 dB in the entire band.

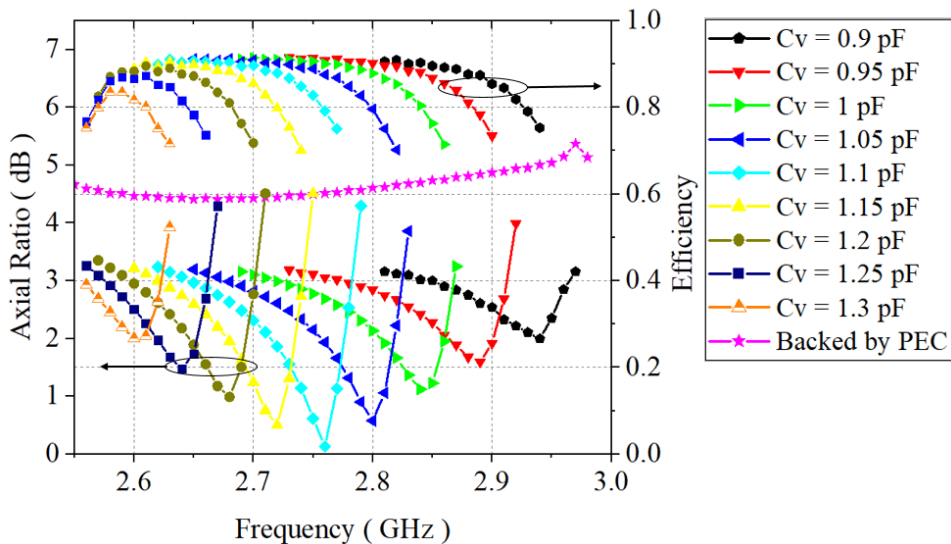


Fig. 3.26. AR results and the radiation efficiency results of spiral antenna array of periodic structure at broadside depending on capacitance of varactor.

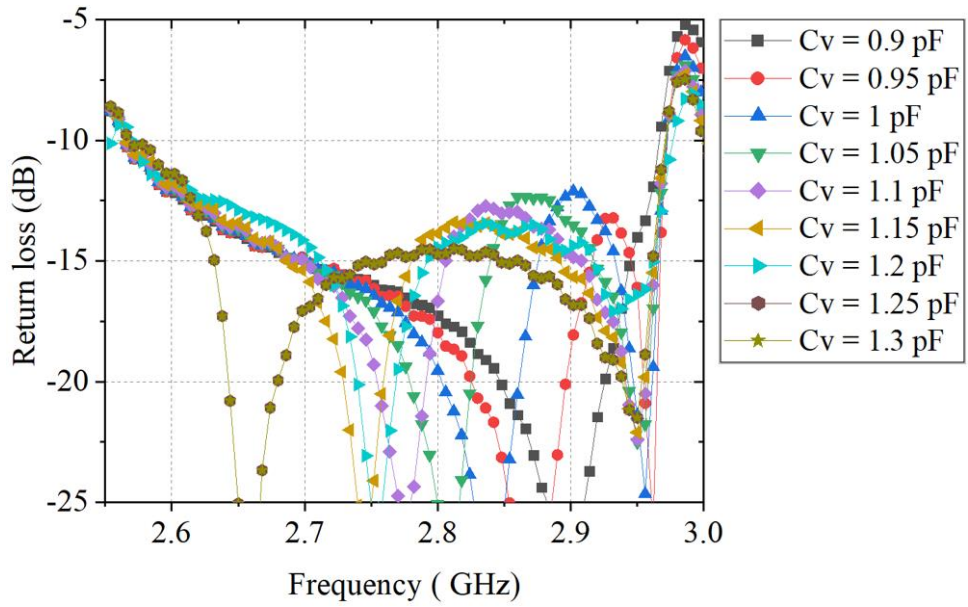


Fig. 3.27. Input reflection coefficient of spiral antenna array of periodic structure depending on capacitance of varactor.

3.3.2 4×4 array simulation with dummy

Through periodic boundary simulation for infinite array effective operation of the polarization-dependent phase tunable reflector is verified in the previous chapter. In this chapter, simulation of 4×4 array with dummy was performed for actual implementation.

A 4×4 array with dummy simulation model is shown in Fig. 3.28. The elements along the first column, sixth column, first row, and sixth row were terminated by 50Ω loads to reduce the array edge effects. The active region of the array is the inner 4×4 elements.

Fig. 3.29 shows the AR results and the radiation efficiency results of 4×4 spiral array with dummy at broadside. As expected, the results of the periodic boundary simulation and the results of the 4×4 array simulation are in full agreement with the same frequency band, which means that the realization of array with dummy is achieved as desired. Frequency band with an efficiency above 80% and an AR below 3 dB range from 2.58 GHz to 2.92 GHz.

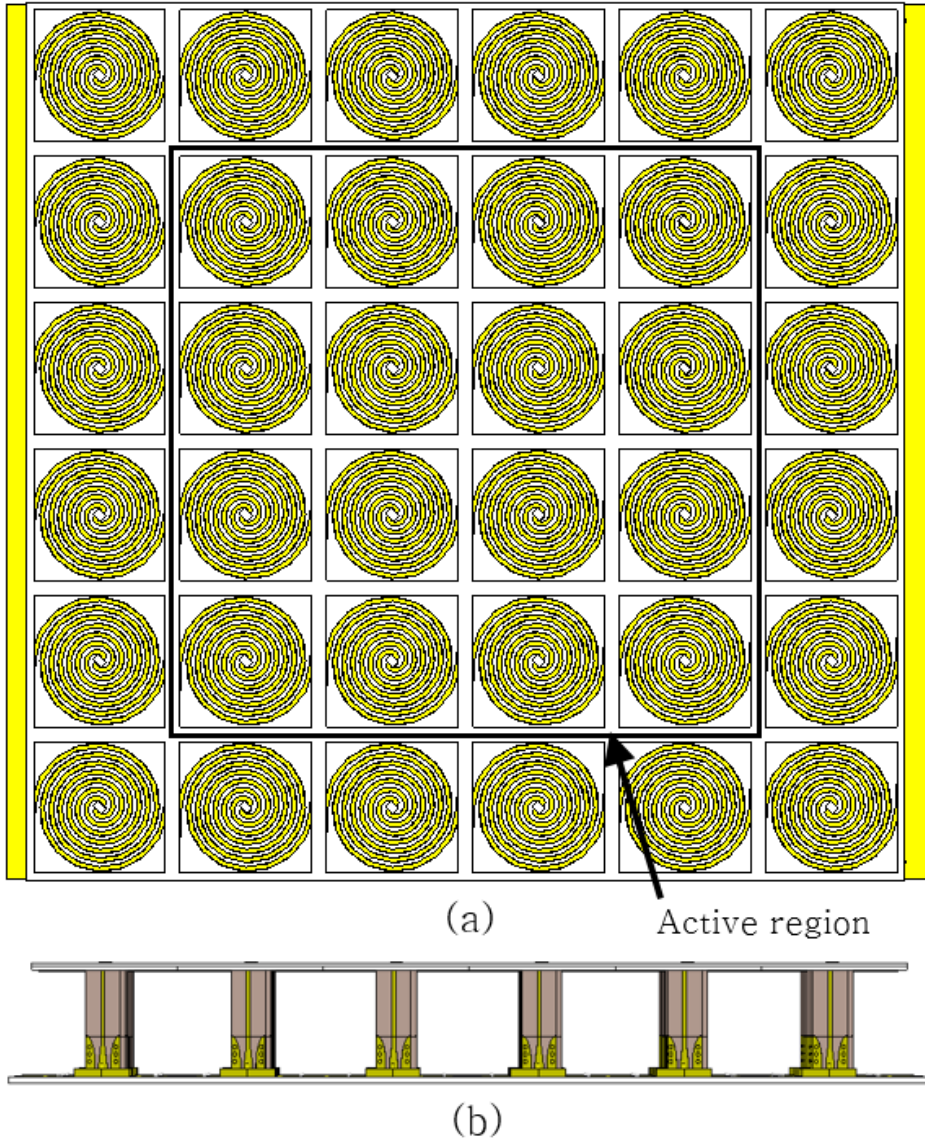


Fig. 3.28. 4×4 array with dummy simulation model backed polarization-dependent phase tunable reflector (a) top view (b) side view.

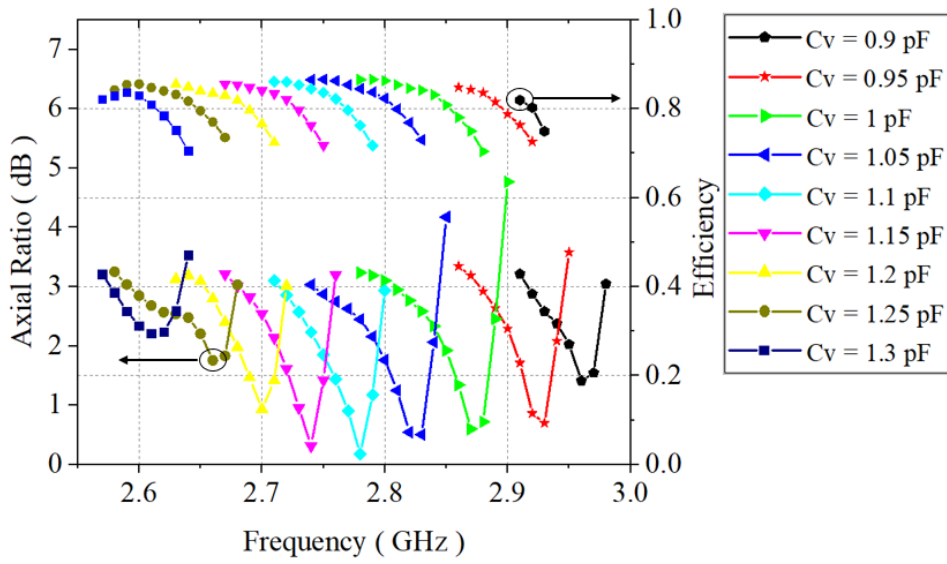


Fig. 3.29. AR results and the radiation efficiency results of 4×4 array with dummy at broadside depending on capacitance of varactor.

3.4. Fabrication and measurement results

The polarization-dependent phase tunable reflector was fabricated in Fig. 3.30. A 4×4 array with dummy of the fabricated array with polarization-dependent phase tunable reflector is depicted in Fig. 3.31.

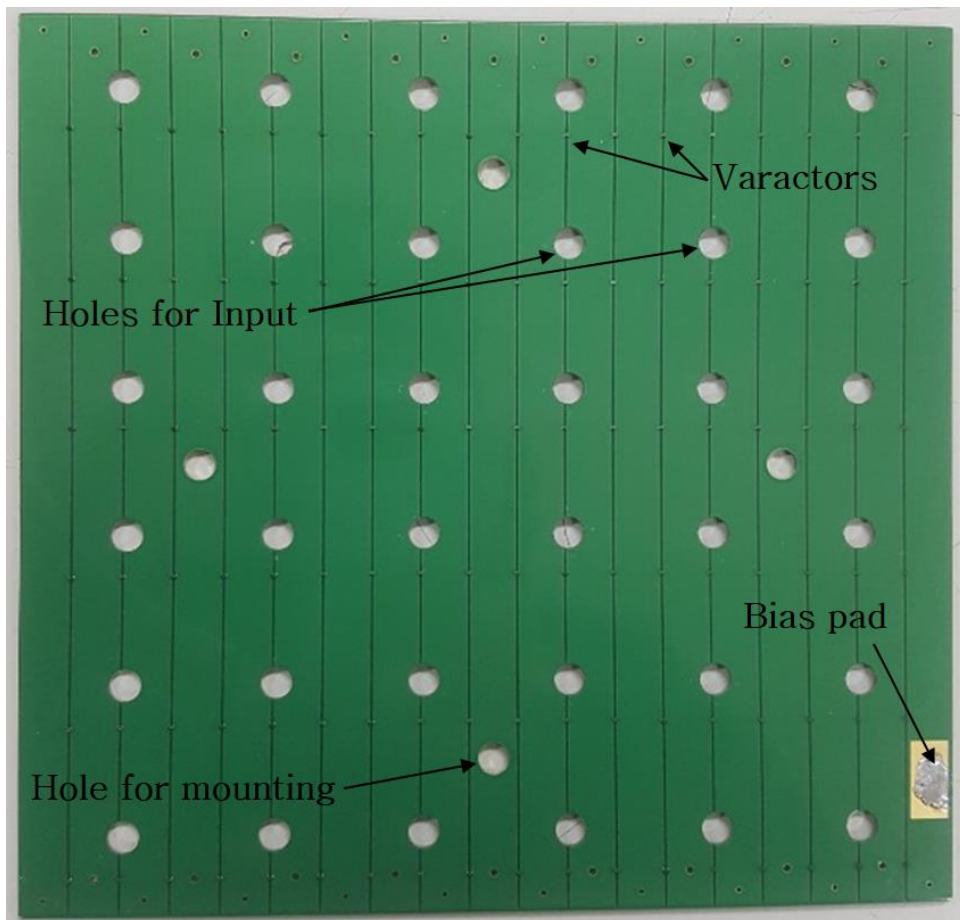
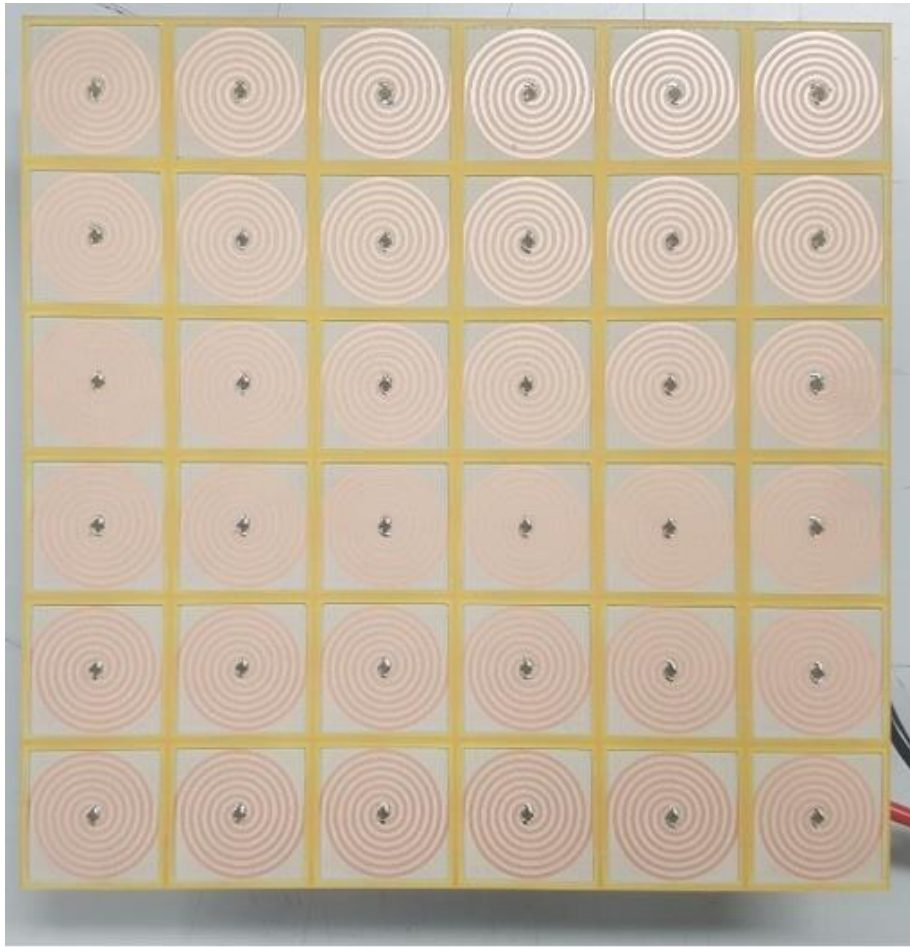
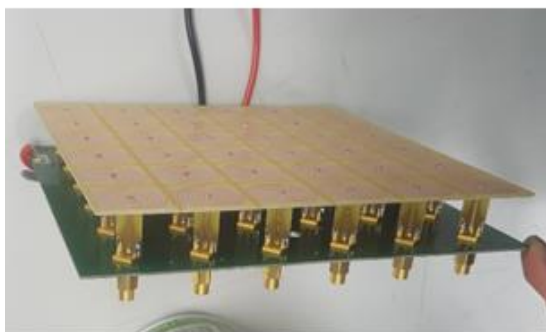


Fig. 3.30. The fabrication model of polarization-dependent phase tunable reflector.



(a)



(b)



(c)

Fig. 3.31. 4×4 array with dummy fabrication model backed polarization-dependent phase tunable reflector (a) top view (b) perspective view (c) back view.

The total array pattern measurement was performed by measuring each of the 16 active element patterns and synthesizing 16 active element patterns.

Before performing the pattern measurement in the chamber, the S parameter measurement for all 16 ports was performed to check that the fabrication model is consistent with the simulation model. Fig. 3.32 and Fig. 3.33, respectively, show the reflection coefficient simulation and measurement results for all 16 ports at 1 GHz to 7 GHz. Although the overall level of reflection coefficient measurement results has risen slightly and the frequency band has shifted slightly compared to simulation results, measurement results and simulation results have high consistent, which means that the fabrication model is consistent with the simulation model.

Fig. 3.34 and Fig. 3.35, respectively, show the reflection coefficient simulation results and measurement results for all 16 ports from 2.4 GHz to 3.2 GHz which is target band for AR improvement and the measuring band in the chamber. Similarly, although the overall level has risen slightly and the frequency band has shifted slightly, measurements and simulations have high consistent. The reflection coefficient results of less than -10 dB are obtained over the entire target band.

The mounted model in chamber for the measurement is shown in Fig. 3.36. Fig. 3.37 shows 4×4 array with dummy fabrication model with a circuit implemented using series batteries to adjust the voltage applied to the varactors of reflector.

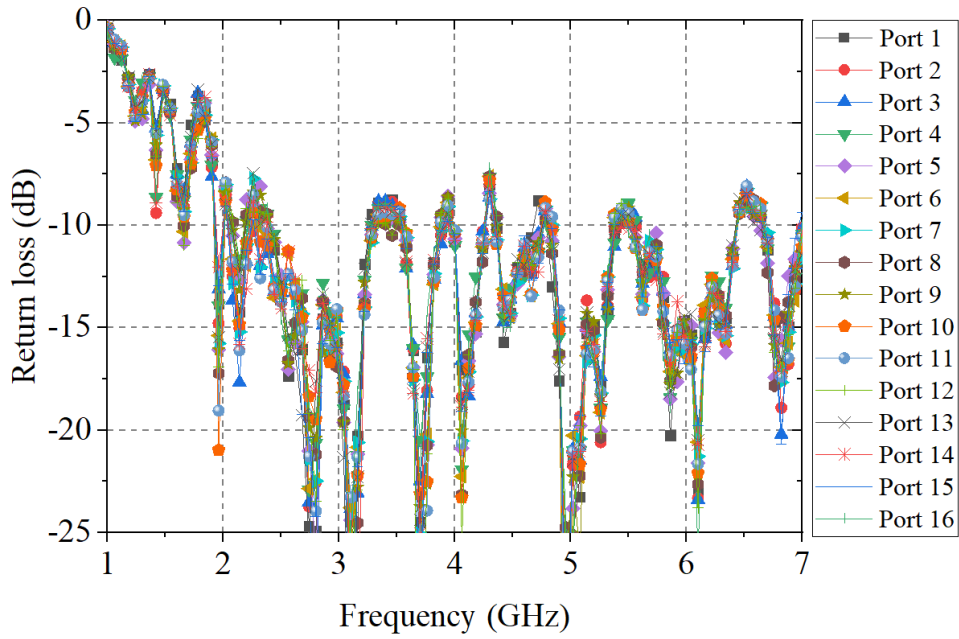


Fig. 3.32. Reflection coefficient simulation results of 4×4 array with dummy for all 16 ports at 1 GHz to 7 GHz.

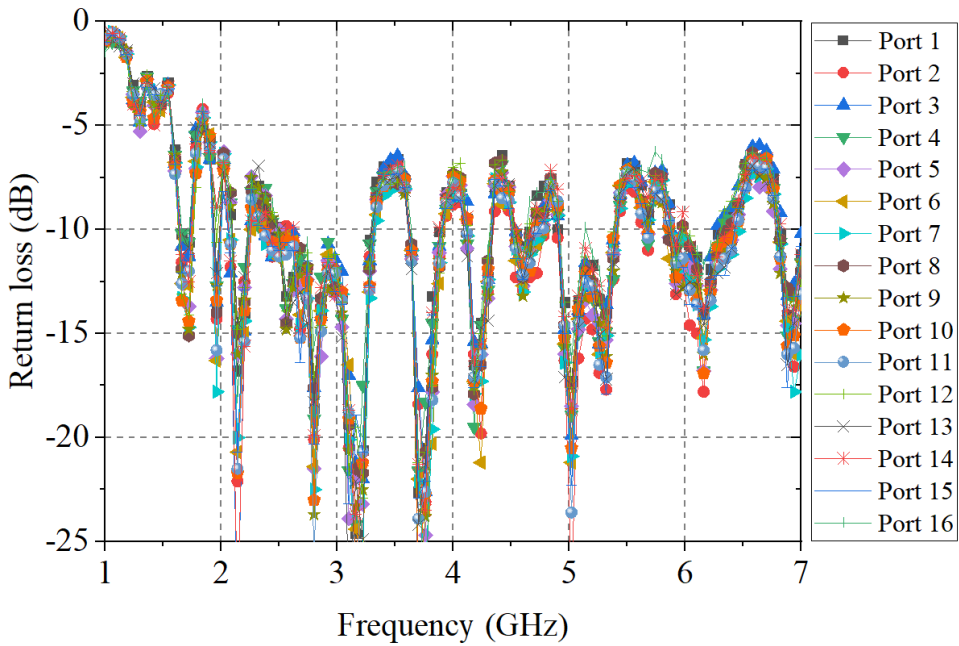


Fig. 3.33. Reflection coefficient measurement results of 4×4 array with dummy for all 16 ports at 1 GHz to 7 GHz.

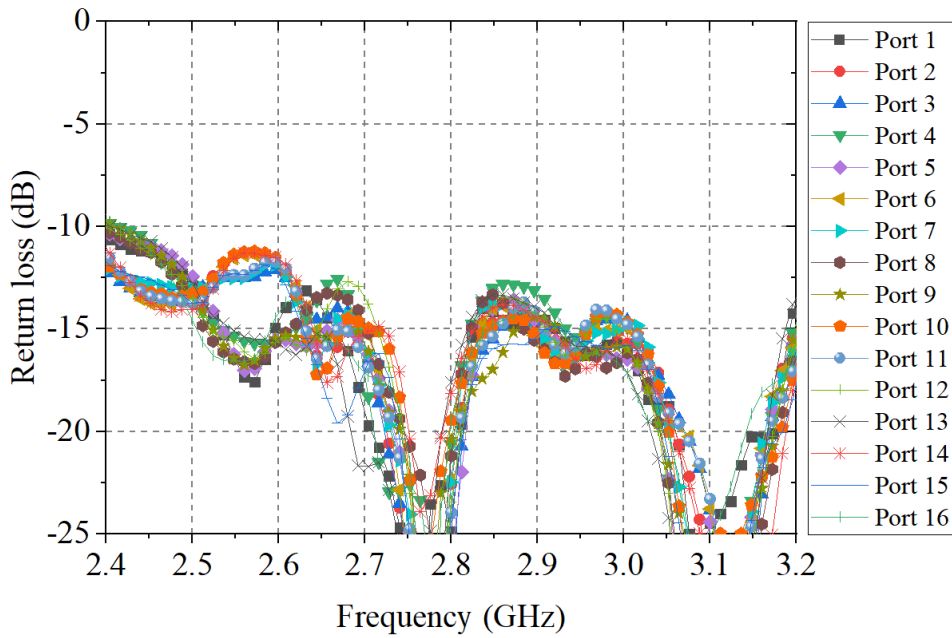


Fig. 3.34. Reflection coefficient simulation results of 4×4 array with dummy for all 16 ports at 2.4 GHz to 3.2 GHz.

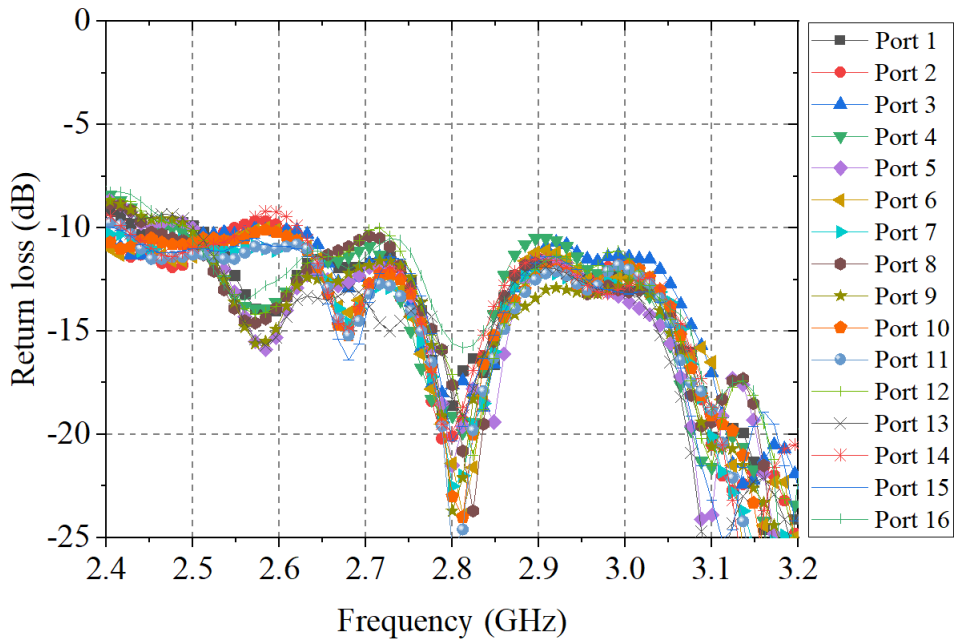


Fig. 3.35. Reflection coefficient measurement results of 4×4 array with dummy for all 16 ports at 2.4 GHz to 3.2 GHz.

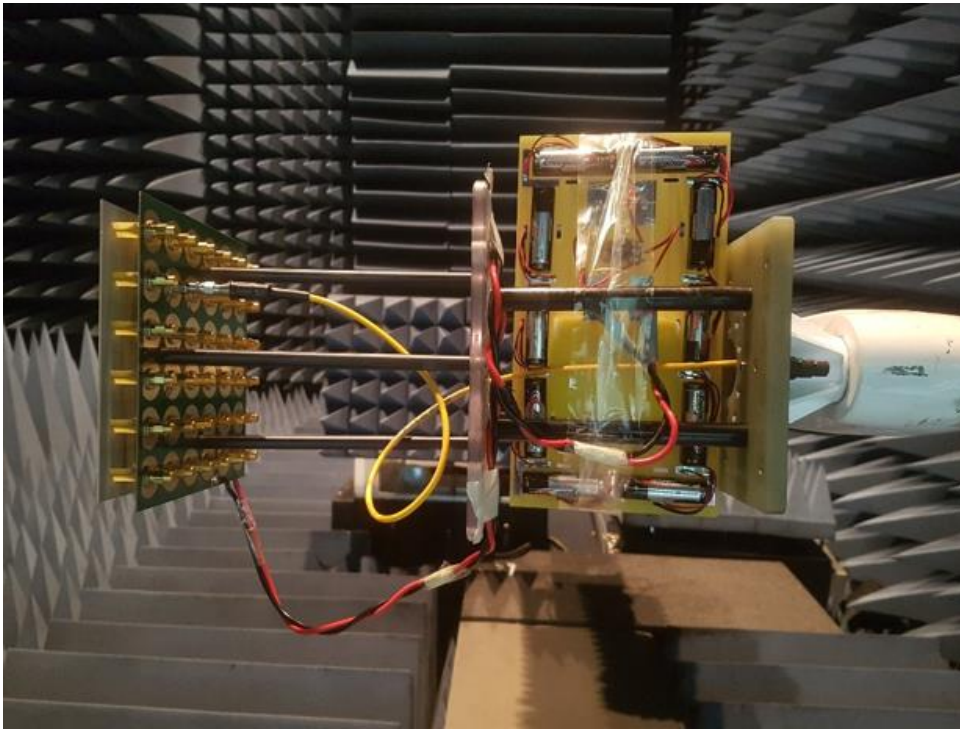


Fig. 3.36. The mounted model in chamber for the measurement.

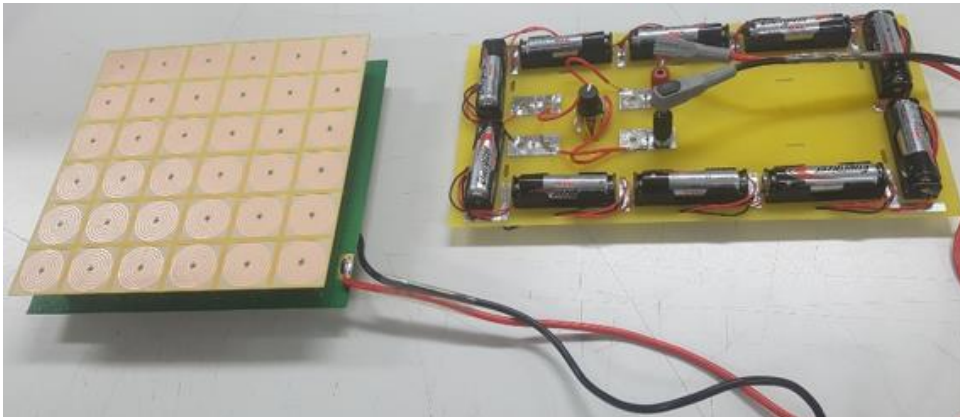


Fig. 3.37. 4×4 array with dummy fabrication model with a circuit implemented using series batteries to adjust the voltage applied to the varactors of reflector.

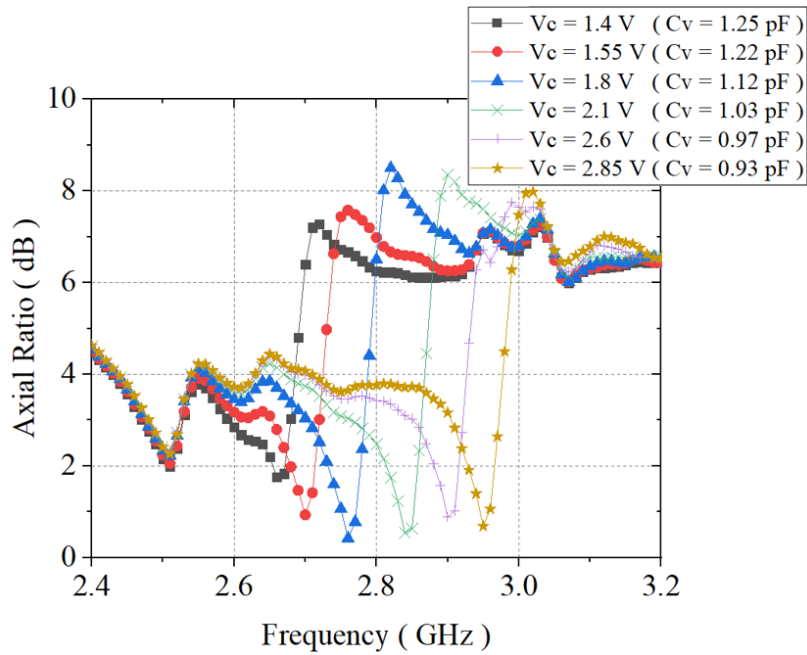


Fig. 3.38. AR simulation results of 4×4 array with dummy depending on bias voltage applied to varactors on reflector.

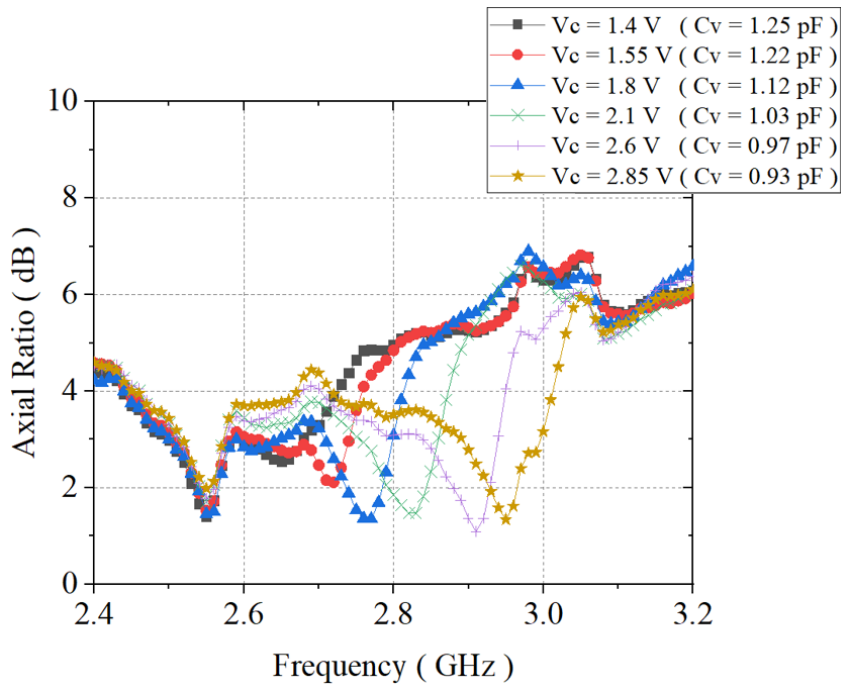


Fig. 3.39. AR measurement results of 4×4 array with dummy depending on bias voltage applied to varactors on reflector.

Fig. 3.38 and Fig. 3.39, respectively, show AR simulation and measurement results at broadside of 4×4 array with dummy fabrication model backed by polarization-dependent phase tunable reflector. AR improvement can be achieved through the measurement results in Fig. 3.38 by changing bias voltage applied to varactors on polarization-dependent phase tunable reflector.

In order to confirm that the measurement results are consistent with the simulation results in terms of efficiency, the gain results over frequency band were measured. Fig. 3.40 and Fig. 3.41 show the simulation and measurement results of RHCP gain and LHCP gain at broadside, respectively, at 2.4–3.2 GHz when bias voltage of 2.1 V is applied to varactors on reflector. The measurement results of both the RHCP gain and the LHCP gain are consistent with the simulation results in the target frequency band marked with yellow where the AR is improved when bias voltage of 2.1V is applied. The close agreement between the measurement results and the simulation results of RHCP gain and LHCP gain in the entire frequency band proved that the designed and fabricated model has the efficiency of 80% or more at the point where the AR improvement occurred.

In the case of applying bias voltage of 2.1 V to varactors, the RHCP gain pattern, LHCP gain pattern, and AR characteristics at 2.8 GHz within the band marked by the yellow in Fig. 3.40 were measured in both $\phi = 0^\circ$ cut and $\phi = 90^\circ$ cut. Fig. 3.42 and Fig. 3.43 show simulation and measurement results of RHCP gain and LHCP gain,

respectively, in $\phi=0^\circ$ cut. Fig. 3.44 and Fig. 3.45 show simulation and measurement results of RHCP gain and LHCP gain, respectively, in $\phi=90^\circ$ cut. Measurement results of gain and simulation results of gain have good agreement at all theta points in both $\phi=0^\circ$ cut and $\phi=90^\circ$ cut.

Fig. 3.46 shows AR measurement results in $\phi=0^\circ$ cut and $\phi=90^\circ$ cut when bias voltage of 2.1 V is applied to varactors on reflector. Proper values of AR below 2 dB in both $\phi=0^\circ$ cut and $\phi=90^\circ$ cut are achieved within the 3 dB beamwidth range which is marked in yellow, which means that fabricated array antenna is a good CP antenna array.

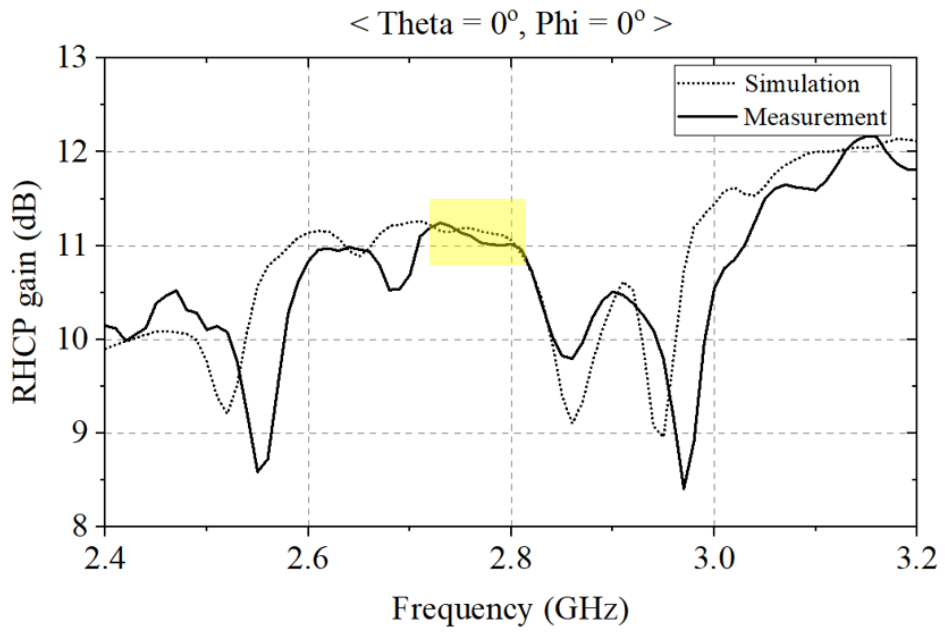


Fig. 3.40. Simulation and measurement results of RHCP gain at broadside in 2.4–3.2 GHz when bias voltage of 2.1 V is applied to varactors on reflector.

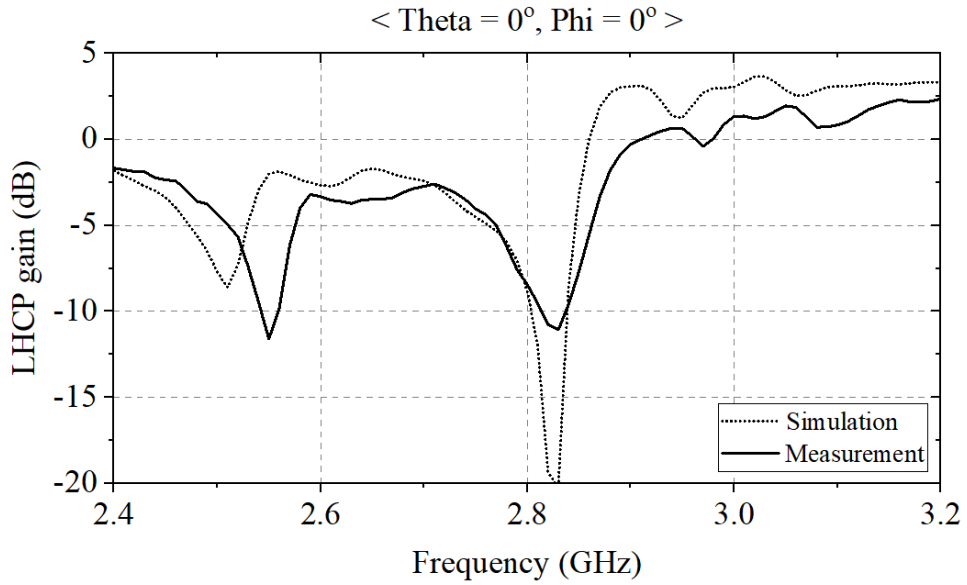


Fig. 3.41. Simulation and measurement results of LHCP gain at broadside in 2.4–3.2 GHz when bias voltage of 2.1 V is applied to varactors on reflector.

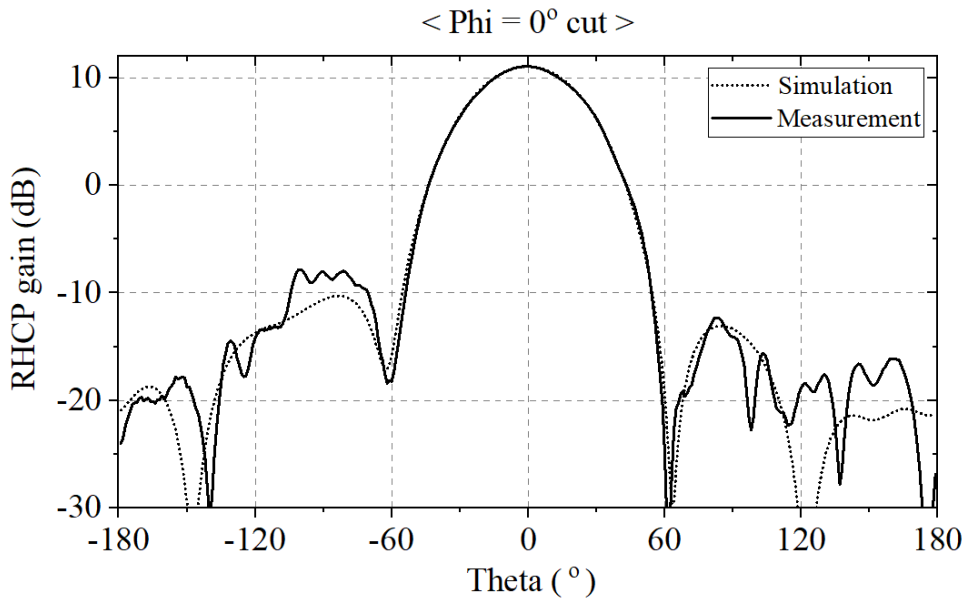


Fig. 3.42. Simulation and measurement results of RHCP gain pattern in $\phi = 0^\circ$ cut when bias voltage of 2.1 V is applied to varactors on reflector.

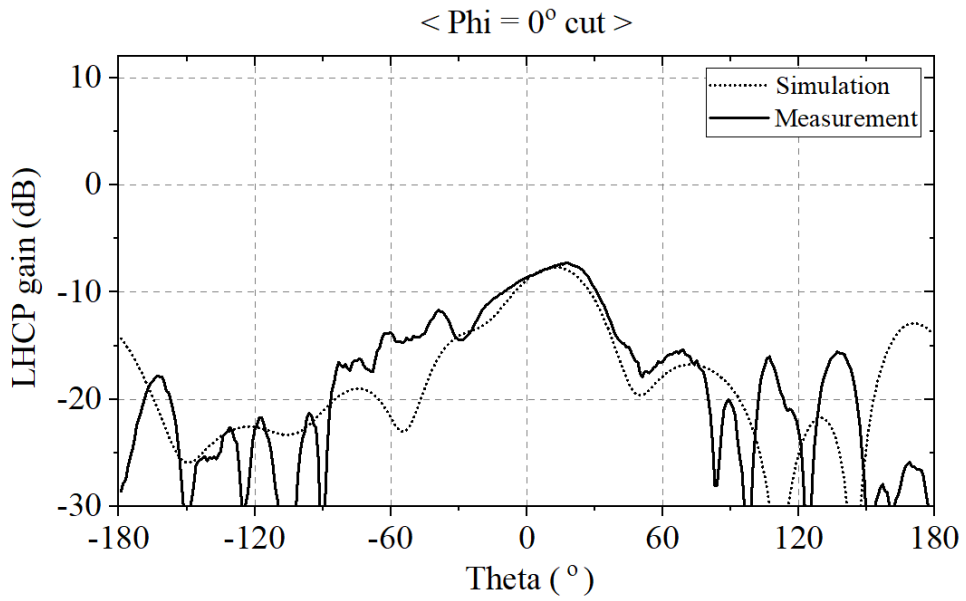


Fig. 3.43. Simulation and measurement results of LHCP gain pattern in $\phi = 0^\circ$ cut when bias voltage of 2.1 V is applied to varactors on reflector.

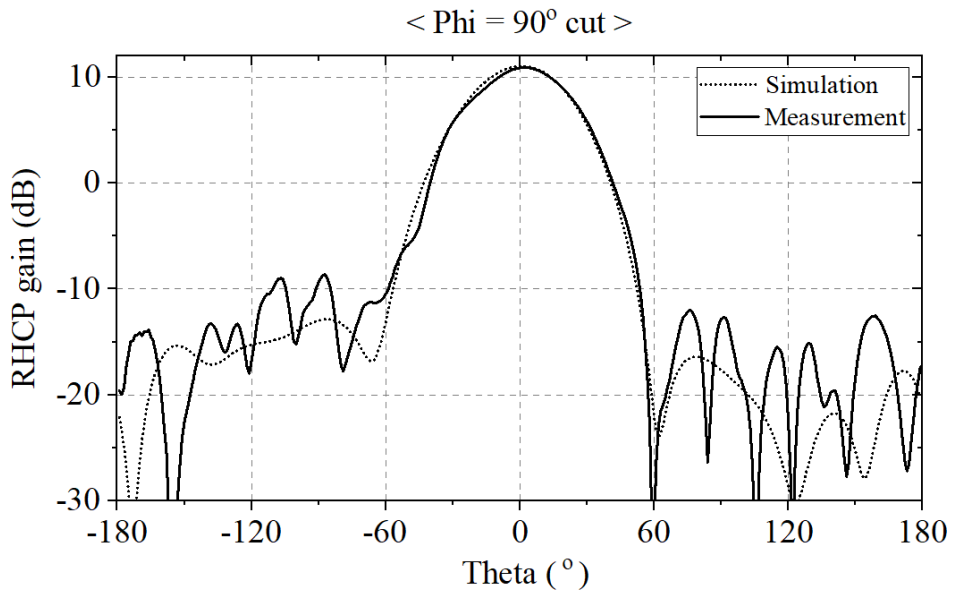


Fig. 3.44. Simulation and measurement results of RHCP gain pattern in $\phi = 90^\circ$ cut when bias voltage of 2.1 V is applied to varactors on reflector.

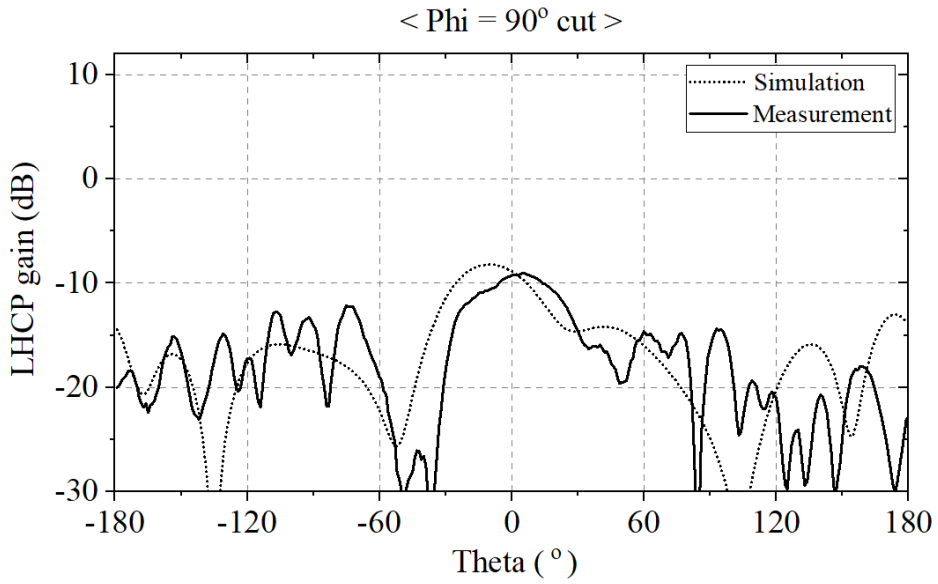


Fig. 3.45. Simulation and measurement results of LHCP gain pattern in $\phi = 90^\circ$ cut when bias voltage of 2.1 V is applied to varactors on reflector.

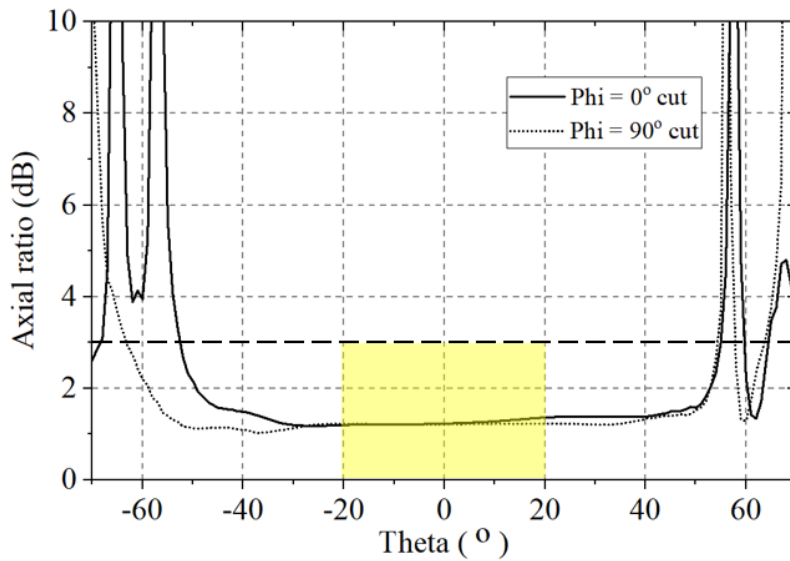


Fig. 3.46. AR measurement results in $\phi = 0^\circ$ cut and $\phi = 90^\circ$ cut when bias voltage of 2.1 V is applied to varactors on reflector.

Finally, the measurement results for beam steering are presented. Fig. 3.47 and Fig. 3.48 show the simulation and measurement results, respectively, of the RHCP pattern when the beam is steered from -30° to 30° in the $\phi=0^\circ$ cut. Fig. 3.49 and Fig. 3.50 show the simulation and measurement results, respectively, of the RHCP pattern when the beam is steered from -30° to 30° in the $\phi=90^\circ$ cut. As expected in the simulation, the measurement results show beamforming is achieved from -30° to 30° in both the $\phi=0^\circ$ cut and the $\phi=90^\circ$ cut.

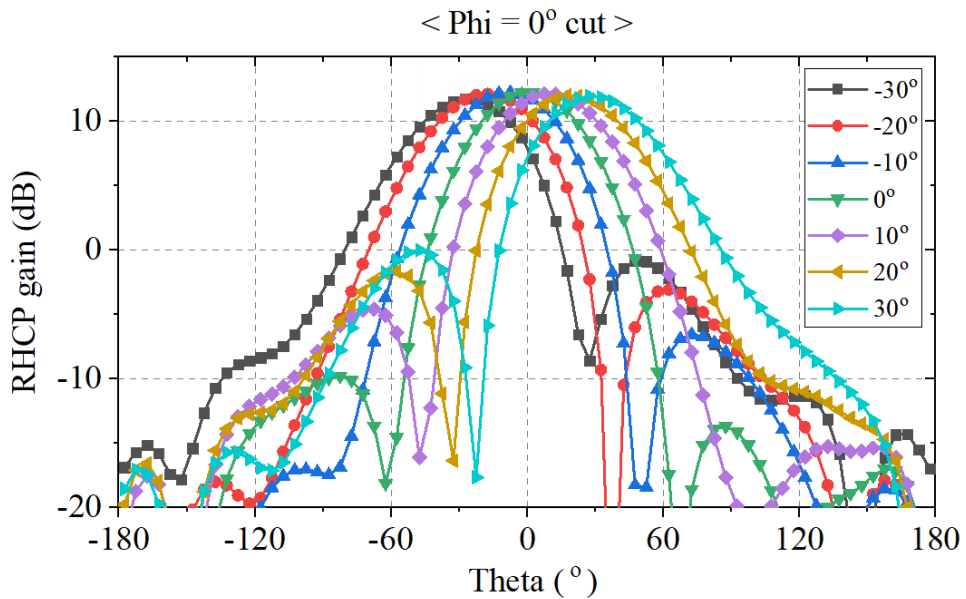


Fig. 3.47. Simulation results of the RHCP pattern depending on beam steering angle from -30° to 30° in the $\phi=0^\circ$ cut when bias voltage of 2.1 V is applied to varactors on reflector.

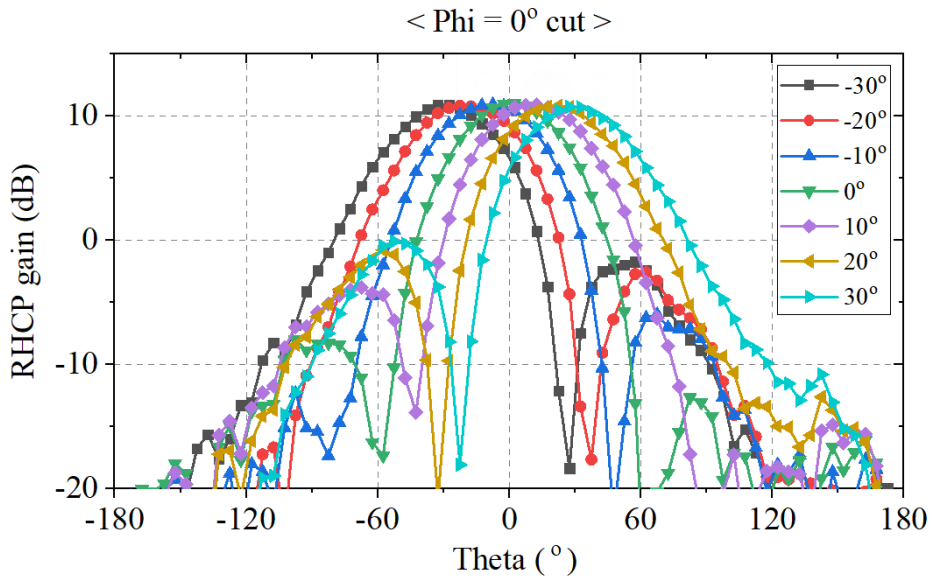


Fig. 3.48. Measurement results of the RHCP pattern depending on beam steering angle from -30° to 30° in the $\phi=0^\circ$ cut when bias voltage of 2.1 V is applied to varactors on reflector.

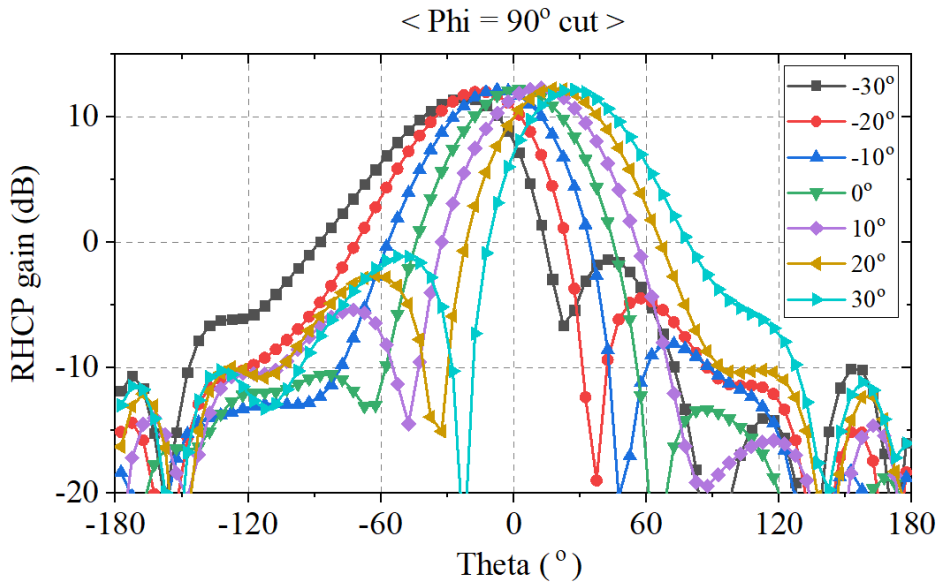


Fig. 3.49. Simulation results of the RHCP pattern depending on beam steering angle from -30° to 30° in the $\phi=90^\circ$ cut when bias voltage of 2.1 V is applied to varactors on reflector.

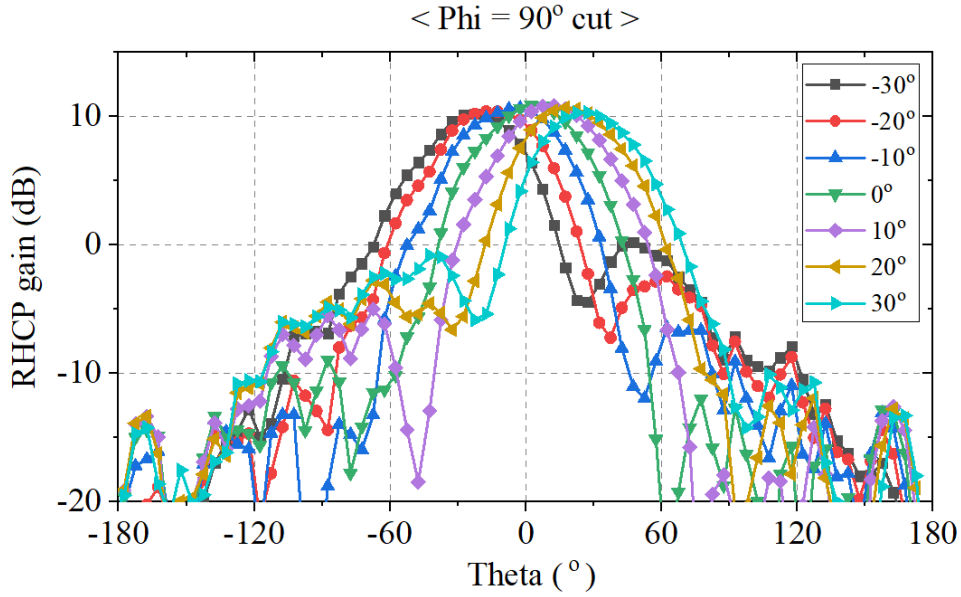


Fig. 3.50. Measurement results of the RHCP pattern depending on beam steering angle from -30° to 30° in the $\phi=90^\circ$ cut when bias voltage of 2.1 V is applied to varactors on reflector.

Instead of presenting LHCP results, the AR measurement results that can more clearly identify CP characteristics are presented for when beam steering from -30° to 30° . Fig. 3.51 and Fig. 3.52 are the measurement results of AR when beam steering from -30° to 30° in $\phi=0^\circ$ cut and $\phi=90^\circ$ cut, respectively. The results within the 3 dB beamwidth are only plotted and all results of AR remained below 1.5 dB from -30° to 30° in both the $\phi=0^\circ$ cut and the $\phi=90^\circ$ cut. We implemented a spiral antenna capable of beam steering from -30° to 30° with excellent CP characteristics with an AR value of less than 1.5 dB within the 3 dB beamwidth.

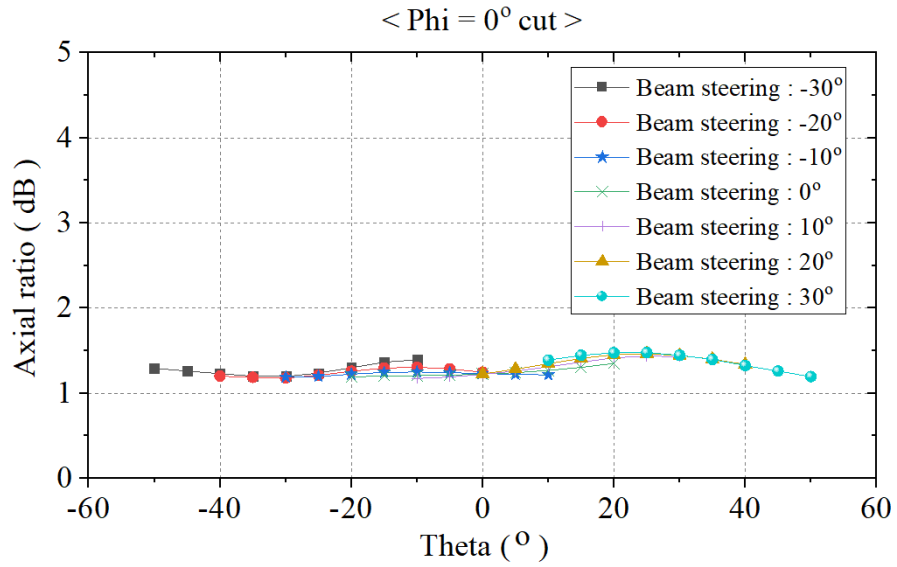


Fig. 3.51. Measurement results of the AR within beamwidth depending on beam steering angle from -30° to 30° in the $\phi=0^\circ$ cut when bias voltage of 2.1 V is applied to varactors on

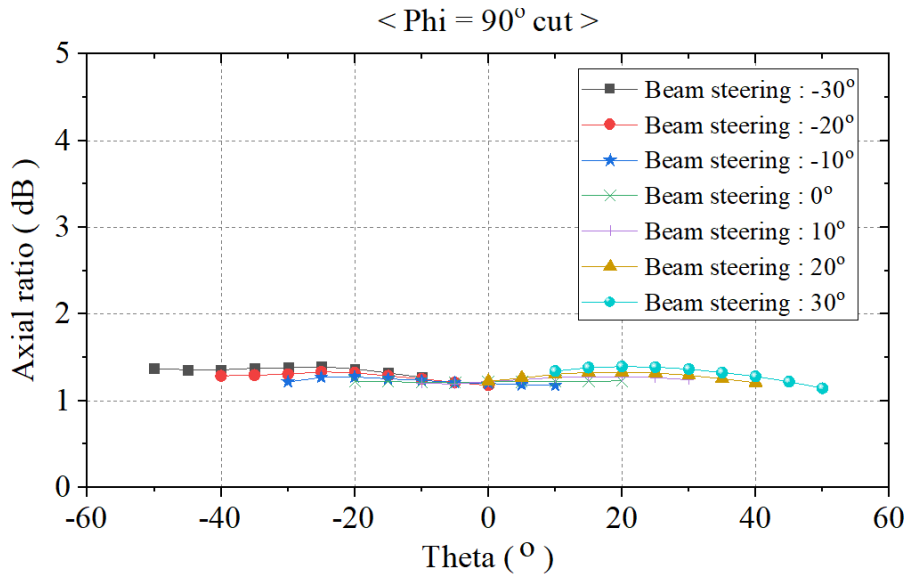


Fig. 3.52. Measurement results of the AR within beamwidth depending on beam steering angle from -30° to 30° in the $\phi=90^\circ$ cut when bias voltage of 2.1 V is applied to varactors on

3.5. Conclusion

In this chapter, to solve performance degradation problems when forming a unidirectional beam by attaching a PEC reflector close to the wideband antenna is described for low-profile wideband phased array antenna systems. At first we analyzed the reason why the AR could be deteriorated by the reflector. The reflected wave generated by the reflector is reflected back from the antenna with transmitted wave, causing multiple reflections, which causes AR deterioration. The AR deteriorates because the reflected reflection coefficient and the transmission coefficient are not symmetric about polarization. Based on this, Improvement of AR can be achieved by changing reflection phase of one polarization ($\angle\Gamma_{xx}^R$) while fixing reflection phase of the other polarization ($\angle\Gamma_{yy}^R$). A polarization-dependent phase tunable reflector is proposed to implement the required $\angle\Gamma_{xx}^R$ and $\angle\Gamma_{yy}^R$ using varactors.

To verify that AR is effectively improved by the polarization-dependent phase tunable reflector, spiral array antenna backed by the polarization-dependent phase tunable reflector was designed. The target frequency band is 2.55–2.95 GHz and the required $\angle\Gamma_{yy}^R$ is -180° , and the required $\angle\Gamma_{xx}^R$ is approximately from -250° to -270° . Periodic boundary simulation for infinite array was performed through CST time domain solver and then simulation of 4×4 array with dummy was performed for actual implementation. The

spacing between the antenna and reflector is 23 mm, 0.21 wavelength at 2.8 GHz. Designed array antenna has a reflection coefficient of less than -10 dB in the entire band. As expected, the results of the periodic boundary simulation and the results of the 4×4 array simulation are in full agreement with the same frequency band, which means that the realization of array with dummy is achieved as desired.

A 4×4 array with dummy is fabricated with polarization-dependent phase tunable reflector for measurement. Although the overall level of reflection coefficient measurement results has risen slightly and the frequency band has shifted slightly compared to simulation results, measurement results and simulation results have high consistent, which means that the fabrication model is consistent with the simulation model. AR improvement can be achieved through the measurement results by changing bias voltage applied to varactors on polarization-dependent phase tunable reflector. The close agreement between the measurement results and the simulation results of RHCP gain and LHCP gain in the entire frequency band proved that the designed and fabricated model has the efficiency of 80% or more at the point where the AR improvement occurred. Measurement and simulation results of the RHCP gain pattern, LHCP gain pattern, and AR have good agreement at all theta points in both $\phi = 0^\circ$ cut and $\phi = 90^\circ$ cut. As expected in the simulation, the measurement results show beamforming is achieved from -30° to 30° in both the $\phi = 0^\circ$ cut and the $\phi = 90^\circ$ cut.

According to this measurement process and results we

implemented a spiral array antenna capable of beam steering from -30° to 30° with excellent CP characteristics with an AR value of less than 1.5 dB within the 3 dB beamwidth without loss by applying polarization-dependent phase tunable reflector.

Bibliography

- [1] D. Parker and D. C. Zimmermann, “Phased arrays—part 1: theory and architectures,” *IEEE Transactions on Microwave Theory and Techniques*, vol. 50, no. 3, pp. 678–687, 2002.
- [2] Z. Changfei, F. Jiahui, K. Weidong, S. Quan, and G. Yan, “A miniaturized wideband Vivaldi antenna and phased array,” *in Proc. 3rd Asia–Pacific Conf. Antennas Propag.*, Jul. 2014, pp. 569–572.
- [3] C. T. Rodenbeck, S. G. Kim, W. H. Tu, M. R. Coutant, S. Hong, M. Y. Li, and K. Chang, “Ultra–Wideband Low–Cost Phased–Array Radars,” *IEEE Trans. Microwave Theory Tech.*, vol. 53, no. 12, pp. 3697–3703, Dec. 2005.
- [4] S. K. Garakoui, E. A. Klumperink, B. Nauta and F. E. van Vliet, “Phased–array antenna beam squinting related to frequency dependency of delay circuits,” *2011 European Radar Conference (EuRAD)*, pp. 416–419, 12–14 October 2011.
- [5] M. Cai, K. Gao, D. Nie, B. Hochwald, J. N. Laneman, H. Huang and K. Liu, “Effect of wideband beam squint on codebook design in phased–array wireless systems,” *2016 IEEE Global Communications Conference (GLOBECOM)*, 4–8 December 2016.
- [6] F. Hu and K. Mouthaan, “A 1–20 GHz 400 ps true–time delay with small delay error in 0.13 μm CMOS for broadband phased array antennas,” *2015 IEEE MTT–S International Microwave Symposium*, Phoenix, AZ, pp. 1–3, 17–22 May 2015.

- [7] Minyoung Yoon and Sangwook Nam, "7-Bit Multilayer True-time Delay up to 1016ps for Wideband Phased array antenna," *IEICE TRANS. ELECTRON.*, VOL.E102-C, NO.8 AUGUST 2019.
- [8] T. H. Liu, W.X. Zhang, M. Zhang, and K.F. Tsang, "Low profile spiral antenna with PBG substrate" , *Electron. Lett.*, Vol. 36, pp. 779–780, 2000.
- [9] J. M. Bell, and M. F. Iskander, "A low-profile Archimedean spiral antenna using an EBG ground plane," *IEEE Antennas and Wireless Propagation Letters*, vol. 3, pp. 223–226, December 2004.
- [10] Z. Li, G. M. Wang, Y. Cao, "A low-profile equiangular spiral antenna using a novel EBG ground plane" , *In antennas, Propagation & EM Theory, 2006. ISAPE ' 06. 7th International Symposium on*, pp. 1–3, 2006.
- [11] L. Yousefi, B. M. Iravani, and O. M. Ramahi, "Enhanced bandwidth artificial magnetic ground plane for low-profile antennas", *IEEE Antennas and Wireless Propagation Letters*, vol. 6, pp. 289–292, July 2007
- [12] L. Schreider, X. Begaud, X., Soiron, M., et al., "Broadband archimedean spiral antenna above a loaded electromagnetic band gap substrate" , *IET Microw. Antennas Propag.*, vol. 1, pp. 212–216, 2007.
- [13] M. Grelier, C. Djoma, M. Jousset, S. Malle ´ gol, A.–C. Lepage, X. Begaud, "Axial ratio improvement of an Archimedean spiral

- antenna over a radial AMC reflector” , *Appl. Phys.*, A 109, pp. 1081–1086, 2012.
- [14] H. Nyquist and S Brand, “Measurement of phase distortion” . *Bell. Syst. Tech. J.*, vol. 9, no. 3, pp. 522–549, 1930.
- [15] O. Ostwald, “Group and phase delay measurement with vector network analyzer ZVR” , Rohde &Schwarz, Munich, Germany, *Application Note 1EZ35_1E*, Jul. 10, 1997.
- [16] Agilent Network Analyzer Basics, *Agilent Technol.*, Santa Clara, CA, 2008.
- [17] Agilent ENA 2, 3 and 4 port RF Network Analyzers, *Agilent Technol.*, Santa Clara, CA, 2008.
- [18] M. Yoon and S. Nam, “Avoidance of off–switch resonance in true time delay line using cascaded switches,” *2016 URSI Asia–Pacific Radio Science Conference*, pp. 719 – 720, 21–25 August 2016.
- [19] Q. Liu, C.–L. Ruan, L. Peng, and W.–X. Wu, “A novel compact Archimedean spiral antenna with gap–loading,” *Prog. Electromagn. Res. Lett.*, vol. 3, pp. 169–177, 2008.
- [20] Analog Devices, “ High Isolation, Silicon SPDT, Nonreflective Switch, 9 kHz to 13.0 GHz,” *HMC1118 Datasheet*, 2017.
- [21] A. R. Eskandari and L. Mohammadi, “Group delay variations in wideband transmission lines: analysis and improvement,” *International Journal of Soft Computing Engineering (IJSCE)*, vol. 1, no. 4, pp. 122–128, 2011.

- [22] J. G. Willms, A. Ouacha, L. de Boer and F. E. van Vliet, “A wideband GaAs 6-bit true-time delay MMIC employing on-chip digital drivers,” *30th European Microwave Conference*, Paris, France, pp. 1–4, 2–5 October 2000.
- [23] J. Ahn, S. H. Cha, S. G. Cha and Y. J. Yoon, “Compact spiral element for wideband beam-steering arrays,” *IEEE Antennas and Wireless Propagation Letters*, vol. 16, pp. 1994–1997, 2017.
- [24] J. S. Pak, H. Kim, J. Lee and J. Kim, “Modeling and measurement of radiated field emission from a power/ground plane cavity edge excited by a through-hole signal via based on a balanced TLM and via coupling model,” *IEEE Transactions on Advanced Packaging*, vol. 30, no. 1, pp. 73–85, Feb. 2007.
- [25] F. Hu and K. Mouthaan, “A 1–21 GHz, 3-bit CMOS true time delay chain with 274 ps delay for ultra-broadband phased array antennas,” *2015 European Radar Conference (EuRAD)*, Paris, France, pp. 1347–1350, 9–11 Sept. 2015.
- [26] M. Kim, J. B. Hacker, R. E. Mihailovich and J. F. DeNatale, “A DC-to-40 GHz four-bit RF MEMS true-time delay network,” *IEEE Microwave and Wireless Components Letters*, vol. 11, no. 2, pp. 56–58, Feb. 2001.
- [27] Y. Du, J. Bao, Z. He and J. Jiang, “A X-band switched-line 5-bit phase shifter with RF MEMS multithrow switches,” *8th IEEE International Conference on Nano/Micro Engineered and Molecular Systems*, Suzhou, China, pp. 296–299, 7–10 Apr. 2013.

- [28] H. Nakano, et al, “Low-Profile Equiangular Spiral Antenna Backed by an EBG Reflector,” *IEEE Trans. Antennas Propag.*, vol. 57, no. 5, pp. 1309–1318, May 2009.
- [29] C. Djoma, M. Jousset, A. C. Lepage, S. Mallegol, C. Renard, and X. Begaud, “Maximal bandwidth of an Archimedean spiral antenna above a reflector,” *IEEE Antennas Wireless Propag. Lett.*, vol. 13, pp. 333–336, 2014.
- [30] C. Park and Y. Yoon, “Miniaturization of Archimedean spiral antenna for wideband beamforming arrays” , *Microw. Opt. Technol. Lett.*, Vol. 61, pp. 125–130, 2019.
- [31] D. Guha, A. Banerjee, C. Kumar, and Y. Antar, “Higher order mode excitation for high-gain broadside radiation from cylindrical dielectric resonator antennas” , *IEEE Trans Antennas Propag.*, Vol. 60, pp. 71–77, 2012.
- [32] C. Park, S. Cha, Y. Yoon, and H. Kim, “Double-arm hexagonal Archimedean spiral antenna for wideband compact array” , *IEEE Symp. On Antenna and Propagation*, San Diego, USA, 9–14 July 2017.
- [33] S. A. Tretyakov, C. R. Simovski, Dynamic model of artificial reactive impedance surfaces, *J. Electromagn. Waves Appl.*, 17, pp. 131–145 (2)

초 록

본 논문에서는 낮은 높이의 광대역 배열 안테나 시스템을 구현하기 위해 필요한 핵심 기술 개발에 관해 연구하였다. 레이더, 전자전, 무선 통신과 같이 많은 분야에서 활발히 사용되는 있는 배열 안테나는 산업이 고도화되면서 요구하는 시스템 스펙이 더욱 고급화되고 있다. 그 중 무인 비행체, 미사일 등과 같은 고속 이동체의 곡면에 배치할 수 있도록 하기 위해서는 낮은 높이의 안테나 설계가 필요한데, 특히 낮은 높이의 광대역 안테나는 구조적으로 설계에 큰 어려움이 있다. 이 논문에서 목표로 정한 응용 분야는 전자전에서 빔포밍을 이용하여 적의 위치를 탐색하고 해당 위치로 특정 주파수의 큰 전력의 신호를 전송하는 전파 방해기이다. 전파 방해기는 광대역의 주파수 대역 내에서 선택적으로 주파수를 선택하여 사용할 수 있도록 설계되어야 하므로 광대역으로 동작하는 시스템 구현이 필요하다. 낮은 높이의 광대역 배열 안테나 시스템은 크게 광대역 빔조향 네트워크와 낮은 높이의 광대역 배열 안테나로 구분할 수 있다. 본 논문에서는 각 부분에서의 문제를 분석하고 이를 해결하여 설계 및 구현하는 방향으로 연구를 진행하였다. 수행된 연구의 내용은 아래와 같다.

첫 번째로, 광대역 빔조향 네트워크를 구성하는 가장 핵심 요소인 실시간 지연회로를 구현할 때 필요한 기술을 개발하였다. 먼저 실시간 지연회로의 중요한 성능 지표인 지연 시간 특성에 영향을 줄 수 있는 3가지 요소들에 대해 분석하였다. 첫 번째 요소는 off 상태에서 보이는 커패시터에 의한 공진이다. 실시간 지연회로에서 공진이 발생하면 전체 시스템 성능이 악화될 수 있기 때문에 30 dB 이상의 격리 특성을 갖는 스위치를 사용하여야 한다. 두 번째로 분석한 요소는 불연속에 의해 나타나는 반사파로 이는 실시간 지연회로와 전체 시스템을 구성할 때 매칭이 필수적으로 수행되어야 하는 이유가 된다. 마지막으로 분석한 요소는 안테나 임피던스에 의한 반사 손실이다. 광대역 안테나의

임피던스는 주파수에 따라 변하게 되는데 이는 안테나에 인가되는 신호의 위상을 변화시켜 배열 안테나 시스템 성능에 영향을 줄 수 있다. 몬테 카를로 시뮬레이션을 통해 안테나 임피던스 변화에 따른 위상 오차가 빔조향각과 사이드 로브 레벨에 얼마나 영향을 주는지 확인하였다. 배열 안테나를 설계하여 해당 안테나의 능동 반사 계수를 통해 이를 검증하였다. 실시간 지연회로의 설계를 진행할 때 추가적인 이슈는 소형화가 있다. 앞에서 분석한 3가지 요소를 고려하여 7-bit 적층 실시간 지연회로를 설계하였다. 제작 및 측정을 통해 설계한 실시간 지연회로가 손실에 따른 지연시간, 높은 bit 수, 저전력의 장점을 가지는 것을 확인하였다. 마지막으로 광대역 안테나 시스템을 구성하여 제작된 실시간 지연회로를 검증하였다. 측정을 통해 제작된 광대역 안테나 시스템이 3:1 대역에서 빔 스캔트 현상 없이 빔조향이 가능함을 확인하였고 소형화된 실시간 지연회로가 제대로 동작함을 검증하였다.

두 번째로, 낮은 높이의 광대역 안테나를 구현에 필요한 기술로 광대역 안테나 가까이 반사판을 배치하여 단방향 빔을 형성할 때 발생하는 문제점을 분석 및 극복하였다. 낮은 높이의 광대역 배열 안테나에 가장 적합한 안테나는 구현이 쉽고 소형화에 장점이 있는 스파이럴 안테나이다. 양방향 패턴을 갖는 스파이럴 안테나는 단방향 패턴을 만들어 주기 위해 반사판이 필요한데 해당 반사판으로 인해 매칭과 축비에 문제가 생기는 큰 단점이 있다. 본 논문에서는 먼저 반사판이 축비를 악화시키는 이유에 대해 분석하였다. 분석을 기반으로 축비 개선을 위해 varactor를 사용한 polarization-dependent 위상 조절 반사판을 제안하였다. polarization-dependent 위상 조절 반사판이 효과적으로 축비를 개선하는지 확인하기 위해 스파이럴 안테나와 함께 배치하여 설계하였다. 주기 구조를 통해 무한 배열 시뮬레이션을 진행하여 원하는 주파수 대역에서 축비가 효과적으로 개선되는 것을 확인하였다. 이를 구현하기 위해 dummy를 추가한 4×4 배열 안테나를 최종 설계하였다. 주기 구조 시뮬레이션과 높은 일치성을 보여 제작 및 측정을 진행하였다. 제작된 안테나의 반사

손실은 원하는 대역 모두에서 -10 dB 이하의 값을 가졌다. 축비, 이득, 패턴 모두 시뮬레이션과 거의 일치한 측정 결과를 얻을 수 있었다. 이를 통해 polarization-dependent 위상 조절 반사판이 효과적으로 축비를 개선하는 것을 검증하였다. 마지막으로 빔조향 특성을 확인한 결과 polarization-dependent 위상 조절 반사판을 적용하면서 손실없이 빔폭 내에서 1.5 dB 아래의 우수한 축비 값을 가지며 -30 도에서 30 도까지 빔조향이 가능함을 확인하였다.

결론적으로, 본 논문에서는 낮은 높이의 광대역 안테나 시스템을 구현할 때 극복해야 하는 두가지 주제에 대해 분석 및 해결하였다. 정확한 분석 및 적절한 해결 방안을 찾을 수 있었고 이를 통해 광대역 빔조향 네트워크와 낮은 높이의 광대역 배열 안테나에 적용하여 설계하였다. 최종적으로 측정 및 검증을 통해 전체 과정의 타당성을 검증하였다.

주요어: 광대역 빔조향 네트워크, 다층 적재된 실시간 지연회로, 소형화, 낮은 높이의 광대역 배열 안테나, 위상 조절 반사판, 축비 개선

학 번: 2013-20833

감사의 글

먼저 많이 부족한 저를 받아주시고 긴 시간 동안 많은 가르침을 주신 남상욱 교수님께 깊은 감사의 말씀 올립니다. 지식적인 측면 뿐만 아니라 문제를 바라보는 태도, 연구에 대한 열정 등 많은 부분에서 큰 가르침을 받을 수 있었습니다. 특히 주어진 문제를 바라보고 분석하고 해결하기 위해 끊임없이 생각하고 고민하고 발전해야 한다는 것을 배운 것이 저에게 가장 큰 도움이 된 것 같습니다. 가르침을 토대로 참된 연구자가 되어 열심히 살아가도록 하겠습니다. 또한, 바쁘신 와중에도 시간을 내어 제 논문을 지도해 주신 서광석 교수님, 박남규 교수님, 오정석 교수님, 그리고 박익모 교수님께도 큰 감사 드립니다.

다음으로 전파공학 연구실 선후배 분들께도 감사의 말씀을 드리고 싶습니다. 어떻게 보면 이렇게 많은 시간을 함께 보낼 수 있는 것도 하나의 큰 인연이라고 생각합니다. 그 안에서 연구적으로 인격적으로 많은 도움을 받을 것 같아 너무 고맙고 그 덕분에 이렇게 졸업할 수 있게 된 것 같습니다. 제가 도움이 되기 위해 노력한 부분이 부족한 것 같아 아쉽지만 인연이 끝이 아니기에 앞으로도 연락하며 서로 도움을 주고 받을 수 있는 사이가 되었으면 좋겠습니다.

마지막으로, 항상 내 편이 되어 묵묵하게 저를 믿고 응원해 주신 어머니, 할아버지, 할머니, 그리고 항상 지켜봐 주고 계실 아버지께도 큰 감사의 마음 전하고 싶습니다. 특히 어머니께 감사의 글을 통해 고맙고 항상 사랑한다고 전하면서 이 논문을 마칩니다.

2020년 2월 윤민영